Thesis

Production of medical radioisotopes ^{68}Ga and ^{45}Ti in deuteron-induced reactions in cyclotrons

(サイクロトロンを用いた重陽子入射反応による医療用放射性同位元素 ^{68}Ga と ^{45}Ti の生成)

09/24/2021

Hokkaido University

Zolbadral Tsoodol

Thesis

Production of medical radioisotopes ^{68}Ga and ^{45}Ti in deuteron-induced reactions in cyclotrons

(サイクロトロンを用いた重陽子入射反応による医療用放射性同位元素 ^{68}Ga と ^{45}Ti の生成)

09/24/2021

Hokkaido University

Zolbadral Tsoodol

Table of Contents

Presented Paper List and Conference Presentation List

Part of this study was presented in the following papers:

1. Zolbadral Tsoodol, Masayuki Aikawa, Ichinkhorloo Dagvadorj, Tegshjargal Khishigjargal, Namsrai Javkhlantugs, Yukiko Komori, Hiromitsu Haba, Production cross sections of ^{68}Ga and radioactive by-products in deuteron-induced reactions on natural zinc, Appl. Radiat. Isot. 159 (2020). doi:10.1016/j.apradiso.2020.109095.

2. Zolbadral Tsoodol, Masayuki Aikawa, Dagvadorj Ichinkhorloo, Tegshjargal Khishigjargal, Erdene Norov, Yukiko Komori, Hiromitsu Haba, Sándor Takács, Ferenc Ditrói, Zoltán Szűcs, Production cross sections of ^{45}Ti in the deuteron-induced reaction on ^{45}Sc up to 24 MeV, Appl. Radiat. Isot. (2020). doi:10.1016/j.apradiso.2020.109448.

Part of this study was presented in the following academic conferences:

1. Zolbadral Tsoodol, Masayuki Aikawa, Ichinkhorloo Dagvadorj, Tegshjargal Khishigjargal, Namsrai Javkhlantugs, Yukiko Komori, Hiromitsu Haba, as a poster presentation, Production cross sections of ^{68}Ga and radioactive by-products in deuteron-induced reactions on natural zinc, the 7th GI-CoRE Medical Science and Engineering Symposium on August 18-19, 2019, Hokkaido University, Sapporo,Hokkaido.

2. Ts.Zolbadral, M. Aikawa, D. Ichinkhorloo, Kh. Tegshjargal, N. Javkhlantugs, Y. Komori, H. Haba, Production cross sections of ^{68}Ga via deuteron-induced reactions on natural zinc, RIKEN Accelerator Progress Report 53, 190, 2020/10

3. Ts.Zolbadral, M. Aikawa, D. Ichinkhorloo, Kh. Tegshjargal, Y. Komori, H. Haba, S. Takács, F. Ditrói, Z. Szűcs, Production cross sections of ^{45}Ti via deuteron-induced reaction on ^{45}Sc, RIKEN Accelerator Progress Report 53, 191, 2020/10

4. Zolbadral Tsoodol, Masayuki Aikawa, Dagvadorj Ichinkhorloo, Khishigjargal Tegshjargal, Yukiko Komori, Hiromitsu Haba, Sándor Takács, Ferenc Ditrói, Zoltán Szűcs, Production cross sections of ^{45}Ti via deuteron-induced reaction on

^{45}Sc, Proceedings of the 2019 Symposium on Nuclear Data 75-78 2020/12 DOI:10.11484/jaea-conf-2020-001

5. Zolbadral Tsoodol, Masayuki Aikawa, Dagvadorj Ichinkhorloo, Khishigjargal Tegshjargal, Erdene Norov, Yukiko Komori, Hiromitsu Haba, Sándor Takács, Ferenc Ditrói, Zoltán Szűcs, Production cross sections of ^{45}Ti via deuteron-induced reaction on ^{45}Sc, AESJ 2020 Fall Meeting as an oral presentation on September 16-18, 2020 Online Meeting.

CHAPTER 1: Introduction

The discoveries of X-ray, radioactivity, nuclear reaction, neutron and charged particles in the early twentieth century are all important parts of the basis of medical physics.

We can highlight the following achievements in relation with nuclear medicine: In 1935, Enrico Fermi discovered neutron-induced radioactivity. It marked the beginning of nuclear medicine as a neutron-induced reaction (The Editors of Encyclopedia Britannica, 2018). Nuclear fission was discovered by Otto Hahn and Fritz Strassmann in 1938, which led to the construction of nuclear reactors (Gill, Livens and Peakman, 2014). Ernest Lawrence and John Lawrence invented the first cyclotron in 1939, and several other researchers established the use of cyclotrons in the medical field (Carlson, 1995).

The first use of radioisotopes as tracers in the study of chemical processes by George de Hevesy was the most important event in the history of nuclear medicine (Hevesy, 1943). David Kuhl introduced the emission reconstruction tomography in 1956 (Jaszczak, 2006; Portnow, Vaillancourt and Okun, 2013). It becomes the basis of diagnostic techniques for computed tomography (CT), single-photon emission computed tomography (SPECT), positron emission tomography (PET), and multimodality (PET/CT, SPECT/CT/MRI).

Among these diagnostic imaging techniques, PET is a powerful one based on an annihilation reaction induced between a positron and an electron. A positron emitted from a radiopharmaceutical injected into a patient reacts with an electron in tissue (Omami, Tamimi and Branstetter, 2014). The positron emitter contained in the radiopharmaceutical is one of the important parts of the PET diagnostic technique. For instance, F-18 fluorodeoxyglucose (FDG) is used for PET imaging and considered as a standard PET isotope. Recently, we utilizes a variety of positron emitters for PET (Qaim *et al.*, 2016; Qaim, 2017; Boros and Packard, 2019). Such PET isotopes are mainly produced using accelerators and cyclotrons (Qaim, 2017) and a few positron emitters can be produced from generators. It is also possible to use neutron-induced reactions.

Despite that most PET isotope production routes are well-established, ongoing research is needed for more efficient production of PET radionuclides and development of new radionuclides for medical applications. To maximize the yield of the desired

product and minimize the impurity, it is necessary to choose an appropriate projectile energy and to use an isotopically pure target and chemical separation of the product. For such optimization, nuclear decay and reaction data are crucial (Qaim, 2017).

The non-conventional positron emitters ^{68}Ga and ^{45}Ti are expected to become more popular in clinical PET scanners. For the cyclotron production of these PET isotopes, the promising route is the (p,n) reaction on isotopically enriched targets. Alternative production route is the (d,2n) reaction, which can produce the same residual as the (p,n) reaction. In literature, a few experimental cross section data on deuteron induced reactions for production of ^{68}Ga and ^{45}Ti were reported. However, there are significant discrepancies among the experimental data and less reliable data available. Therefore, we aim to investigate the deuteron-induced reactions for the production of the emerging PET isotopes ^{68}Ga and ^{45}Ti. Two experiments were carried out to measure reliable production cross sections of ^{68}Ga and ^{45}Ti in deuteron induced reactions on natural zinc and scandium. Based on the experiments, the production routes of the two radioisotopes can be discussed.

A brief history of nuclear physics milestones, which impact on developments of nuclear medicine, was reviewed in the chapter one. The chapter two describe the definition of some basic terms of nuclear reaction and decay and radionuclide production. The experimental details used are given in the chapter three. The procedures, such as target preparation, irradiation condition, data acquisition and analysis, are shown. The chapter also provides the monitor reaction for cross-checking of incident beam parameters and uncertainty estimations on the measured cross section. The chapter four shows the first experiment using a natural zinc target irradiated by a deuteron beam of 24 MeV for the production of the medical radionuclide ^{68}Ga. Co-produced radioisotopes are also investigated to evaluate amounts of impurities for practical use of ^{68}Ga. All the results were discussed in comparison with the previous experimental data and the theoretical predictions of TENDL-2019. Physical yields of the radionuclides were deduced from the measured cross sections. Based on a comparison between proton- and deuteron-induced reactions on natural zinc, we discussed the production reaction of ^{68}Ga. In the chapter five, our second experiment are given. Production cross sections of the medically interesting radionuclide ^{45}Ti were investigated in the deuteron-induced reaction on ^{45}Sc up to 24 MeV. The activation cross sections of the radioactive impurities such as ^{44}Ti and ^{44g,44m,46}Sc isotopes were also determined. All our measured results were compared with

the previous experimental data and the theoretical predictions of TENDL-2019. The physical yield of ^{45}Ti was deduced from the measured cross sections. The production of the radioactive-contamination-free ^{45}Ti via the ^{45}Sc(d,2n)^{45}Ti reaction was discussed. The chapter six presents the results and conclusions.

Abbreviation Table

The abbreviations used in the body text and figures are as follows:

AVF	Azimuthally Varying Field
CT	Computed Tomography
FWHM	Full Width at Half Maximum
HPGe	High Purity Germanium
IAEA	International Atomic Energy Agency
MRI	Magnetic Resonance Imaging
SPECT	Single-Photon Emission Computed Tomography
PET	Positron Emission Tomography
PHY	Physical Yield
RI	Radioactive Isotope
SRIM	Stopping and Range of Ions in Matter
TOF	Time-Of-Flight
TENDL	TALYS-based Evaluated Nuclear Data Library

CHAPTER 2: Basic Concepts

2.1 Nuclear reaction

A nuclear reaction is a process that a nuclear particle (nucleon or nucleus) collides with another one. In the nuclear reaction, the incident particles can be scattered to another direction or changed to different particles. It can be noted as:

$$\mathrm{X}(a,b)\mathrm{Y}$$

where X is a stable nuclide at rest (target), a is an accelerated particle (projectile), Y is a product nuclide (residual), b is an emitted particle or photon.

In a nuclear reaction, several conservation laws are preserved, such as baryonic number, charge, energy and linear momentum, total angular momentum, parity, and isospin. Several physical quantities such as the Q-value, the threshold energy, and the cross section depend on each nuclear reaction.

2.1.1 Q-value and threshold energy

A certain amount of energy, Q [MeV], can be released or absorbed when a particular nuclear reaction takes place. The Q-value is defined as:

$$Q = [(m_a + m_X) - (m_Y + m_b)] \cdot c^2 \tag{2.1}$$

where m_a is the mass of the projectile, m_X is the mass of the target, m_Y is the mass of the residual and m_b is the mass of the emitted particle.

There are three cases:

- $Q = 0$ means elastic scattering,
- $Q > 0$ means that the final system has lighter total mass, which is called exothermic, and this reaction may occur at any incident energy.
- $Q < 0$ means that the final system has heavier total mass, which is called endothermic.

For an endothermic reaction ($Q < 0$), a certain amount of energy to be absorbed is required. This energy is called the threshold energy, which is the minimum kinetic energy of the projectile to induce the nuclear reaction. From the conservation laws of energy and momentum, the threshold energy E_{thr} can be derived as:

$$E_{thr} = |Q| \cdot \left(1 + \frac{m_a}{m_X}\right) \tag{2.2}$$

As an example of the ^{68}Zn(d,2n)^{68}Ga reaction, the Q and E_{thr} values are:

$$\begin{aligned} Q &= [m_a(^2_1H) + m_X(^{68}_{30}Zn) - m_Y(^{68}_{31}Ga) - m_b(2n)] \cdot c^2 \\ &= [2.014\text{u} + 67.925\text{u} - 67.928\text{u} - 2 \cdot 1.009\text{u}] \cdot 931.502\ \text{MeV/u} \\ &= -5.928\ \text{MeV} \end{aligned}$$

$$\begin{aligned} E_{thr} &= |Q| \cdot \left(1 + \frac{m_a(^2_1H)}{m_X(^{68}_{30}Zn)}\right) \\ &= 5.928\ \text{MeV} \cdot \left(1 + \frac{2.014\text{u}}{67.925\text{u}}\right) \\ &= 6.103\ \text{MeV} \end{aligned}$$

Hence, the ^{68}Zn(d,2n)^{68}Ga reaction is the endothermic reaction and occurs above the projectile energy of 6.103 MeV. Other residuals, ^{69}Ga and ^{67}Ga, can be formed as impurities above their own threshold energies. A suitable energy window of the projectile beam to avoid such impurities can be defined to optimize radioisotope production. The reaction threshold energy is a key parameter to describe the suitable energy window.

2.1.2 Reaction cross section

A reaction cross section is an important physical quantity to describe a nuclear reaction. The cross section is probability to induce the nuclear reaction between one incident particle and one target nucleus. It can be considered as an effective area of interaction between the particle and target nucleus.

To introduce the reaction cross section, we consider a flux of incident charged particles per second I_p [#/s] impinging a foil of a matter of area L^2. The foil contains N_0 mono-isotopic stable nuclei with a sphere shape of radius r, as shown in Fig. 2.1.

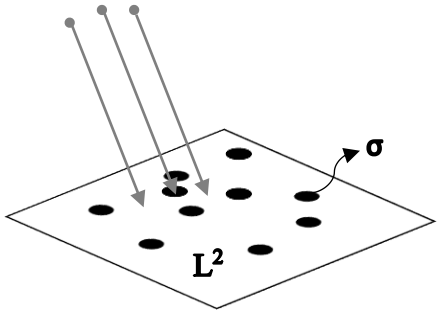

Fig. 2.1. Irradiation of projectiles on a foil of a matter containing N_0 stable nuclei of cross-sectional area $\sigma = \pi \cdot r^2$.

A probability P_{hit} that one incident charged particle collides with the target nuclei is equal to the fraction of the surface area covered by the target nuclei to the foil area L^2 (Basdevant, Rich and Spiro, 2005).

$$P_{hit} = \frac{N_0 \cdot \sigma}{L^2} \tag{2.3}$$

Because of a geometrical area of the target nucleus, the cross section has dimensions of area per nucleus. It can be used to define the probability for any types of reactions.

The cross section of the nuclear reaction differs from the geometrical cross section. The reaction cross section σ_r corresponds to the effective surface area of the target nucleus. A common unit of the cross section of the nuclear reaction is barn, 1 b = 10^{-24}

cm^2. The cross section of a nuclear reaction depends upon the type and energy of the incident particle and the target nuclei. The reaction cross section can be determined based on experiments. A concept with an energy dependent cross section is more useful in practical applications.

The cross sections as a function of the kinetic energy of the incident particle are called an excitation function, $\sigma(E)$. The excitation function typically increases from the threshold energy of the nuclear reaction until a maximum value and then decreases with the increasing energy. The excitation function enables to investigate a particular production route.

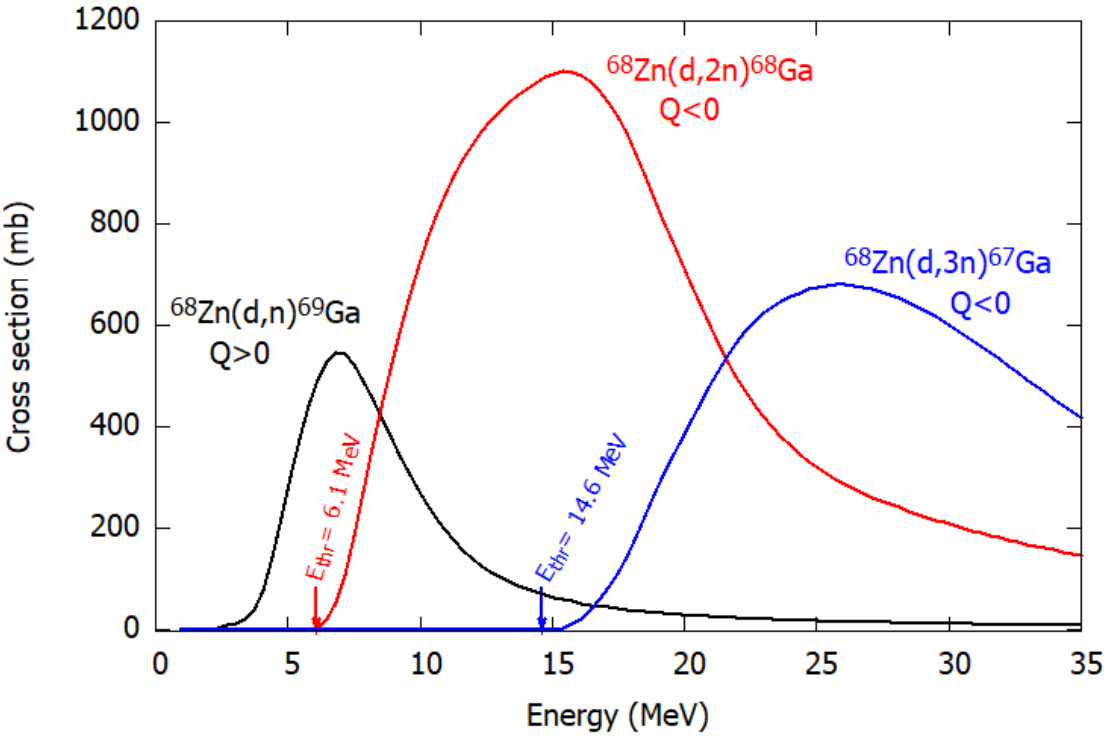

Fig. 2.2. The excitation functions, the threshold energies and Q-values of the ^{68}Zn(d,xn)^{67,68,69}Ga reactions.

Figure 2.2 shows an example of the excitation functions of ^{67,68,69}Ga formation via deuteron-induced nuclear reactions on isotopically enriched ^{68}Zn. The cross section data are taken from the TENDL-2019 library (Koning *et al.*, 2019). In this example, the stable

^{69}Ga is formed by the ^{68}Zn(d,n) reaction. Its threshold energy is E_{thr} = 0.0 MeV and this is an exothermic nuclear reaction (Q>0). As the projectile energy increases, various reaction channels are opened. Thus, the radioactive ^{68}Ga and ^{67}Ga isotopes are formed by the (d,2n) and (d,3n) reactions on ^{68}Zn. Their threshold energies are E_{thr}= 6.1 MeV and E_{thr}= 14.6 MeV, respectively. These are endothermic nuclear reactions.

2.1.3 Radioactive decay and types of beta decay

The most important factor that affects nuclear stability is the neutron/proton ratio. If a nucleus with the mass number less than 40 contains the equal numbers of protons and neutrons, the nucleus is more stable. If this ratio is too high or too low, the nucleus is unstable and leads a radioactive decay. The radioactive decay is spontaneous disintegration process of the unstable nucleus. Charged particles and electromagnetic radiation (gamma rays) are emitted with the radioactive decay. The rate of the radioactive decay is termed "activity" and expressed in the unit of Becquerel [Bq], which is the number of decays per second. The activity $A(t)$ can be expressed as

$$A(t) = \frac{dN_u(t)}{dt} = -\lambda \cdot N_u(t) \tag{2.4}$$

where $N_u(t)$ and λ [s^{-1}] are the number and a decay constant of the radioactive nucleus.

The decay constant λ is related to the half-life of the radioactive nucleus, $T_{1/2}$ [s],

$$T_{1/2} = \frac{\ln 2}{\lambda} \tag{2.5}$$

There are several types of radioactive decay as follows:

- α-decay is the ejection of an alpha-particle and governed by the strong interaction
- β-decay is the ejection of an electron or positron and governed by the weak interaction
- γ-decay is the ejection of electromagnetic radiation from the internal transition between energy states in the nucleus.

In this thesis, the investigated medical isotopes, ^{68}Ga and ^{45}Ti, are positron emitters. Thus, we consider a little detailed description of the beta decays.

β^- decay:

$$^{A}_{Z}X = {}_{Z+1}^{A}X + e^- + \overline{\nu_e}$$

In the β^- decay process, one neutron turns into one proton in the nucleus. The decay neutron emits an electron and an antineutrino.

$$n = p + e^- + \bar{\nu_e}$$

The Q value associated with this process is

$$Q_{\beta^-} = \left[m_n - m_p - m_e\right] \cdot c^2 = 939.566 - 938.272 - 0.511 = 0.783 \text{ MeV}$$

This process is possible spontaneously in case of $Q_{\beta^-} > 0$.

β^+ decay:

In the β^+ decay, one proton turns into one neutron. The decay proton emits a positron and a neutrino.

$$p = n + e^+ + \nu_e$$

The Q value of one proton decay is $Q_{\beta^+} = -1.805$ MeV. This negative Q value implies that the energy supply is required from outside. On the contrary, in proton-rich unstable nuclei, one proton can turn into a neutron spontaneously.

$${}^{A}_{Z}X = {}_{Z-1}{}^{A}X + e^+ + \nu_e$$

Some examples of the β^+ decay is:

a. ${}^{68}_{31}Ga = {}^{68}_{30}Zn + e^+ + \nu_e$ - The average energy of the emitted positron is $E_{\beta^+}{}^{ave}$ = 829.5 keV and its total intensity is $I_{\beta^+}^{total} = 88.9\%$.

b. ${}^{45}_{22}Ti = {}^{45}_{21}Sc + e^+ + \nu_e$ - It emits a positron with an average energy of 439 keV and its total intensity is $I_{\beta^+}^{total} = 84.8\%$.

Electron capture (EC):

In this decay, an orbital electron is captured by a proton and causes the emission of the electron neutrino.

$$p + e^- = n + \nu_e$$

The Q value is $Q_{EC} = -0.783$ MeV and it is not a spontaneous process. The β^- decay occurs in neutron-rich nuclei, while the β^+decay and EC undergo in proton-rich nuclei.

$$ {}^{A}_{Z}X + e^- = {}_{Z-1}{}^{A}X + \nu_e $$

2.2 Production of radioisotopes in cyclotrons

2.2.1 Production and cumulative cross sections

One of the main applications of radioactive isotopes is nuclear medicine. In this field, a terminology of "*production cross section*" is used. It is the sum of cross sections of all reaction channels contributing to production of the radioisotope of interest.

The radioisotope of interest can be produced by different nuclear reactions if a target contains several isotopes. For example, natural zinc targets in deuteron-induced reactions can contribute to the production of ^{67}Ga as shown in Fig. 2.3. All the cross sections on each zinc isotope are normalized using natural zinc isotopic composition and those on natural zinc were derived. There exist two peaks in the energy region below 25 MeV. The first peak is around 8 MeV. The main contribution to the peak comes from the exothermic (d,n) reaction on ^{66}Zn (abundance: 27.73%). The (d,2n) reaction on ^{67}Zn can contribute into the peak above 4.1 MeV but its contribution is small due to the relatively low abundance of ^{67}Zn (4.04%). The second peak comes from the (d,3n) reaction on ^{68}Zn (18.45%). Its threshold energy is E_{thr} = 15.7 MeV.

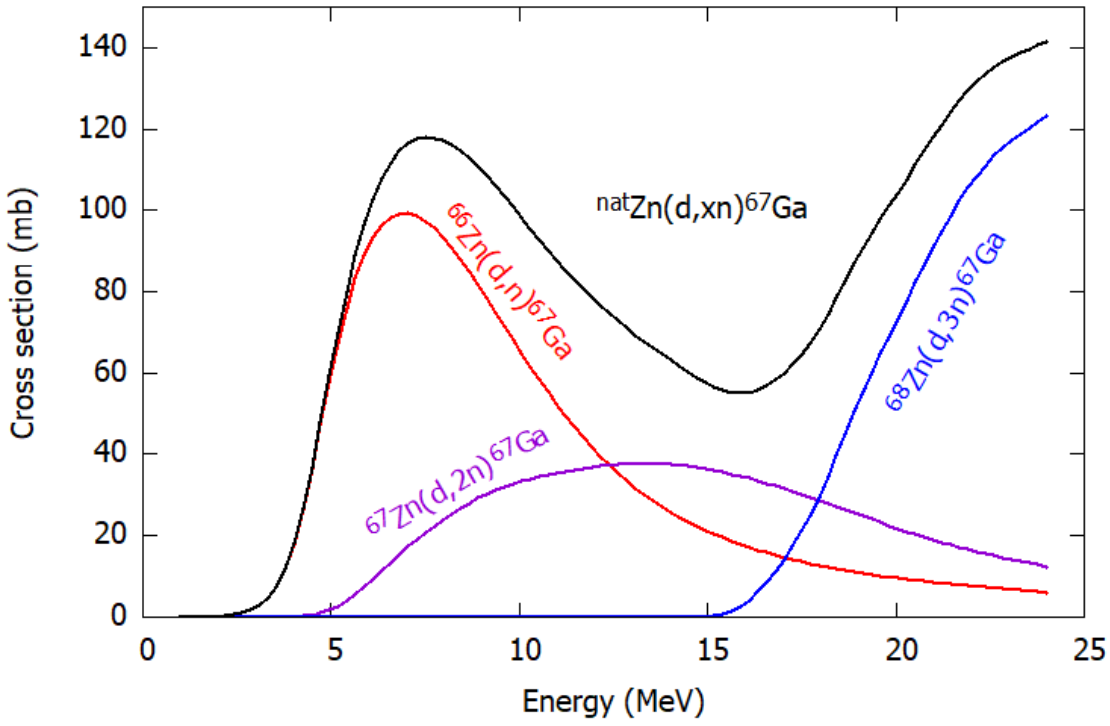

Fig. 2.3. Production cross section of ^{67}Ga in deuteron induced reactions on natural zinc derived from the data retrieved from the TENDL-2019 library (Koning *et al.*, 2019).

As shown in the example above, the production cross sections of ^{67}Ga through the deuteron-induced reaction on a natural zinc target can be estimated as

$$\sigma_{^{nat}Zn(d,x)^{67}Ga} = 0.2773 \cdot \sigma_{^{66}Zn(d,n)^{67}Ga} + 0.0404 \cdot \sigma_{^{67}Zn(d,2n)^{67}Ga} + 0.1845 \cdot \sigma_{^{68}Zn(d,3n)^{67}Ga}$$

The medical isotope can be produced via the direct production route and also indirect production routes. The indirect routes are the decay of the co-produced parent and the meta-stable state of the isotope of interest.

A terminology of "*cumulative production cross section"* describes the sum of the cross sections in these direct and indirect production routes. An example is that of ^{65}Zn in deuteron-induced reactions on natural zinc as shown in Fig. 2.4. The longer-lived ^{65}Zn ($T_{1/2}$=243.93 d) is directly formed in the deuteron irradiation on ^{64}Zn, ^{66}Zn and ^{67}Zn in natural zinc below 24 MeV. The shorter-lived ^{65}Ga ($T_{1/2}$=15.2 min) is simultaneously produced via reactions on ^{64}Zn and ^{66}Zn. Then ^{65}Ga decays into ^{65}Zn by EC and β^+ processes. The measured cross section is regarded as the cumulative one. The direct and indirect cross sections can be separated if the production cross section of the co-produced precursor, ^{65}Ga, is determined. The indirect contribution from the decay of ^{65}Ga is large in Fig. 2.4.

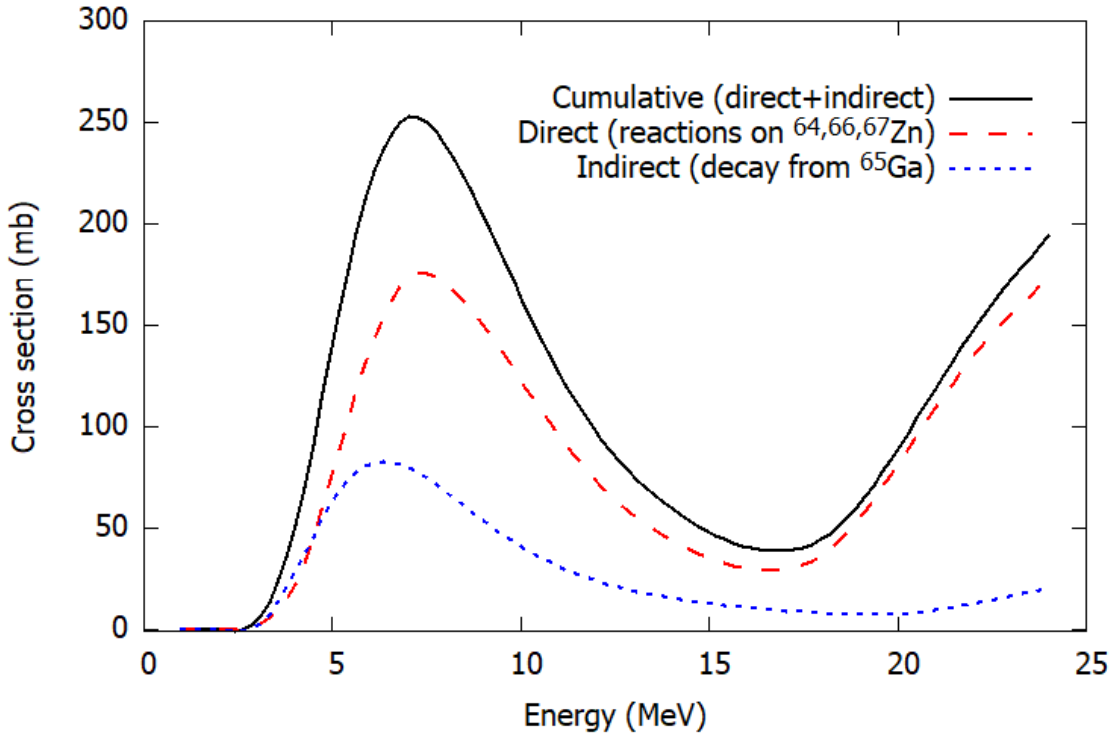

Fig. 2.4. Cumulative, direct, and indirect production cross sections of ^{65}Zn in deuteron induced reactions on natural zinc derived from the data retrieved from the TENDL-2019 library (Koning *et al.*, 2019).

2.2.2 Production rate

A production rate is the number of produced nuclei per second Y (#/s) in nuclear reactions. It depends on the energy. The production rate of a stable nucleus for a particular reaction is proportional to the number of target nuclei per unit area of the foil n_T [#/cm^2] (discussed in Section 3.1.1), the flux of the incident charged particle I_p [#/s] (discussed in Section 3.2.1), and the reaction cross section σ_r:

$$Y = n_T \cdot I_p \cdot \sigma_r \tag{2.6}$$

If the produced nucleus is unstable, it decays during the irradiation. The production rate of the unstable nuclei can be described as:

$$\frac{dN(t)}{dt} = Y - \lambda \cdot N(t) \tag{2.7}$$

The number of radioactive nuclei $N(t_{irr})$ produced at the time t_{irr} is as follows:

$$N(t_{irr}) = Y \cdot \frac{\left(1 - e^{-\lambda t_{irr}}\right)}{\lambda} \tag{2.8}$$

The number *N*(t) is shown in Fig. 2.5. During the irradiation, the *N* increases. After the irradiation, the *N* decreases exponentially. Irradiation longer than two to three half-lives is ineffective because 80% of the maximum number of the nuclei has already been produced.

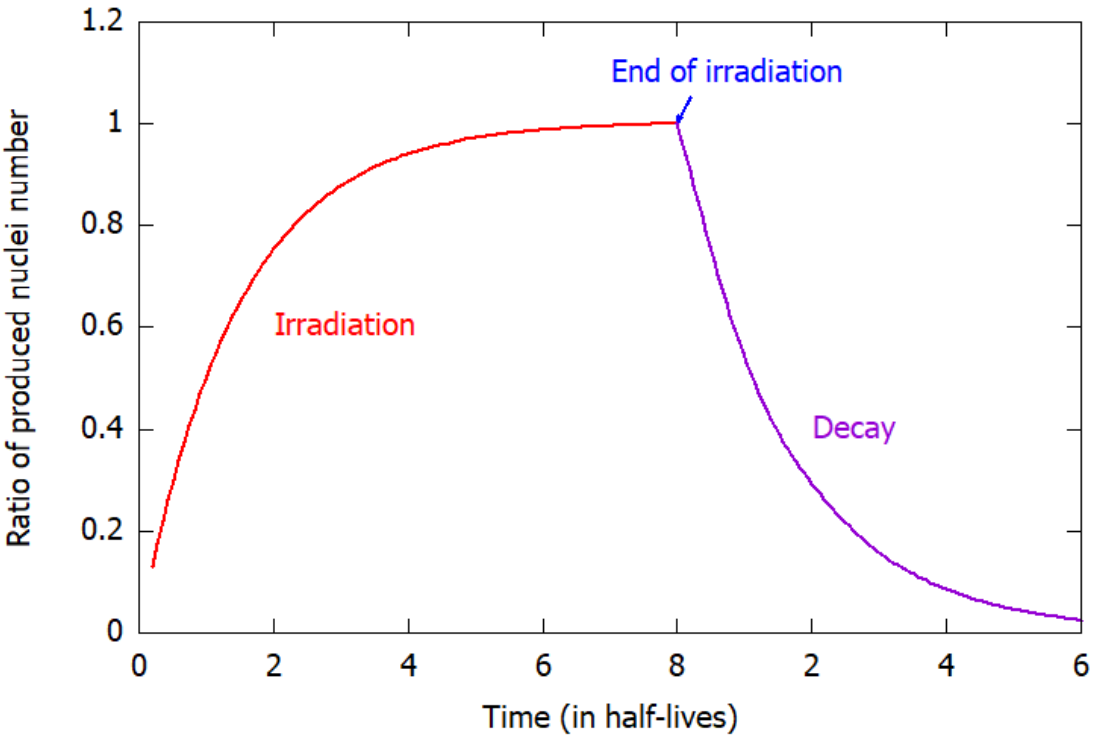

Fig. 2.5. The number of the produced nuclei relative to the peak as a function of time.

2.2.3 Physical yield for a thick target.

Physical yield (PHY) is a ratio of the number of nuclei formed in the nuclear reaction to the number of particles induced on the target (Qaim *et al.*, 2001). We consider irradiation on a thick target with a thickness of dx as shown in Fig. 2.6. The energy of incident charged particles decreases in the thick target. Because the energy loss of the projectile is not negligibly small, the reaction cross section $\sigma(E)$ in the thick target varies depending on the projectile energy.

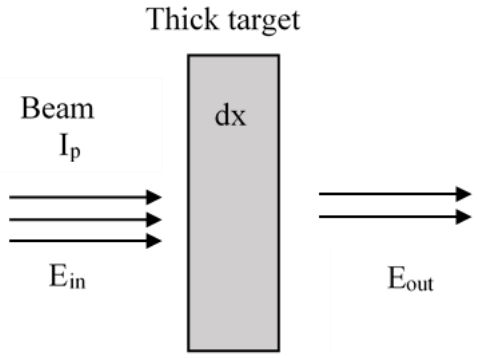

Fig. 2.6. Energy degradation of the incident beam with E_{in} after passed through a target with a thickness of dx

According to the literature (Otuka and Takács, 2015), the physical yield for thick target is defined as:

$$PHY = H \cdot \frac{N_A}{A_t \cdot Z_p \cdot e} \cdot \int_{E_{out}}^{E_{in}} \frac{\sigma(E)}{dE/d\rho x} dE \cdot \lambda \tag{2.9}$$

where E_{in} and E_{out} are the incident and outgoing energies of the projectile and $dE/d\rho x$ is mass stopping power (explained in section 2.2.4), H is the abundance or purity of the target nuclei, N_A is Avogadro's number [#/mol], A_T is the molar mass of the target element [g/mol] Z_p is the atomic number of the projectile and e is the elementary charge. The physical yield is expressed as activity per electric charge, in the unit of $\mathrm{Bq/C}$. The electric charge is convertible to the product of current and time and its unit is $\mathrm{Bq/As}$. The physical yield in the unit of $\mathrm{MBq/\mu Ah}$ is widely used for practical use.

2.2.4 Stopping power

Incident charged particles interact with atoms in a target through electronic and nuclear processes. Due to these processes, the projectiles lose their energy. The force is stopping power of the material. The rate of loss of the energy depends on the properties of both the incident and target particles.

Liner stopping power $S(E)$ describes the average energy loss of projectiles per unit length in the target in [MeV/cm]:

$$S(E) = -dE/dx \tag{2.10}$$

The liner stopping power $S(E)$ depends on the material density. In fact, the stopping power of solid and gas states is very distinct. Thus, the mass stopping power $S_m(E)$ can be described by the liner stopping power divided by the material density:

$$S_m(E) = -dE/d(\rho x) \tag{2.11}$$

where ρ is the material density. The unit of the mass stopping power is MeV/mg/cm^2.

The energy loss of the projectile occurs due to interaction with the electrons and nuclei in the target. The process with the former is the electronic stopping power, $S_e(E)$. The process with the latter is the nuclear stopping power, $S_n(E)$.

The total stopping power is the sum of the electron $S_e(E)$ and nuclear stopping powers $S_n(E)$:

$$S_{tot}(E) = S_e(E) + S_n(E) \tag{2.12}$$

In general, the nuclear stopping powers $S_n(E)$ is small because the nuclear force acts in a short range. It implies that the electromagnetic interaction between the projectile and target is dominant.

For example, stopping power in the case of a deuteron beam on zinc is calculated using the SRIM software (Ziegler, Ziegler and Biersack, 2010) and shown in Fig. 2.7. It is seen that the electronic stopping power is more dominant than the nuclear stopping power.

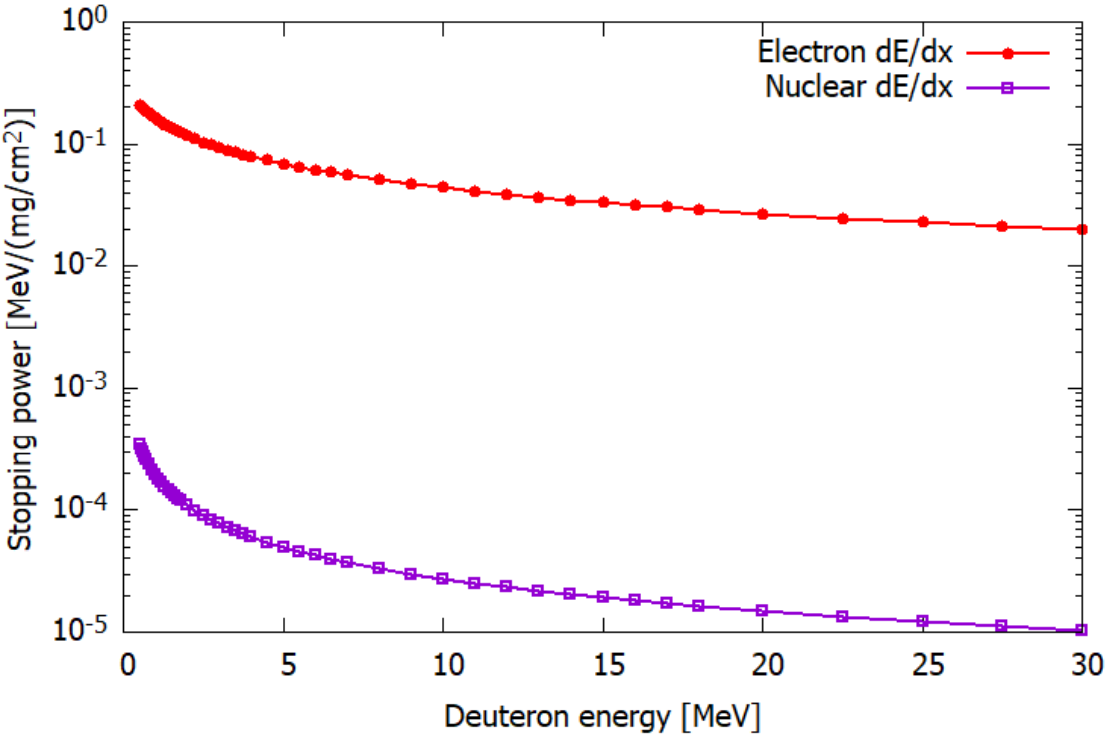

Fig. 2.7. Stopping powers in the case of a deuteron beam on zinc calculated using the SRIM software.

CHAPTER 3: Experimental Details

3.1 Target preparation

Various types of targets in solid, liquid, and gaseous states can be used for radioisotope production. The thicknesses of these targets vary from a few to several hundred mg/cm^2 (Stolarz, 2014). The targets should have the following features: high chemical purity, uniform thickness, good mechanical strength, stability under a beam, and easy processing after irradiation.

In our experiments, solid targets (pure metal and thin foils) are used to measure the production cross sections of medical isotopes. Because the solid targets are denser than gas and liquid ones, the path length of a beam becomes shorter, and the target thicknesses can be thinner. The thinner solid foils enable to measure an excitation function with better resolution and structure.

In general, the foils in a target play three different roles in the experiments. The first one is a main target foil to produce the medical isotope of interest. The second one is a catcher foil of recoiled products at the downstream of the main target foil. The catcher foil should satisfy requirements for few radioactive products by the nuclear reaction in the investigated energy range. Moreover, to minimize γ-ray attenuation during the measurement, the catcher foil of a lower atomic number should be selected (Alharbi *et al.*, 2011). The last one is a monitor foil (discussed in Section 3.2.2) used to assess beam parameters.

The target configuration of the three type foils is arranged based on the calculation of energy degradation (discussed in section 3.1.2) as shown in Fig. 3.1. Then the foils were stacked into a target holder served as a Faraday cup. The stacked target is irradiated with a beam.

a)

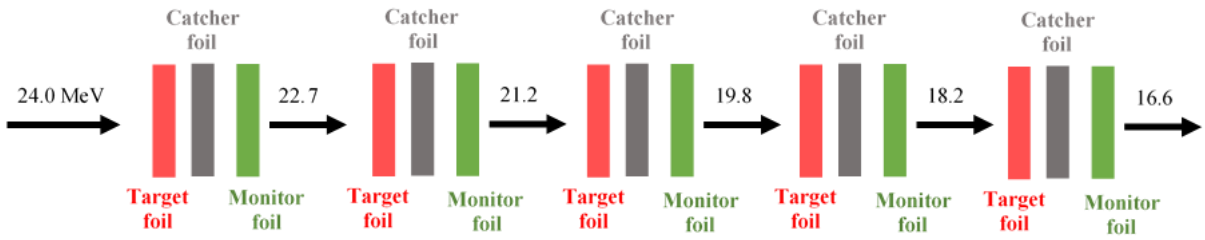

b)

Fig. 3.1. (a) Target foils and a target holder, and (b) a schematic of the stack configuration.

3.1.1 Target thickness

Target thicknesses of the foils should be determined. The number of nuclei per unit area n_T [#/cm^2] can be derived from the average thickness n_{avg} [g/cm^2] (mass thickness), derived from weight and size measurements. In the experiments, large metal foils were purchased from a commercial company and their thickness and purity were provided by them. The exact foil thicknesses may be different from the provided values. Thus, the

average thicknesses of the foils are derived by measuring the weights and sizes of larger foils. The derived average thickness n_{avg} [mg/cm^2] can be evaluated as

$$n_{avg} = \frac{\langle m \rangle}{\langle S \rangle} \tag{3.1}$$

where $\langle m \rangle$ and $\langle S \rangle$ are the average values of several measurements of the weights and sizes of larger foils, respectively. The uncertainty of foil thicknesses is estimated from these measurements.

The number of target nuclei N_0 in the foil is

$$N_0 = H \cdot \frac{m}{A_T} \cdot N_A \tag{3.2}$$

where m is the weight of the foil [g].

From Equations 3.1 and 3.2 n_T [#/cm^2] can be estimated as

$$n_T = \frac{H \cdot N_A}{A_T} \cdot n_{avg} \tag{3.3}$$

3.1.2 Energy degradation calculation

Energy degradation of the projectile in the target can be estimated using the stopping power calculated by the SRIM software (Ziegler, Ziegler and Biersack, 2010). We consider a beam with the incident energy of E_{in} impinging on a thin metal foil with a thick x and a density ρ. The relation between the average thickness n_{avg} [mg/cm^2] and the mass stopping power $S_m(E)$ (discussed in Section 2.2.4) can be expressed as follows:

$$n_{avg} = x \cdot \rho = \int_{E_{out}}^{E_{in}} \left(\frac{1}{S_m(E)} \right) dE \tag{3.4}$$

The stopping power $S_m(E)$ can be approximated as a linear function for a thin foil (small energy loss) as:

$$S_m(E) = b + a \cdot E \tag{3.5}$$

where a is slop and b is intercept coefficients.

Equation (3.4) can be written using Equation (3.5) as:

$$x \cdot \rho \approx \int_{E_{out}}^{E_{in}} \frac{1}{(aE + b)} dE \tag{3.6}$$

From Equation (3.6), the degraded energy after passed through a thin foil, E_{out}, can be calculated as:

$$E_{out} = E_{in} e^{a\rho x} + \frac{b}{a}(e^{a\rho x} - 1) \tag{3.7}$$

An example of energy degradation is shown in Fig. 3.2 in the case of a deuteron beam of 24 MeV impinging on a staked target with a configuration of Zn-Ti-Ti sets. The thicknesses of the Zn and Ti foils were 17.64 and 9.31 mg/cm^2, respectively. To fully stop the deuteron beam in the target, a total of 46 foils are required.

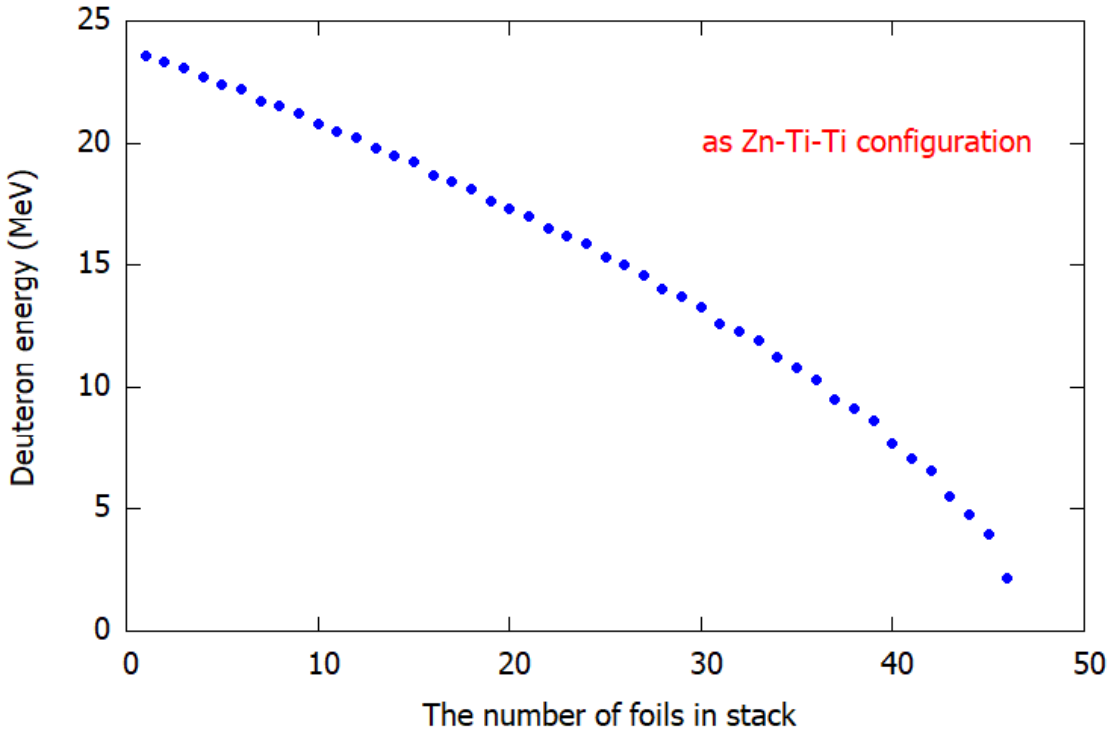

Fig. 3.2. Energy degradation of a 24-MeV deuteron beam in the stacked target.

3.2 Irradiation and measurement processes

The stacked target was irradiated with a beam. In the experiments, the energy of the incident beam was measured by the time-of-flight method (TOF) (Watanabe *et al.*, 2014). The beam intensity was measured using a Faraday cup. The beam parameters were cross-checked with the $^{nat}Ti(d,x)^{48}V$ monitor reaction (discussed in Section 3.2.2). During the irradiation, the beam current was kept constant. The irradiation period is determined depending on the experimental condition and inappropriate to be 2 or 3 times longer than the half-life as shown in Fig. 2.5. For a larger number of products and better statistics of γ-ray measurements, however, the foil should be irradiated longer as long as possible.

After the irradiation, the activated stack was dismantled without any chemical separation. Then the decay γ rays emitted from the dismantled foils were measured and analyzed by the Gamma Studio software (SEIKO EG&G). Each foil was measured several times using a high-resolution HPGe detector (given in Appendix A). The detector efficiencies for various source-detector distances were determined using a mixed γ-ray standard source (given in Appendix A). The source has known activities to cover the energy range between 60 and 1836 keV. The cooling times were essential to avoid interference of γ-lines from byproducts and to evaluate cumulative formation of the longer-lived radionuclide. In addition to the strong characteristic γ-lines of each radioisotope, weak γ-lines were also considered to cross-check. In the cases of longer-lived radionuclides, activity measurements were carried out after sufficient cooling times for the complete decay of shorter-lived isotopes.

3.2.1 Measurement of beam intensity

The deuteron beam current is directly measured using a Faraday cup and cross-checked with the $^{nat}Ti(d,x)^{48}V$ monitor reaction. The Faraday cup can measure electric current. The positive ions in the beam reach at the target in the Faraday cup and gain electrons. The electrons were provided through an amperemeter. The total charge can be measured using the amperemeter. A schematic diagram and real photos of the Faraday cup like target holder is shown in Fig. 3.3.

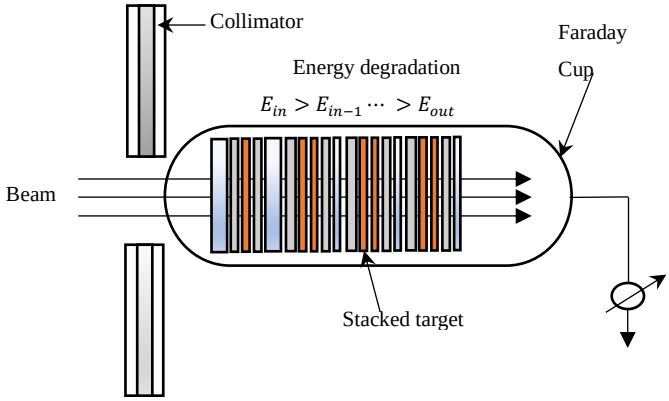

a)

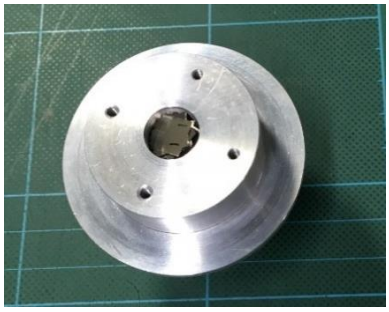

b)

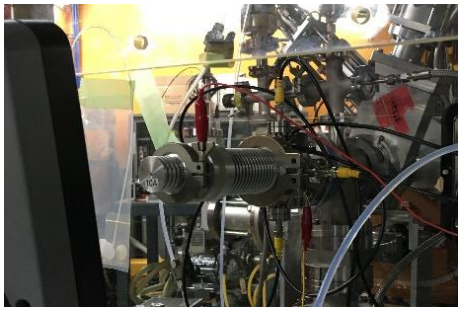

c)

Fig. 3.3. Faraday cup like target holder: (a) schematic diagram, (b) a real photo and (c) installed on beam line.

The average beam current I $[A]$ is defined as:

$$I = \frac{q_{tot}}{t_{irr}} \tag{3.8}$$

where q_{tot} is the total charge measured by the Faraday cup and t_{irr} is the irradiation time.

The total charge is proportional to the total number of projectiles n_p. It can be expressed as follows:

$$q_{tot} = n_p \cdot Z_p \cdot e \tag{3.9}$$

.

From Equations 3.8 and 3.9, the average number of projectiles per second I_p [#/s] is

$$I_p = \frac{n_p}{t_{irr}} = \frac{I}{Z_p \cdot e} \tag{3.10}$$

3.2.2 Monitor reaction

The monitoring reaction can be used to double-check the measured beam intensity. The procedures are as follows:

- The cross sections of the monitor reaction are derived using the intensity directly measured by the Faraday cup. The intensity is common for the monitor and the target foils because the foils are arranged in one stack and irradiated simultaneously. The loss of projectiles due to reactions is very small and neglected.
- The derived excitation function of the monitor reaction is compared with the recommended values of the International Atomic Energy Agency (IAEA) (Takács et al., 2007; Hermanne *et al.*, 2018).
- If there are any discrepancy between the derived and the recommended excitation functions, the beam intensity is corrected within the uncertainty. This corrected beam intensity is adopted in data assessment of the cross sections.

There are several monitor reactions recommended by the IAEA (Takács et al., 2007; Hermanne *et al.*, 2018) with regard to the energy region and projectile type. In our experiments, the $^{nat}Ti(d,x)^{48}V$ reaction is used and shown in Fig. 3.4.

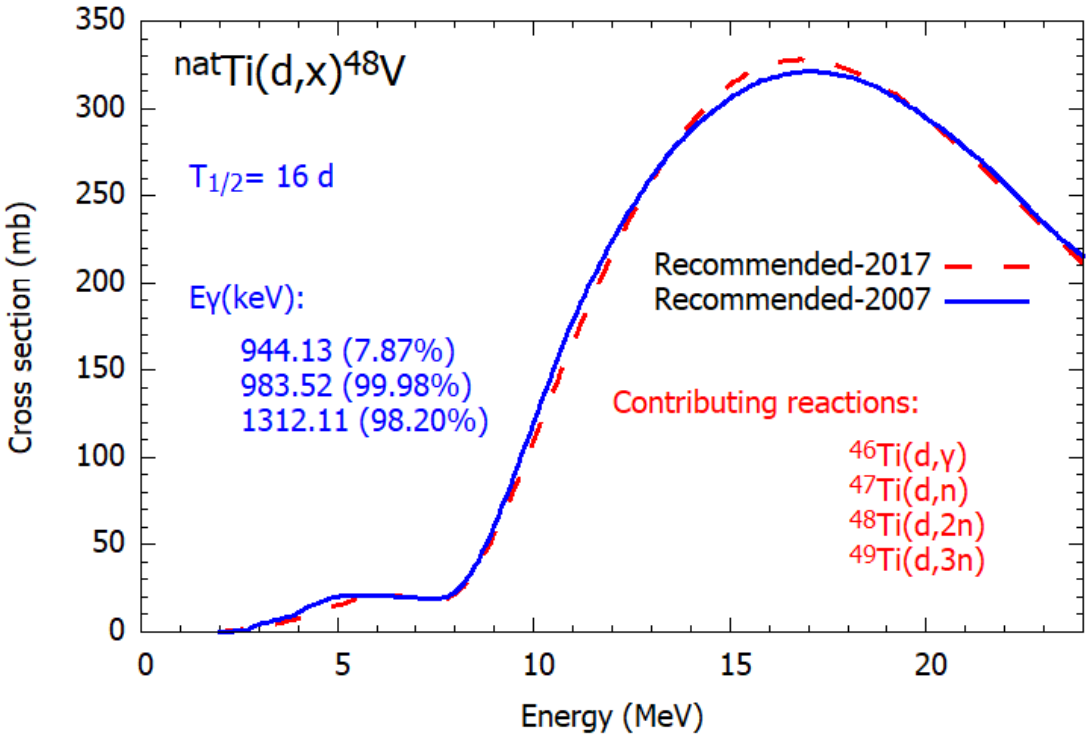

Fig. 3.4. The excitation functions of the ^{nat}Ti(d,x)^{48}V monitor reaction (Takács *et al.*, 2007; Hermanne *et al.*, 2018).

3.3 Data analysis

3.3.1 Derivation of the production cross section from measurement.

One way to detect the radioactive isotope produced by irradiation is to measure the radiations from its decay.

It is assumed that the irradiation lasted for the time t_{irr}. After the irradiation, we wait for a certain cooling time t_c before the start of measurement. During an acquisition time t_m after the cooling time t_c, the γ-rays emitted from the activated foil are measured by a high-resolution HPGe detector. Only decay process occurs during the cooling time t_c and the acquisition time t_m. The number of measured counts ΔN is

$$\Delta N = \varepsilon_d \cdot \varepsilon_\gamma \cdot \varepsilon_t \cdot N(t_{irr}) \cdot e^{-\lambda t_c} \cdot \left(1 - e^{-\lambda t_m}\right) \tag{3.11}$$

where ε_t is the dead time correction, ε_γ is the gamma-ray intensity, and ε_d is the detector efficiency (given in Appendix A). The numbers of produced stable and unstable ($T_{1/2} =$ 3.08 h) nuclei under the condition of $Y = 1.32 \cdot 10^8$ s^{-1} as a function of time is shown in Fig. 3.5 with irradiation, cooling, and acquisition times, respectively.

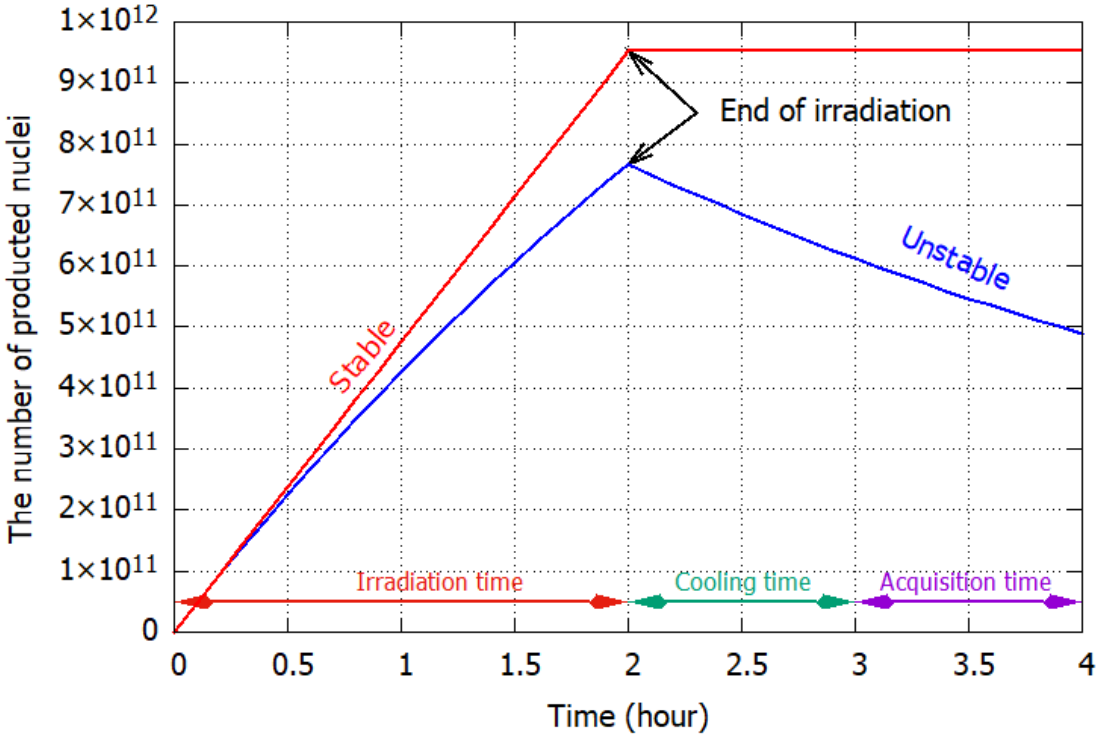

Fig. 3.5. The number of produced nuclei as a function of time during irradiation, cooling, and acquisition.

Finally, from Equations 2.6, 2.8, and 3.11, the production cross section σ is derived as follows:

$$\sigma = \frac{\Delta N \lambda}{n_T I_p \varepsilon_d \varepsilon_\gamma \varepsilon_t (1 - e^{-\lambda t_{irr}}) e^{-\lambda t_c} (1 - e^{-\lambda t_m})} \tag{3.12}$$

3.3.2 Self-absorption correction

The self-absorption effect in the target material causes a loss of γ-ray counting. This effect is particularly high for low-energy γ-rays in high-Z materials (Alfassi et al., 2009). It leads underestimation of the cross sections of the isotope of interest. The self-absorption in the foils can be estimated as:

$$A(E) = A_0(E)\frac{\rho[\mu(E)/\rho]x}{1 - exp[-\rho(\mu(E)/\rho)]x} \quad (3.13)$$

where $A_0(E)$ is the measured activity of the γ-ray at the energy E, A(E) is the corrected activity, x is the thickness of the foil, ρ is the density of the foil, μ(E)/ρ is the mass attenuation coefficient taken from the reference (Hubbel and Seltzer, 2004).

As an example, the self-absorption for the γ-line at 78.32 keV emitted from Sc foils (250 μm thickness) was estimated to be 1.5% from Equation 3.13. The mass attenuation coefficient is 0.40 cm^2/g.

3.3.3 X-ray interference from detector shielding

For low energy γ-lines, there can be the interference effect of X-rays from the detector shielding and other surrounding materials. Lead (Pb) was used as detector shielding. During γ-ray measurement, any radiation emitted from the activated foils could induce the X-ray fluorescence radiation at energies of E_{K_α}= 75 keV and E_{K_β} = 85 keV. It is better to minimize the interference as far as possible. In our experiments, the X-ray fluorescence radiations of Pb shielding would influence on the 78.32-keV γ-rays (Iγ = 96.4%) emitted from the decay of ^{44}Ti.

3.3.4 Isomeric decay contribution

A longer-lived metastable state of a radioactive nuclide of interest can be formed and it decays into a ground state by the Isomeric Transition (IT) process. Thus, the metastable state contributes to the γ-line of the ground state.

As an example, ^{44m}Sc ($T_{1/2}$= 58.61 h) can be formed directly by the (d,t) (E_{thr} = 5.07 MeV) and (d,p2n) (E_{thr} = -13.6 MeV) reactions on ^{45}Sc and decays to the ground state ^{44g}Sc ($T_{1/2}$= 3.97 h). The metastable state ^{44m}Sc ($I_p = 6^+$) decays to ^{44g}Sc ($I_p = 2^+$) by IT (98.8%) with emission of the γ-ray at 271 keV and to ^{44}Ca by EC (1.2%) with the γ-ray at 1157 keV. The strong γ-lines with the IT decay (98.8%) allow to determine the independent cross sections for ^{44m}Sc using measurements after adequate cooling times. The cross sections for ^{44g}Sc can be determined using the 1157-keV γ line, however the γ line includes the contribution from the EC decay of ^{44m}Sc (1.2%). Based on γ line intensities and detector efficiencies, the contribution to the 1157-keV γ line from the ^{44m}Sc EC decay can be estimated using that of the γ line at 271.24 keV (86.7%). The small contribution from the EC decay of ^{44m}Sc was subtracted.

The number of the ground state $N_g(t)$ during irradiation is contributed from the decay of the metastable state. The number of the metastable state $N_m(t)$ is

$$N_m(t) = \frac{Y_m}{\lambda_m}\left(1 - e^{-\lambda_m t}\right) \tag{3.14}$$

The time derivative of $N_g(t)$ is

$$\frac{dN_g(t)}{dt} = Y_g - N_g(t) \cdot \lambda_g + P_{m,g} \cdot N_m(t) \cdot \lambda_m \tag{3.15}$$

where $P_{m,g}$ is the isomeric transition coefficient and 0.988 for ^{44m}Sc.

By solving this equation, the cross section for the ground state, σ_g can be derived as follows:

$$\sigma_g = \left[\frac{\Delta N_{cumulative}}{n_T I \varepsilon_d \varepsilon_\gamma \varepsilon_t} - \frac{\sigma_m P_{m,g}}{g - \lambda_m}\left(\frac{\lambda_g}{\lambda_m}\Lambda_m - \frac{\lambda_m}{\lambda_g}\Lambda_g\right)\right]\frac{\lambda_g}{\Lambda_g} \tag{3.16}$$

$$\Lambda_m = \left(1 - e^{-\lambda_m t_{irr}}\right) \cdot e^{-\lambda_m t_c} \cdot \left(1 - e^{-\lambda_m t_m}\right) \tag{3.17}$$

$$\Lambda_g = \left(1 - e^{-\lambda_g t_{irr}}\right) \cdot e^{-\lambda_g t_c} \cdot \left(1 - e^{-\lambda_g t_m}\right) \tag{3.18}$$

where $\Delta N_{cumulative}$ is the measured counts of the photo-peak at 1157 keV, σ_m is the cross section for the meta-stable state, λ_m is the decay constant of the ^{44m}Sc and λ_g is the decay constant of the ^{44g}Sc.

The cross sections with and without correction are shown in Fig. 3.6. The cross sections were derived from the measurement of the 1157-keV γ line after cooling time of 27.5 h. The estimated contribution of the IT decay of ^{44m}Sc to ^{44g}Sc is about 35% at 23.3 MeV (discussed in section 5.3.5).

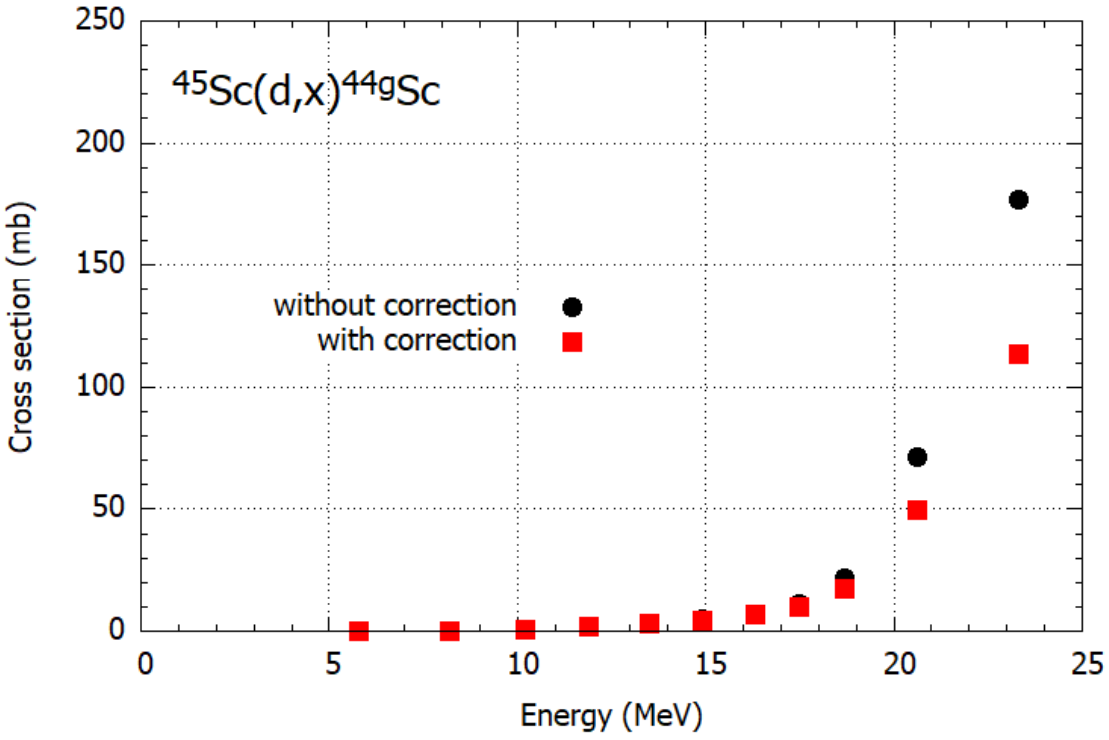

Fig. 3.6. The excitation functions of the ^{45}Sc(d,x)^{44m}Sc reaction with and without correction.

3.3.5 Overlapped γ-lines

Two or more radioactive nuclides that emit γ-rays with the same or close energy can be produced simultaneously in the foil. These γ-rays are considered as spectral overlapped ones because the peak area of the γ-rays in the spectra cannot be separated. Therefore, it is necessary to evaluate their individual contributions. An example is the overlap of γ-rays emitted from ^{44m}Sc and ^{44g}Sc produced in deuteron-induced reactions on scandium.

The γ-line of 1157 keV (I_γ=1.2%) of ^{44m}Sc overlaps with that of ^{44g}Sc (I_γ=99.9%) because these isotopes are coproduced and decay into the same nuclide ^{44}Ca. Thus, the contribution of the EC decay process of ^{44m}Sc should be subtracted from the collected count of the 1157.02 keV γ-line to derive the contribution of ^{44g}Sc. The contribution of ^{44m}Sc can be evaluated using the independent γ-rays at 271.24 keV (I_γ = 86.7%) using the following equations:

$$N_{\gamma_1} = \varepsilon_{d_1}\left(\varepsilon_{\gamma_1}^{m}\Delta N^{m}\right) \tag{3.19}$$

$$N_{\gamma_2} = \varepsilon_{d_2}\left(\varepsilon_{\gamma_2}^{g}\Delta N^{g} + \varepsilon_{\gamma_2}^{m}\Delta N^{m}\right) \tag{3.20}$$

$$\Delta N^{g} = \frac{1}{\varepsilon_{d_1}\varepsilon_{d_2}}\frac{\varepsilon_{d_1}\varepsilon_{\gamma_1}^{m}N_{\gamma_2} - \varepsilon_{d_2}\varepsilon_{\gamma_2}^{m}N_{\gamma_1}}{\varepsilon_{\gamma_1}^{m}\varepsilon_{\gamma_2}^{g}} \tag{3.21}$$

where ΔN^{m} and ΔN^{g} are the number of decays of ^{44m}Sc and ^{44g}Sc, N_{γ_1} and N_{γ_2} denote the net counts in photo-peaks at 271.24 (γ_1) and 1157 keV (γ_2), ε_{d_1} and ε_{d_2} are the detector efficiencies in the photo-peaks, $\varepsilon_{\gamma_2}^{g}$, $\varepsilon_{\gamma_1}^{m}$, and $\varepsilon_{\gamma_2}^{m}$ are the gamma ray branching ratios of ^{44m}Sc and ^{44g}Sc isotopes, respectively. The estimated contribution of the EC decay process of ^{44m}Sc is about 0.5% (discussed in section 5.3.5).

3.4 Uncertainty estimation

3.4.1 Uncertainty of cross section

According to Equation 2.10, experimental production cross sections depend on observables derived from the measurements (C, n_T, I_p, I_γ and ε_γ) and parameters such as decay constant, and γ-ray intensity, irradiation, cooling, and acquisition times.

The total relative uncertainty on the cross sections is estimated by the square root of the quadratic summation of the following components:

$$\Delta\sigma = \sqrt{(\Delta C)^2 + (\Delta n_T)^2 + \left(\Delta I_p\right)^2 + \left(\Delta I_\gamma\right)^2 + \left(\Delta \varepsilon_\gamma\right)^2} \tag{3.22}$$

where ΔC is the relative uncertainty of γ-ray counting, Δn_T is the relative uncertainty of the target thickness, $\Delta I_p$is the relative uncertainty of the beam intensity, ΔI_γ is the relative uncertainty of the γ-ray intensity and $\Delta \varepsilon_\gamma$ is the relative uncertainty of the detection efficiency. The uncertainties of the decay constant and times were ignored because of their negligible contribution in most experiments. Each component is independently estimated.

3.4.2 Uncertainty of beam energy

The uncertainty of the incident projectile energy depends on the conditions of the irradiation and the configuration of the foils in the target. The total relative uncertainty of the projectile energy can be estimated in the same way with that of the cross sections as follows:

$$\Delta E = \sqrt{(\Delta E_0)^2 + \sum_i (\Delta x_i)^2} \tag{3.23}$$

where ΔE_0 is the initial relative uncertainty on the determination of the incident projectile energy and Δx_i are various sources of the relative uncertainty such as the foil thicknesses, the stopping power and beam straggling effect.

In our experiments, the initial relative uncertainty on the deuteron beam energy, ΔE_0, is ± 0.1 MeV, which can be determined using the time-of-flight method (Watanabe *et al.*, 2014). This value is nearly the same relative uncertainty on the first foil. It increases gradually in the last foil of the stack due to the uncertainty propagation. The dominant reason for the increasing value is the struggling effect. The uncertainty of the initial beam energy relatively less affects the total one.

3.4.2.1 Energy straggling

Due to subsequent collisions with electrons in the foil, the beam loses its energy. Even though all the projectiles assumed to have the same incident energy, the energy of each projectile after passing through the foil can be changed from each other. This fluctuation effect is considered as the energy straggling (Ramirez *et al.*, 1969; Yang, O'Connor and Wang, 1991). If the energy loss distribution is similar to a Gaussian, the energy straggling can be defined by the standard deviation (Ma *et al.*, 2007) as follows

$$\sigma_{E_l}{}^2 = (E_l - \langle E_l \rangle)^2 \tag{3.24}$$

where $E_l = E_{in} - E_{out}$ is the energy loss in the foil and $\langle E_l \rangle$ is its mean value. The energy spread can be determined as full width at half maximum (FWHM) on the energy spectrum. Therefore, a relation between the full width at half maximum (FWHM) and the standard deviation, σ_{E_l}, is as

$$FWHM = 2.355 \cdot \sigma_{E_l} \tag{3.25}$$

3.4.2.2 Energy thickness

Charged-particle projectiles can lose their energies in the foil. The energy degradation from the incident energy E_{in} to the outgoing energy E_{out} depends on the thickness of the foil and is called the energy thickness. The measured cross section can be obtained for the energy thickness. The projectile energy at the midpoint of the foil E_{mid} is used for the cross section. Thus, the energy thickness is defined as E_{in}-E_{mid}.

CHAPTER 4: Production Cross Sections of ^{68}Ga in Deuteron-Induced Reactions on Natural Zinc

4.1 Introduction

^{68}Ga ($T_{1/2}$ = 67.71 min) is a positron emitter and suitable for PET scans (Banerjee and Pomper, 2013). It has the benefits of high sensitivity and resolution, repetitive examinations, and low radiation exposure to patients (Velikyan, 2018).

The parent ^{68}Ge ($T_{1/2}$ = 270.93 d) is longer lived and more appropriate for delivery than ^{68}Ga. Therefore, the ^{68}Ge/^{68}Ga generator is used to supply ^{68}Ga for nuclear medicine. The ^{68}Ga activity from the generator is however limited and unable to meet potential demand for ^{68}Ga (International Atomic Energy Agency, 2019). The (p,n) reaction on enriched ^{68}Zn is an preferable route on cyclotrons for large scale production of ^{68}Ga (e.g., Szelecsényi et al., 2012 and Lin et al., 2018; Riga et al., 2018). The deuteron-induced reactions on zinc are another candidate route for the ^{68}Ga production because the cross sections of the deuteron-induced reactions on zinc isotopes are comparable with those of the proton-induced ones according to the TENDL-2017 library (Koning and Rochman, 2012).

In the literature, there are a few experimental cross section data for the ^{nat}Zn(d,x)^{68}Ga reaction (Nassiff and Münzel, 1973; Šimečková et al., 2017) and the ^{68}Zn(d,2n)^{68}Ga reaction (Gilly et al., 1963). From the comparison of these results, however, a notable discrepancy among them is seen. Therefore, it is necessary to measure the reliable data of the cross sections to investigate the production route. In this experiment, we measured the production cross sections of ^{68}Ga and the radioactive by-products via deuteron-induced reactions on natural zinc. Their physical yields were also deduced from the measured cross sections.

4.2 Materials and Methods

The experiment was performed at the AVF cyclotron of the RIKEN RI Beam Factory. The production cross sections were derived using the stacked-foil activation technique and the high-resolution γ-ray spectrometry. The method of target preparation described in Section 3.1 is employed.

The stacked target consisted of pure metallic foils of Zn and Ti with natural isotopic composition. The foils of ^{nat}Zn with 99.9% purity and ^{nat}Ti with 99.6% purity were purchased from Nilaco Corp., Japan. The isotopic composition of natural zinc was ^{64}Zn: 49.17%, ^{66}Zn: 27.73%, ^{67}Zn: 4.04%, ^{68}Zn: 18.45%, and ^{70}Zn: 0.61%. The size and weight of the ^{nat}Zn and ^{nat}Ti foils were measured to determine the foils thicknesses. The thicknesses were found to be 17.64 mg/cm^2 and 9.31 mg/cm^2, respectively. The foils were cut into 10×10 mm^2 to fit a target holder served as a Faraday cup. Eleven sets of the Zn-Zn-Ti-Ti foils were stacked as the target and the configuration of the stacked foils is shown Fig. 4.1. To compensate recoil losses of the products, every second foil of Zn and Ti were measured.

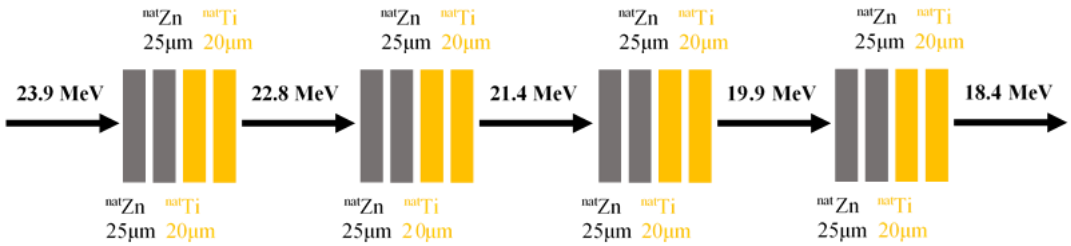

Fig. 4.1 Scheme of the stack foils. ^{nat}Ti foils are used as the monitor.

A deuteron beam of 23.9 MeV with an avarage intensity of 96 nA was irradiated on the stacked target for 22 minutes. The incident beam energy was measured by the time-of-flight method (Watanabe *et al.*, 2014). The uncertainty of the energy was estimated as ±0.1 MeV. The energy degradation and the uncertainty propagation along the stacked foils were calculated by the SRIM code (Ziegler, Biersack and Ziegler, 2008). The intensity was measured by the Faraday cup.

The γ-ray spectra of the irradiated foils were measured by a high-resolution HPGe detector (ORTEC GMX30P4-70) without chemical separation. The detector was

calibrated by a multiple γ-ray point source containing ^{57,60}Co, ^{88}Y, ^{109}Cd, ^{113}Sn ^{137}Cs, ^{139}Ce, and ^{241}Am. The measured γ-ray spectra were analyzed by the Gamma Studio software (SEIKO EG&G). Each foil was measured five times at maximum after cooling times of 40 min to 18 d to cover different half-lives of products. The distance between the detector and the foils was chosen in order to keep the dead time below 7%. The nuclear reaction and decay data for the γ-ray spectrometry are summarized in Table 4.1. All contributing reactions for the formation of the investigated radionuclides are also listed in Table 4.1.

Table 4.1: Nuclear reactions and decay data for reaction products (Pritychenko and Sonzongni, 2003; International Atomic Energy Agency, 2009; National Nuclear Data Center, 2017).

Nuclide	Half-life	Decay mode (%)	Eγ (keV)	Iγ (%)	Contributing reactions	Q-value (MeV)
^{68}Ga	67.71 min	ε+β^+(100)	1077.34	3.22(3)	^{66}Zn(d,γ)	11.3
					^{67}Zn(d,n)	4.3
					^{68}Zn(d,2n)	-5.9
					^{70}Zn(d,4n)	-21.6
^{67}Ga	3.2617 d	ε (100)	91.265	3.11(4)	^{66}Zn(d,n)	3.0
			93.310	38.81(3)	^{67}Zn(d,2n)	-4.0
			184.576	21.41(10)	^{68}Zn(d,3n)	-14.2
			208.950	2.460(10)		
			300.217	16.64(12)		
			393.527	4.56(24)		
^{66}Ga	9.49 h	ε+β^+(100)	833.5324	5.9(3)	^{64}Zn(d,γ)	10.8
			1039.220	37.0(20)	^{66}Zn(d,2n)	-8.2
					^{67}Zn(d,3n)	-15.2
^{65}Ga	15.2 min	ε+β^+(100)	53.93	4.9(10)	^{64}Zn(d,n)	1.7
			61.2	11.4(24)	^{66}Zn(d,3n)	-17.3
			115.09	54(13)		
			153.0	8.9(19)		
			206.9	2.5(5)		
			751.8	8.1(16)		
			768.9	1.3(3)		
			932.2	1.8(4)		
^{69m}Zn	13.756 h	β^- (99.97)	438.634	94.85(7)	^{68}Zn(d,p)	4.3
					^{70}Zn(d,t)	-3.0
^{65}Zn	243.93 d	ε+β^+(100)	1115.539	50.04(10)	^{64}Zn(d,p)	5.7
					^{66}Zn(d,t)	-4.8
					^{67}Zn(d,p3n)	-20.3
					^{65}Ga decay	
^{63}Zn	38.47 min	ε+β^+(100)	669.62	8.2(3)	^{64}Zn(d,t)	-5.6
			962.06	6.5 (4)	^{63}Ga decay	
^{61}Cu	3.339 h	ε+β^+(100)	67.4	4.2(8)	^{64}Zn(d,αn)	-1.4
			282.956	12.2(22)	^{66}Zn(d,α3n)	-20.4
			373.050	2.1(4)		
			588.605	1.17(21)		
			656.008	10.8(20)		
			908.631	1.10(20)		
			1185.234	3.7(7)		
^{58}Co	70.86 d	ε+β^+(100)	810.7593	99.450(10)	^{64}Zn(d,2α)	-2.1
					^{66}Zn(d,2n2α)	-16.9
Monitor reaction						
^{48}V	15.9735 d	ε +β^+(100)	944.13	7.870(7)	^{46}Ti(d,γ)	13.5
			983.52	99.98(4)	^{47}Ti(d,n)	4.6
			1312.11	98.2(3)	^{48}Ti(d,2n)	-7.0
					^{49}Ti(d,3n)	-15.2

The cross sections of the ^{nat}Ti(d,x)^{48}V monitor reaction were used to cross-check the beam intensity directly measured by the Faraday cup as described in Section 3.2.1. Measurements of the 983.5-keV γ-rays (I_γ = 99.98%) emitted from the the ^{48}V decay ($T_{1/2}$ = 15.9735 d) were used to determine the cross sections. The derived excitation function of the ^{nat}Ti(d,x)^{48}V reaction could be corrected using the beam intensity increased by 6.6% from the measured value by the Faraday cup. The corrected excitation function of the monitor reaction is presented in Fig. 4.2. This corrected beam intensity (102 nA) was adopted in the estimation of cross sections.

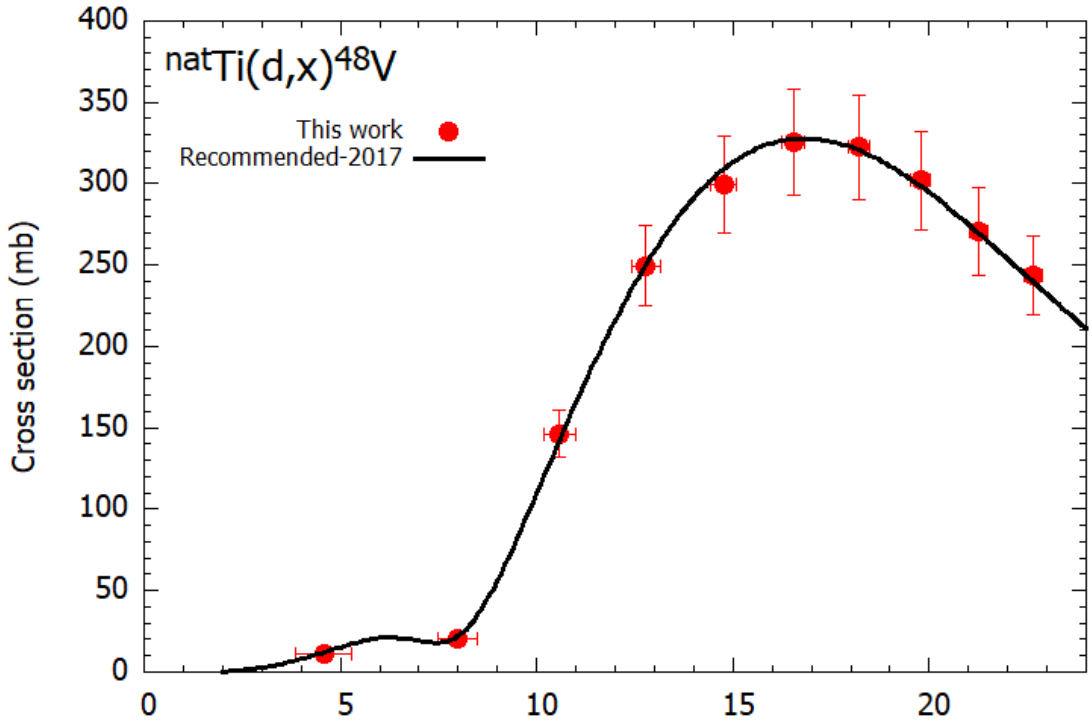

Fig. 4.2. The excitation function of the ^{nat}Ti(d,x)^{48}V monitor reaction compared with the recommended values (Hermanne *et al.*, 2018).

The uncertainties of the cross section and the beam intensity were estimated according to Equations 3.22 and 3.23. The estimated uncertainty on the beam energy of ± 0.1 MeV in the first foil is propagated to ± 0.9 MeV in the last foil of the stack. The total uncertainty of the cross sections was 10.0-32.1%. It was estimated from the following components: the beam intensity (7%), target thickness (2%), target purity (1%),

detector efficiency (6%), γ-intensity (<13%), γ-ray counting (0.5-30.5%), half-life (<5.6%), and peak fitting (3%).

4.3 Results and Discussions

In Table 4.2, the determined production cross sections of ^{65,66,67,68}Ga, ^{63,65,69m}Zn, ^{61}Cu, and ^{58}Co were summarized. Figures 4.3-4.11 show the results in comparison to previous experimental data available in the EXFOR Library (Otuka *et al.*, 2014) and theoretical estimation of TENDL-2017 (Koning and Rochman, 2012). The cross section values extracted from TENDL-2017 and the previous measured data on enriched zinc targets were normalized using the isotopic abundance of natural zinc.

Table 4.2: Measured cross sections and estimated uncertainty.

Energy (MeV)	Cross sections (mb)				
	^{68}Ga	^{67}Ga	^{66}Ga	^{65}Ga	^{69m}Zn
23.2±0.3	99.5±12.8	100.3±10.6	100.2±11.4	24.5±6.4	6.8±0.7
21.9±0.3	121.1±15.0	87.5±9.4	111.7±12.7	22.3±5.9	7.3±0.7
20.4±0.3	130.6±16.5	74.2±8.2	126.2±14.3	22.8±6.0	7.8±0.8
18.9±0.4	158.2±19.1	67.0±7.5	136.2±15.4	24.6±6.6	8.4±0.8
17.3±0.4	169.1±20.5	57.2±6.9	135.6±15.4	25.6±6.9	9.2±0.9
15.6±0.4	178.3±21.6	60.2±6.7	124.5±14.1	30.1±8.1	10.6±1.1
13.7±0.5	167.2±21.2	69.4±8.1	100.5±11.4	38.4±10.4	12.1±1.2
11.6±0.5	137.2±17.5	89.4±11.8	51.7±5.9	52.5±14.2	13.8±1.4
9.2±0.6	68.8±10.7	115.2±13.5	2.3±0.3	74.9±19.9	15.5±1.5
6.2±0.8	12.1±3.9	101.5±11.9		74.0±20.0	11.9±1.2
2.6±0.9		0.23±0.05			0.04±0.01
	^{65}Zn	^{63}Zn	^{61}Cu	^{58}Co	
23.2±0.3	175.9±17.7	60.9±7.2	45.2±9.6	4.0±0.4	
21.9±0.3	145.5±14.6	35.3±4.6	53.5±11.3	3.3±0.4	
20.4±0.3	119.9±12.1	23.0±3.4	54.7±11.6	2.9±0.3	
18.9±0.4	112.5±11.4	8.3±2.1	53.0±11.2	2.6±0.3	
17.3±0.4	117.8±11.9	8.2±2.4	45.1±9.6	1.8±0.2	
15.6±0.4	141.7±14.3	5.3±2.6	34.4±7.4	1.1±0.1	
13.7±0.5	174.9±17.6		23.6±5.3		
11.6±0.5	228.4±23.2		8.1±2.0		
9.2±0.6	299.4±30.2				
6.2±0.8	266.0±26.9				

4.3.1 The ^{nat}Zn(d,x)^{68}Ga reaction

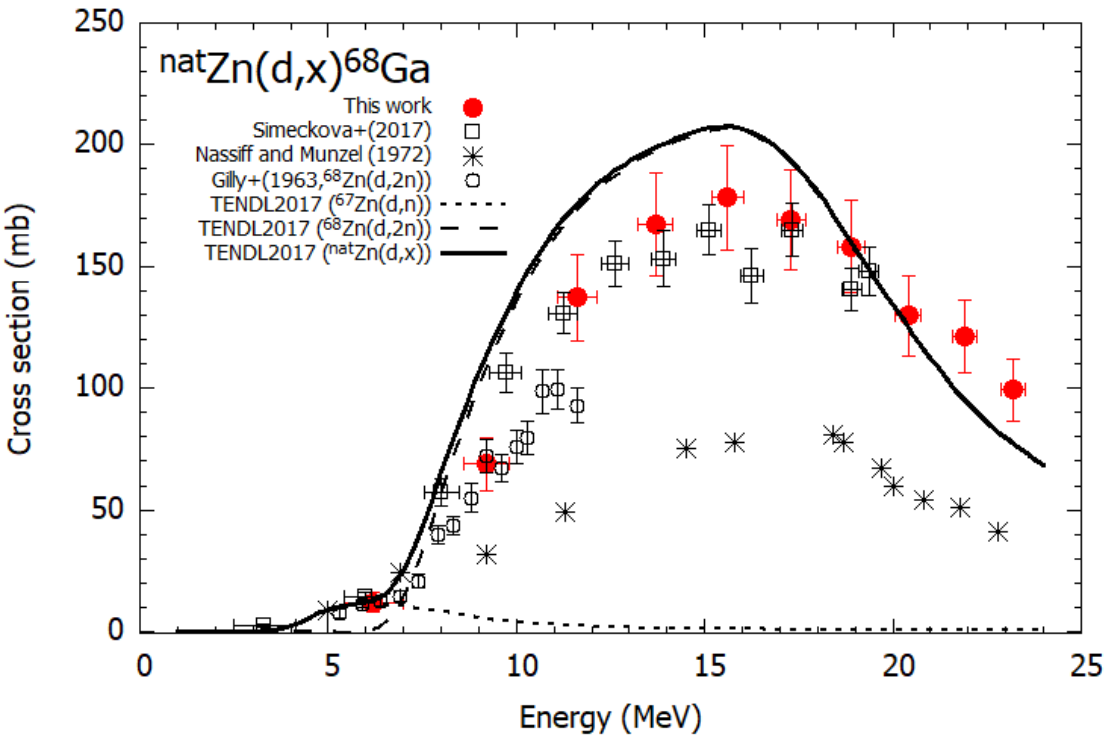

Fig. 4.3. The excitation function of the ^{nat}Zn(d,x)^{68}Ga reaction. The data on enriched ^{68}Zn are nomalized using the natural isotopic abundance.

The measurements of the 1077.34-keV γ-line (I_γ = 3.22%) from the ^{68}Ga decay ($T_{1/2}$ = 67.71 min) were used to derive the cross sections of the ^{nat}Zn(d,x)^{68}Ga reaction. The measured excitation function is shown in Fig. 4.3 in comparison with the previous experimental data on ^{nat}Zn (Nassiff and Münzel, 1972; Šimečková et al., 2017) and ^{68}Zn (Gilly et al., 1963) and the TENDL-2017 data (Koning and Rochman, 2012). In the whole energy region, our result is consistent with the recent data reported by Šimečková et al. (2017) but inconsistent with the data by Nassiff and Münzel (1972). The TENDL-2017 data overestimate the most experimental data. The main contribution comes from the (d,2n) reaction on ^{68}Zn above 6 MeV according to the TENDL-2017 data. The contribution from the (d,n) reaction on ^{67}Zn is expected to be minor. Consequently, the normalized data of the (d,2n) reaction on ^{68}Zn (Gilly et al., 1963) are reasonably consistent with the present result on ^{nat}Zn.

4.3.2 The ^{nat}Zn(d,x)^{67}Ga reaction

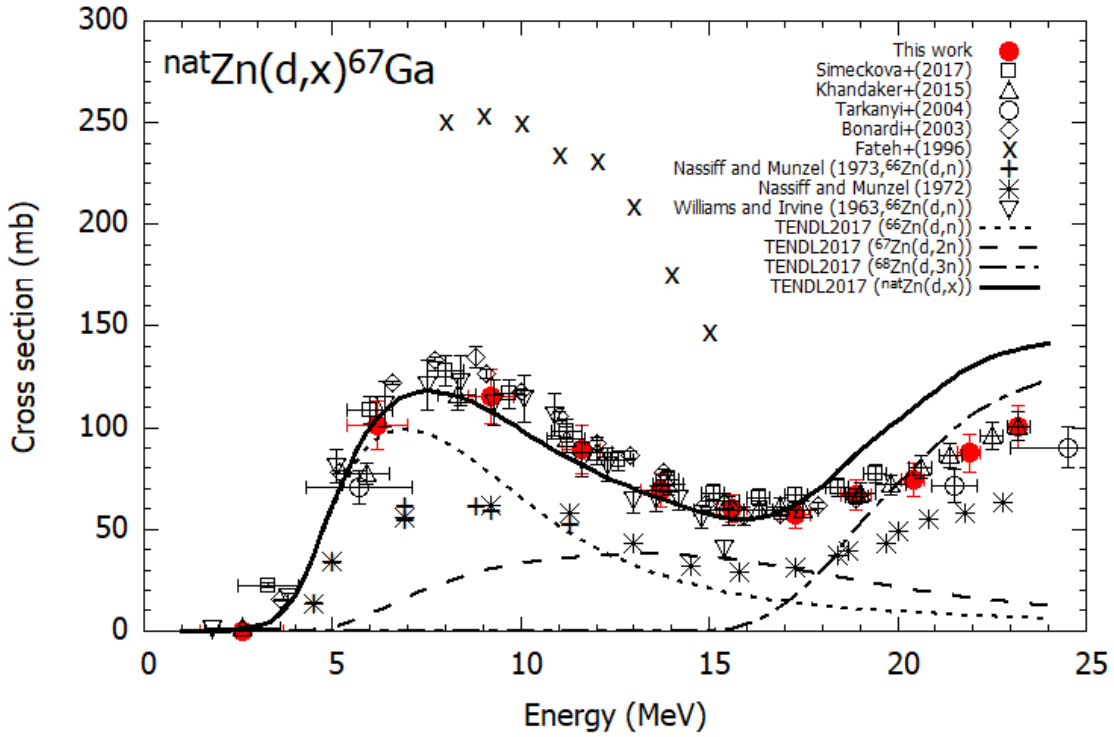

Fig. 4.4. The excitation function of the ^{nat}Zn(d,x)^{67}Ga reaction. The data on enriched ^{66}Zn are nomalized using the natural isotopic abundance.

The cross sections of the ^{nat}Zn(d,x)^{67}Ga reaction were derived from measurements of the 300.2-keV γ-line (I_γ = 16.64%) of ^{67}Ga. The contribution of the same γ-line (I_γ = 0.797%) of ^{67}Cu was found to be negligible according to the lack of its more intense γ-line at 184.576 keV (I_γ = 48.7%). The measured excitation function was shown in Fig. 4.4 in comparison with the experimental data on ^{nat}Zn (Bonardi et al., 2003; Fateh et al., 1996; Khandaker et al., 2015; Nassiff and Münzel, 1972; Šimečková et al., 2017; Tárkányi et al., 2004) and ^{66}Zn (Nassiff and Münzel, 1973; Williams and Irvine, 1963) and the TENDL-2017 data (Koning and Rochman, 2012).

Our result is in good agreement with previous data on natural zinc targets of Bonardi et al. (2003), Khandaker et al. (2015) and Šimečková et al. (2017). In the higher energy region, the data reported by Tárkányi et al. (2004) are slightly lower than ours. The data of Nassiff and Münzel (1972) show lower values while the data reported by Fateh et al. (1996) is much higher than the other experimental data. According to the TENDL-2017

prediction, the (d,n) reaction on ^{66}Zn contributes dominantly to the first peak around 8 MeV. The normalized data of the ^{66}Zn(d,n)^{67}Ga reaction by Williams and Irvine (1963) are in good agreement with our data, while those by Nassiff and Münzel (1973) are inconsistent. Up to 17 MeV, the TENDL-2017 data agree with our result. Above 17 MeV, the TENDL-2017 data show higher values than the present data probably due to overestimation of the ^{68}Zn(d,3n) reaction (E_{thr} = 16.4 MeV).

4.3.3 The ^{nat}Zn(d,x)^{66}Ga reaction

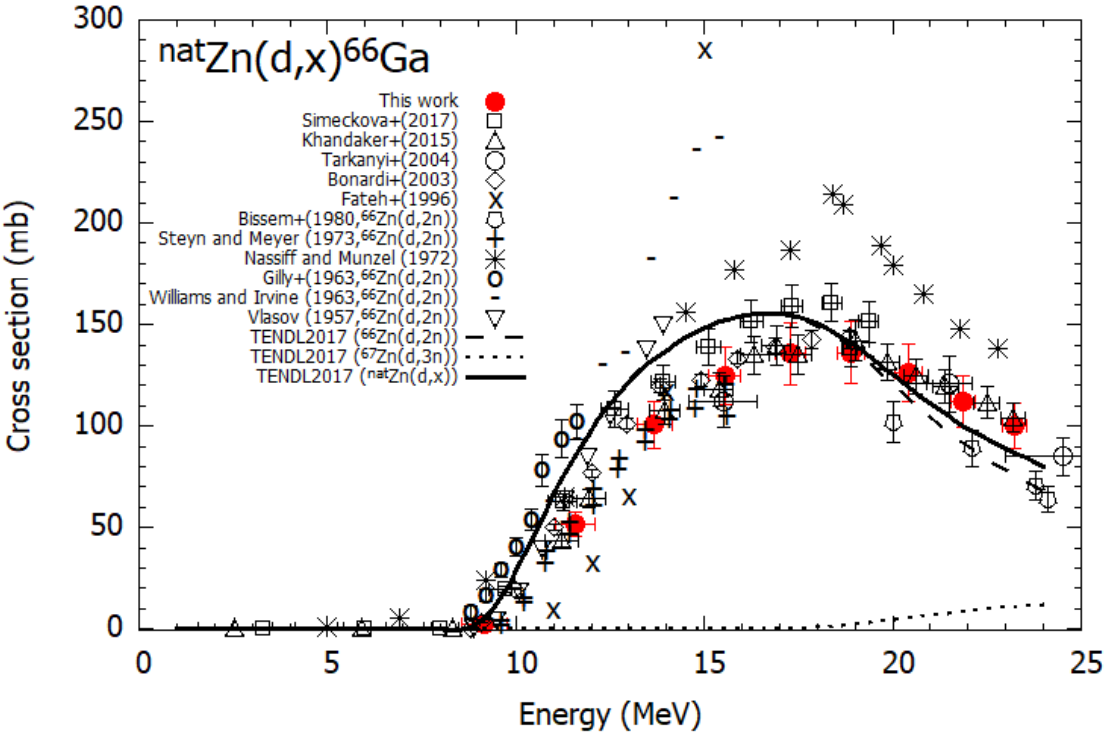

Fig. 4.5. The excitation function of the ^{nat}Zn(d,x)^{66}Ga reaction. The data on enriched ^{66}Zn are nomalized using the natural isotopic abundance.

The 1039.22-keV γ-line (I_γ = 37%) of ^{66}Ga was used to derive the cross sections of the ^{nat}Zn(d,x)^{66}Ga reaction. The present result is shown in Fig. 4.5 with the experimental data studied earlier on ^{nat}Zn (Bonardi et al., 2003; Fateh et al., 1996; Khandaker et al., 2015; Nassiff and Münzel, 1972; Šimečková et al., 2017; Tárkányi et al., 2004) and ^{66}Zn

(Bissem et al., 1980; Gilly et al., 1963; Steyn and Meyer, 1973; Vlasov et al., 1957; Williams and Irvine, 1963) and the TENDL-2017 data (Koning and Rochman, 2012).

Our result is consistent with the data on ^{nat}Zn reported by Khandaker et al. (2015), Tárkányi et al. (2004) and Bonardi et al. (2003). The recent data of Šimečková et al. (2017) are slightly higher than our result. The data of Fateh et al. (1996) and Nassiff and Münzel (1972) are completely inconsistent with the other data. The ^{66}Zn(d,2n)^{66}Ga reaction (E_{thr} = 8.4 MeV) is expected to be dominant in the energy region up to 20 MeV. The normalized data on ^{66}Zn can be compared with our data in the region. The data reported by Steyn and Meyer (1973) agree well with our measured excitation function. The data by Gilly et al. (1963) and Vlasov et al. (1957) are higher than our data. The data reported by Williams and Irvine (1963) show much higher values around the peak region. In the energy region above 16 MeV, the data reported by Bissem et al. (1980) show lower values than ours probably due to the lack of the contribution from the (d,3n) reaction on ^{67}Zn (E_{thr} = 15.7 MeV). The peak amplitude is consistent with the TENDL-2017 data, though the position slightly shifts to the lower energy.

4.3.4 The ^{nat}Zn(d,x)^{65}Ga reaction

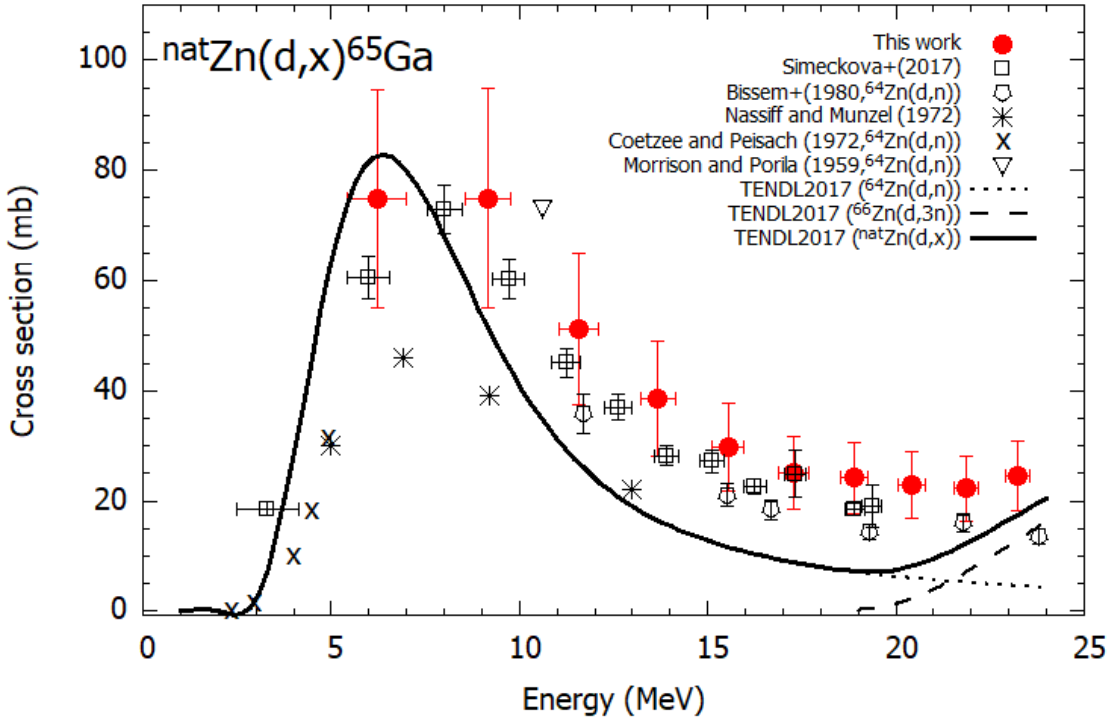

Fig. 4.6. The excitation function of the ^{nat}Zn(d,x)^{65}Ga reaction. The data on enriched ^{64}Zn are nomalized using the natural isotopic abundance.

The cross sections of the ^{nat}Zn(d,x)^{65}Ga reaction were derived from measurements of the 115.09-keV γ-line (I_γ=54%) of the radionuclide ^{65}Ga. The self-absorption of the γ-line was calculated as 0.4% using Equation 3.11 and found to be negligibly small.

The measured excitation function is shown in Fig. 4.6 together with the previous experimental data on ^{64}Zn (Bissem et al., 1980; Coetzee and Peisach, 1972; Morrison and Porile, 1959) and on ^{nat}Zn (Nassiff and Münzel, 1972; Šimečková et al., 2017) and the TENDL-2017 data (Koning and Rochman, 2012). Our data have a larger uncertainty than the others due to the relative uncertainty of the intensity (24%) of the 115.09-keV γ-line (International Atomic Energy Agency, 2009). In addition, due to the very short half-life of ^{65}Ga ($T_{1/2}$ = 15.2 min), its uncertainty (1.3%) is exceptionally considered. It causes the uncertainty of 1.8-5.6% in cross sections and increases the total uncertainty.

The present result shows an overall agreement with the data of Šimečková et al. (2017) while it disagrees with the data reported by Nassiff and Münzel (1972). Only the (d,n) reaction on ^{64}Zn produces ^{65}Ga below the threshold energy of the (d,3n) reaction on ^{66}Zn (E_{thr}=17.8 MeV). Morrison and Porile (1959) reported one cross section of the ^{64}Zn(d,n)^{65}Ga reaction at 10.6 MeV, of which data are comparable with our data. The normalized data of the ^{64}Zn(d,n)^{65}Ga reaction reported by Bissem et al. (1980) are slightly lower than the present data. The peak amplitude of the TENDL-2017 data agrees with our data within the uncertainty, however the peak position slightly shifts to the lower energy.

4.3.5 The $^{nat}Zn(d,x)^{69m}Zn$ reaction

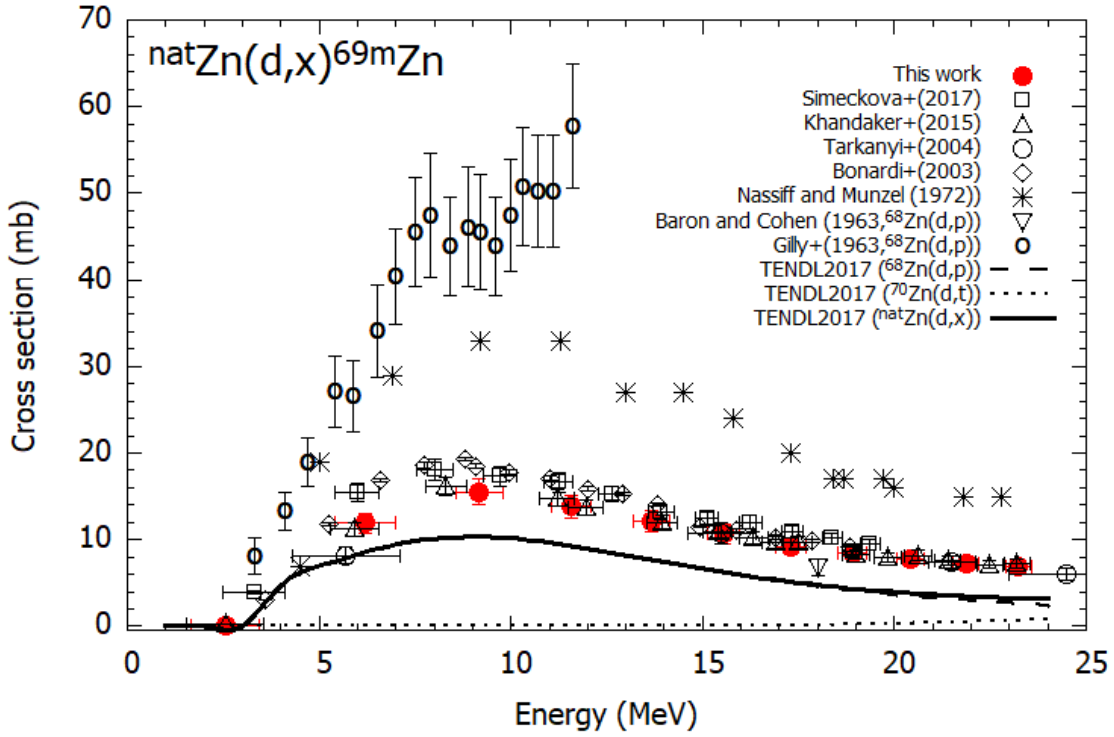

Fig. 4.7. The excitation function of the $^{nat}Zn(d,x)^{69m}Zn$ reaction. The data on enriched ^{68}Zn are nomalized using the natural isotopic abundance.

The cross sections of the $^{nat}Zn(d,x)^{69m}Zn$ reaction were derived from the measurement of the 438.63-keV γ-line (I_γ = 94.85%) emitted from the decay of the meta-stable state ($T_{1/2}$ = 13.8 h) of the radionuclide ^{69}Zn. The measured excitation function is shown in Fig. 4.7 in comparison with the previous experimental data on ^{68}Zn (Baron and Cohen, 1963; Gilly et al., 1963) and on ^{nat}Zn (Bonardi et al., 2003; Khandaker et al., 2015; Nassiff and Münzel, 1972; Šimečková et al., 2017; Tárkányi et al., 2004), and the TENDL-2017 data (Koning and Rochman, 2012).

The present data are in an overall agreement with the data of Bonardi et al. (2003), Khandaker et al. (2015), Šimečková et al. (2017), and Tárkányi et al. (2004). The data reported by Nassiff and Münzel (1972) are much higher than the other experimental data. Based on the TENDLE-2017 prediction, the (d,p) reaction on ^{68}Zn gives the main contribution in our experimental energy region. Among the data using the enriched ^{68}Zn targets, the data of Gilly et al. (1963) completely disagree with our data. The data reported

by Baron and Cohen (1963) at 18 MeV is slightly lower than ours. The TENDL-2017 data underestimate all the experimental data.

4.3.6 The ^{nat}Zn(d,x)^{65}Zn reaction

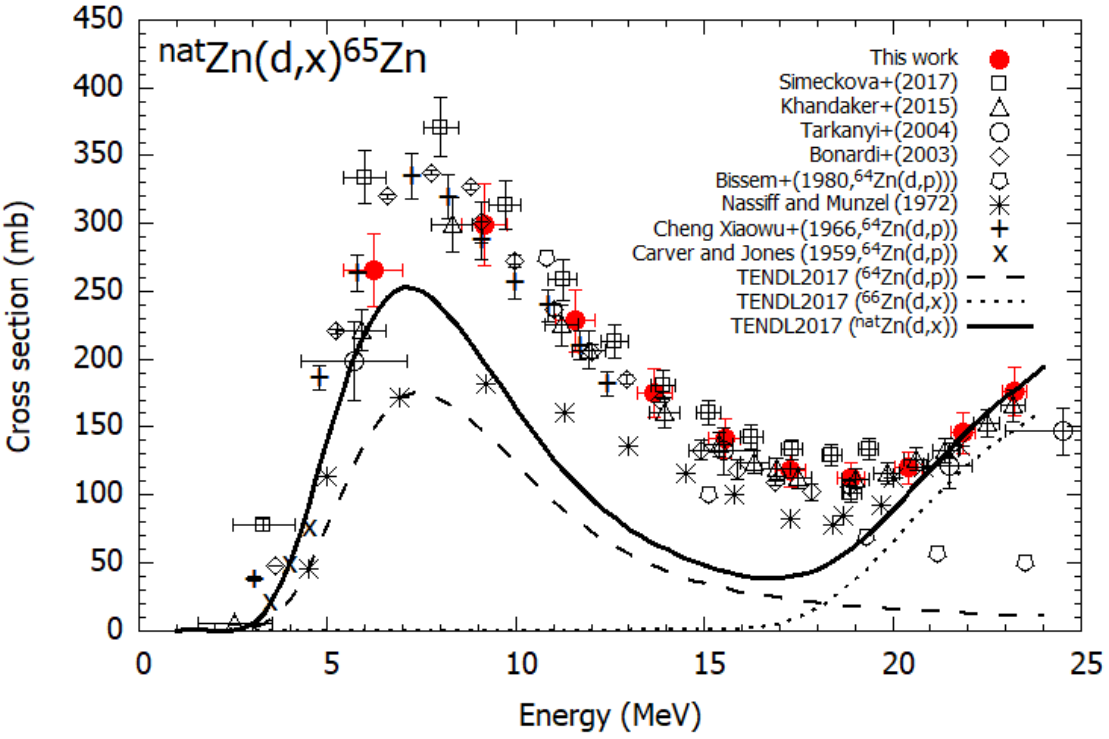

Fig. 4.8. The excitation function of the ^{nat}Zn(d,x)^{65}Zn reaction. The data on enriched ^{64}Zn are nomalized using the natural isotopic abundance.

In addition to the direct reactions, ^{65}Zn ($T_{1/2}$ = 243.93 d) can be produced from the decay of co-produced ^{65}Ga ($T_{1/2}$ = 15.2 min). The measured cross sections are cumulative ones because ^{65}Ga has completely decayed during the cooling time of around 18 days. The cross sections were derived from the measurement of the 1115.59-keV γ-line (I_γ = 50.04%) of ^{65}Zn and shown in Fig. 4.8. The result is compared with the experimental data studied earlier on ^{64}Zn (Bissem et al., 1980; Carver and Jones, 1959; Xiaowu et al., 1966) and on ^{nat}Zn (Bonardi et al., 2003; Khandaker et al., 2015; Nassiff and Münzel, 1972; Šimečková et al., 2017; Tárkányi et al., 2004), and the TENDL-2017 data (Koning and Rochman, 2012).

Our result is consistent with the recent data of Bonardi et al. (2003), Khandaker et al. (2015), Šimečková et al. (2017) and Tárkányi et al. (2004) but inconsistent with the data of Nassiff and Münzel (1973) below 20 MeV. The present result agrees with the normalized data on ^{64}Zn reported by Xiaowu et al. (1966). It would indicate that the (d,p) reaction on ^{64}Zn is dominant at the first peak. The data by Bissem et al. (1980) on ^{64}Zn show lower values than our data in the energy region above 15 MeV. This tendency in the higher energy region may be caused by the lack of the contribution from the reaction on ^{66}Zn. The TENDL-2017 data underestimate the contribution of the (d,p) reaction on ^{64}Zn.

4.3.7 The ^{nat}Zn(d,x)^{63}Zn reaction

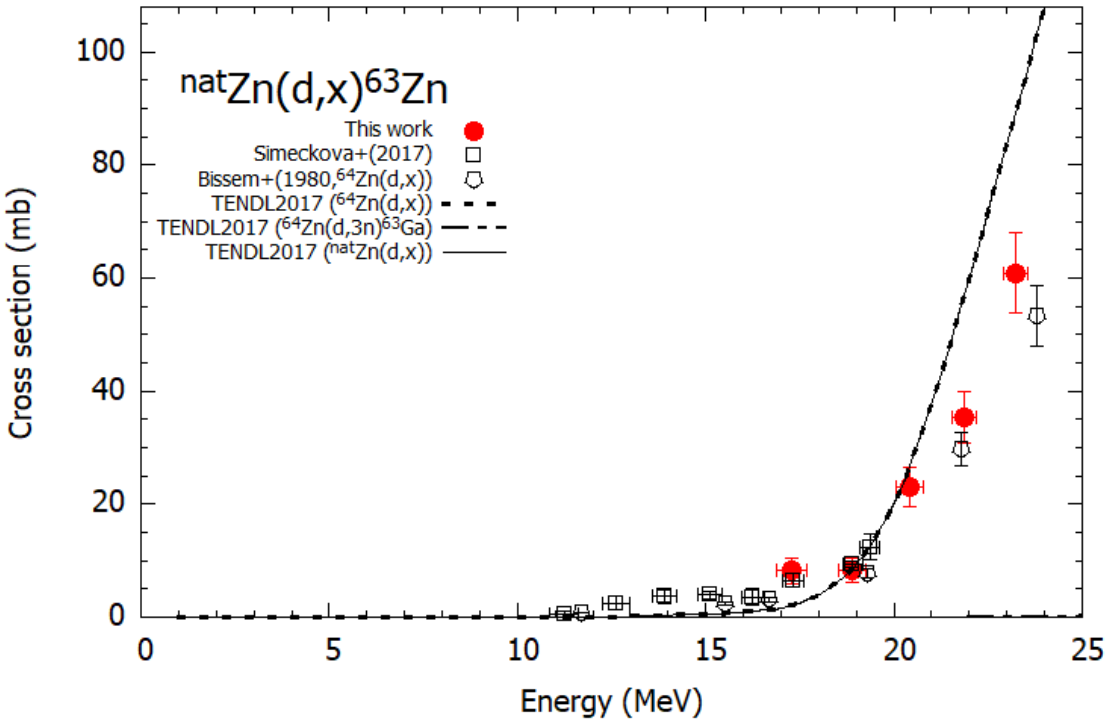

Fig. 4.9. The excitation function of the ^{nat}Zn(d,x)^{63}Zn reaction. The data on enriched ^{64}Zn are nomalized using the natural isotopic abundance.

^{63}Zn ($T_{1/2}$ = 38.5 min) can be produced from direct production of the ^{nat}Zn(d,x)^{63}Zn reaction and the decay of ^{63}Ga ($T_{1/2}$ = 32.4 sec) formed by the ^{64}Zn(d,3n)^{63}Ga reaction (E_{thr} = 21.2 MeV). Therefore, the measured cross sections are cumulative. The excitation

function of the ^{nat}Zn(d,x)^{63}Zn reaction was derived from the measurement of the 669.62-keV γ-line (I_γ = 8.2%) of the radionuclide ^{63}Zn and shown in Fig. 4.9 and compared with previous experimental data on ^{64}Zn (Bissem et al., 1980) and on ^{nat}Zn (Šimečková et al., 2017), and the TENDL-2017 data (Koning and Rochman, 2012). The present data are consistent with the data of Šimečková et al. (2017). Bissem et al. (1980) reported the cumulative cross section of the (d,x) reactions on ^{64}Zn and their normalized data show slightly lower values than our data. The TENDL-2017 data partially agree with experimental values at around 20 MeV.

4.3.8 The ^{nat}Zn(d,x)^{61}Cu reaction

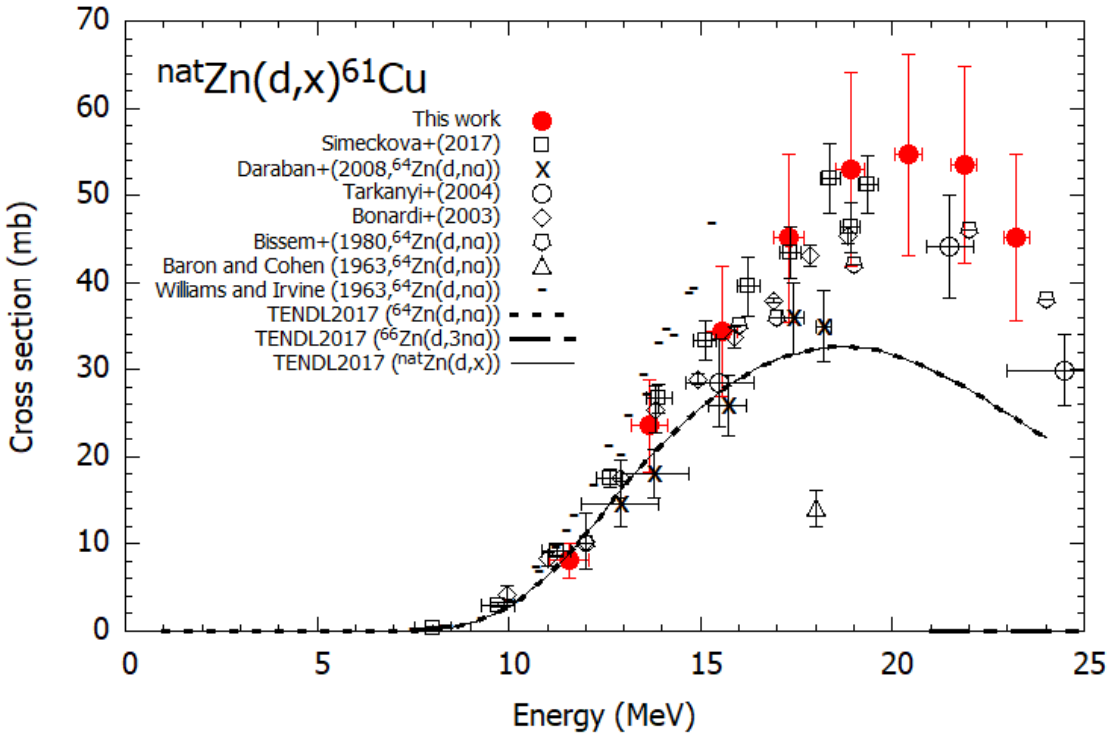

Fig. 4.10. The excitation function of the ^{nat}Zn(d,x)^{61}Cu reaction. The data on enriched ^{64}Zn are nomalized using the natural isotopic abundance.

The cross sections of the ^{nat}Zn(d,x)^{61}Cu reaction were determined using the 282.96-keV γ-line (I_γ = 12.2%) of ^{61}Cu. The relative uncertainty of the γ-line is 18%

(International Atomic Energy Agency, 2009), which is a major source of the total uncertainty of the cross sections. The result is shown in Fig. 4.10 in comparison with the previous experimental data on ^{64}Zn (Baron and Cohen, 1963; Bissem et al., 1980; Daraban et al., 2008; Williams and Irvine, 1963) and on ^{nat}Zn (Bonardi et al., 2003; Šimečková et al., 2017; Tárkányi et al., 2004), and the TENDL-2017 data (Koning and Rochman, 2012).

The present result agrees with the data studied using natural zinc targets by Šimečková et al. (2017), Bonardi et al. (2003), and Tárkányi et al. (2004). The result is also compared with the data studied using enriched ^{64}Zn because only the (d,nα) reaction on ^{64}Zn (E_{thr} = 1.4 MeV) contributes to ^{61}Cu production below the threshold energy of the ^{66}Zn(d,3nα)^{61}Cu reaction (E_{thr} = 21.04 MeV). The normalized data of Bissem et al. (1980) and Daraban et al. (2008) show slightly lower values than our data. The normalized data of Baron and Cohen (1963) is too low while those of Williams and Irvine (1963) show higher values than ours. The TENDL-2017 data give lower values than the experimental data.

4.3.9 The ^{nat}Zn(d,x)^{58}Co reaction

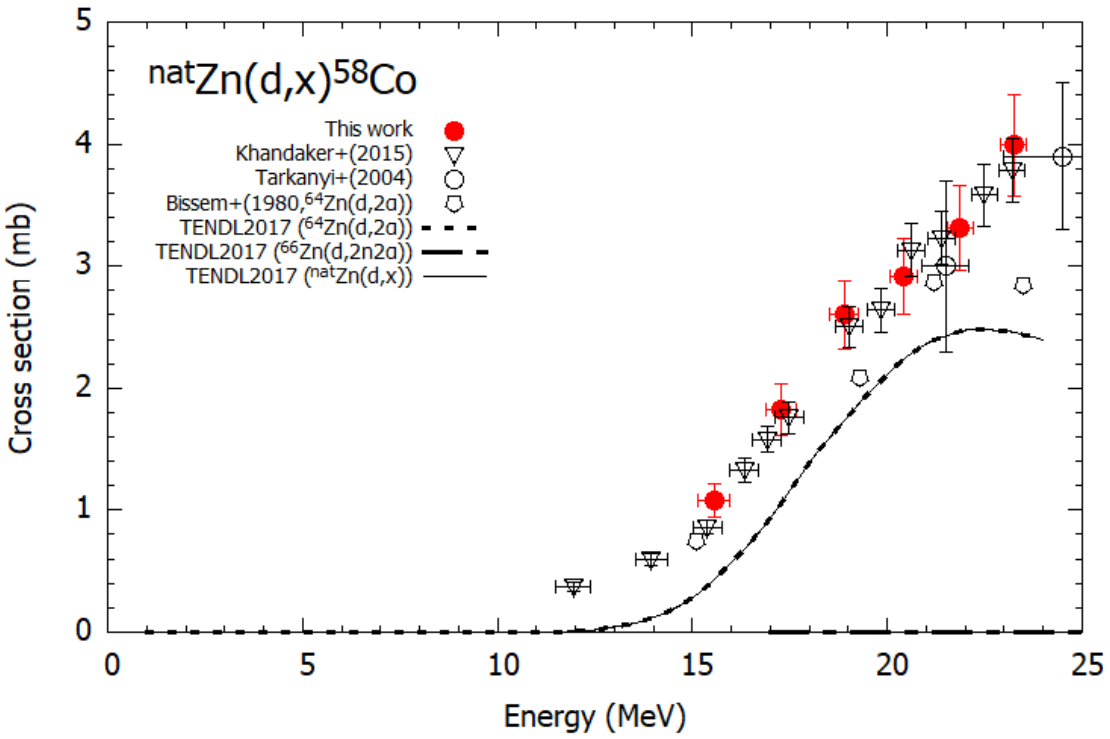

Fig. 4.11. The excitation function of the ^{nat}Zn(d,x)^{58}Co reaction. The data on enriched ^{64}Zn are nomalized using the natural isotopic abundance.

There is a meta-stable state ($T_{1/2}$ = 9.10 h) of ^{58}Co, which decays to the ground state ($T_{1/2}$ = 70.86 d) during a cooling time of about 18 days. Therefore, the cumulative cross sections of the ^{nat}Zn(d,x)^{58}Co reaction were derived from the measurement of the 810.76-keV γ-line (I_γ = 99.45%) of the ground state. The excitation function for the ^{58}Co production is shown in Fig. 4.11 and compared with the previous experimental data on ^{64}Zn (Bissem et al., 1980) and on ^{nat}Zn (Khandaker et al., 2015; Tárkányi et al., 2004), and the TENDL-2017 data (Koning and Rochman, 2012).

The present result agrees with both data on ^{nat}Zn of Khandaker et al. (2015) and Tárkányi et al. (2004). In our experimental energy region, the (d,2α) reaction on ^{64}Zn (E_{thr} = 0.0 MeV) is dominant. The (d,2n2α) reaction on ^{66}Zn (E_{thr} = 17.4 MeV) can contribute to the ^{58}Co production in higher energy region. The normalized data of the ^{64}Zn(d,2α)^{58}Co reaction by Bissem et al. (1980) show lower values than our data probably due to the lack of the contribution from the ^{66}Zn(d,2n2α) reaction. The TENDL-2017 data show lower values than all the experimental data.

4.3.10 Physical yields

Physical yields (Otuka and Takács, 2015) of ^{65,66,67,68}Ga, ^{63,65,69m}Zn, ^{61}Cu and ^{58}Co were deduced from spline fitted curves of the measured excitation functions and stopping powers calculated by the SRIM code (Ziegler, Biersack and Ziegler, 2008). The deduced physical yields are shown in Figs. 4.12-4.18 and compared with data available in the EXFOR Library (Otuka *et al.*, 2014). Deviations of our results from some of the experimental data are partly caused by the calculation adopted in this work.

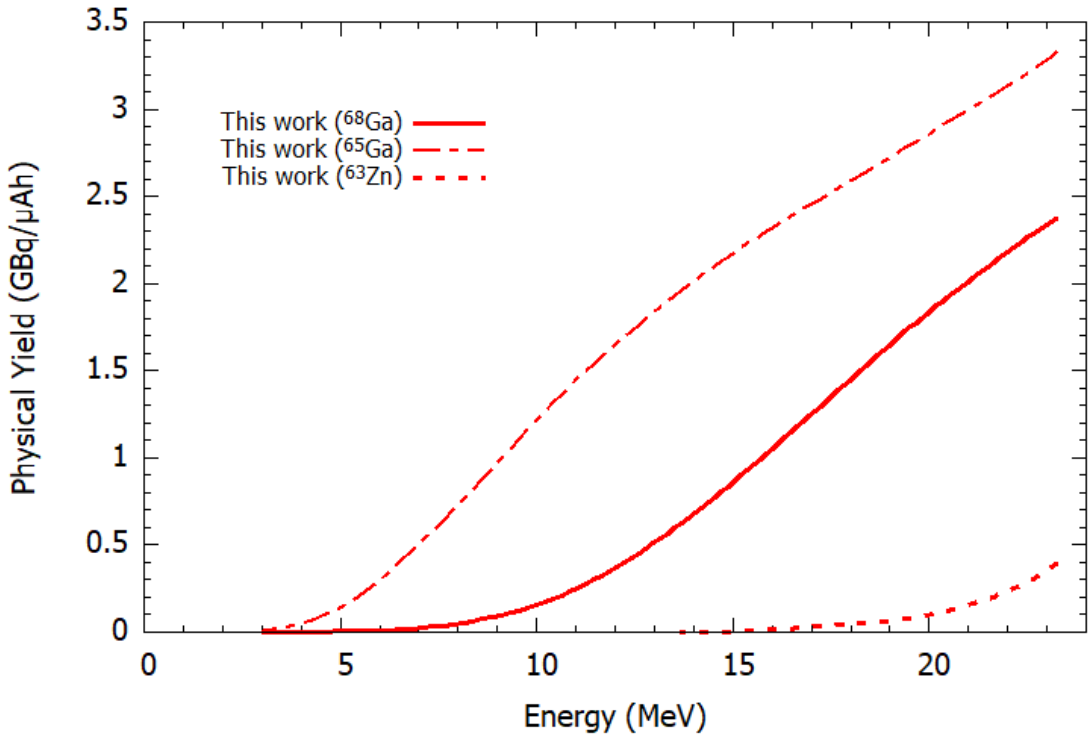

Fig. 4.12. The physical yields of ^{65}Ga, ^{68}Ga and ^{63}Zn via the deuteron-induced reactions on ^{nat}Zn.

The physical yields of the short-lived radionuclides ^{65}Ga, ^{68}Ga and ^{63}Zn are shown in Fig. 4.12. There are no experimental data found in our literature survey. The physical yields of ^{65}Ga, ^{68}Ga and ^{63}Zn were reported for the first time.

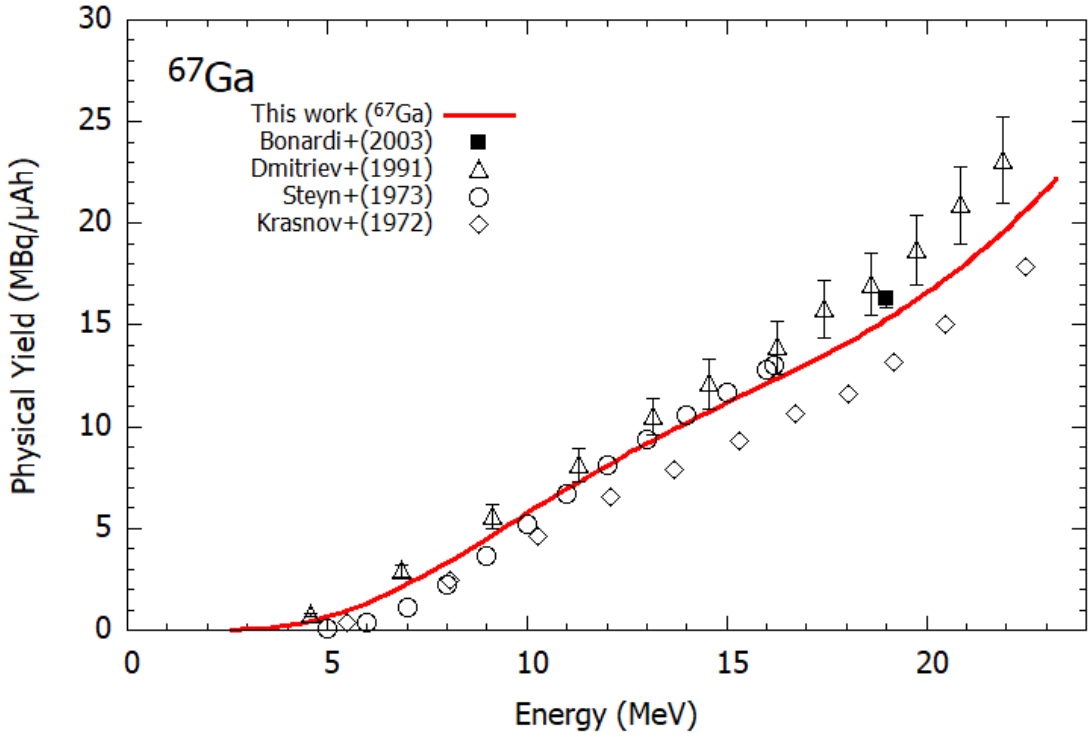

Fig. 4.13. The physical yield of ^{67}Ga via the deuteron-induced reactions on ^{nat}Zn.

The physical yield of ^{67}Ga is presented in Fig. 4.13 in comparison with the previous experimental data (Bonardi et al., 2003; Dmitriev et al., 1991; Krasnov et al., 1972; Steyn and Meyer, 1973). The data by Dmitriev et al. (1991) and Bonardi et al. (2003) show higher values than ours at the higher energy region. Our yield curve shows a partial agreement with the yields reported by Steyn and Meyer (1973). The data by Krasnov et al. (1972) present systematically lower values than our data.

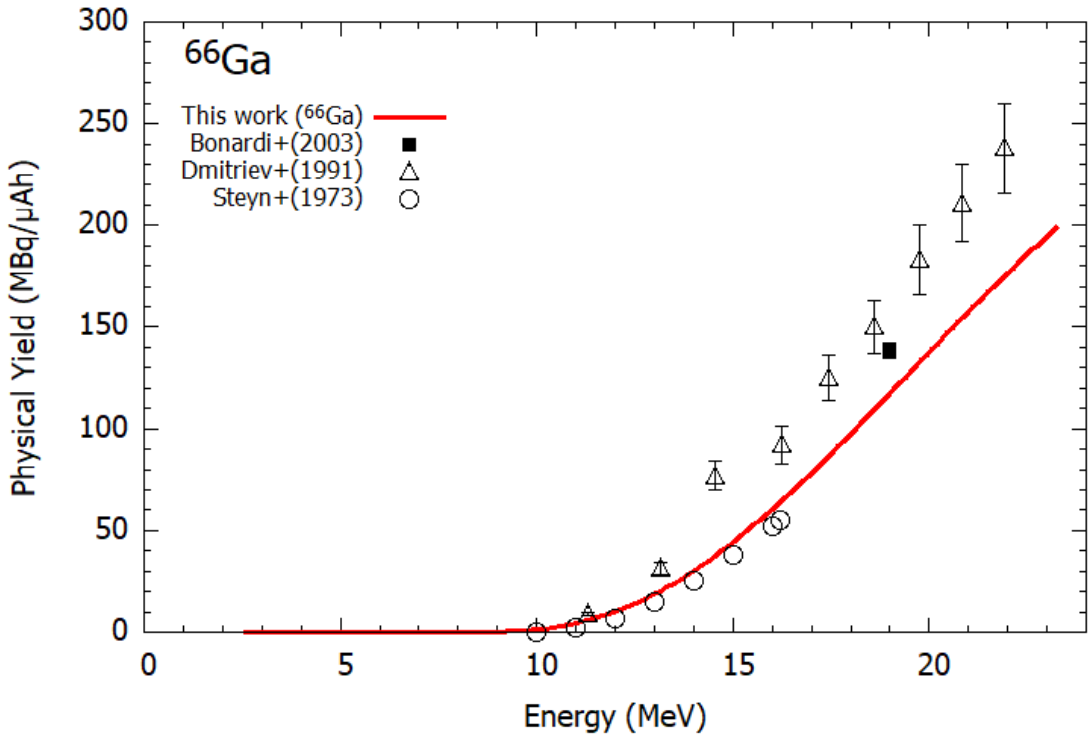

Fig. 4.14. The physical yield of ^{66}Ga via the deuteron-induced reactions on ^{nat}Zn.

Figure 4.14 shows the physical yield of ^{66}Ga in comparison with the previous experimental data (Bonardi et al., 2003; Dmitriev et al., 1991; Steyn and Meyer, 1973). Our result agrees with the yields reported by Steyn and Meyer (1973). However, the data reported by Dmitriev et al. (1991) and those of Bonardi et al. (2003) at 19 MeV show systematically higher values than ours.

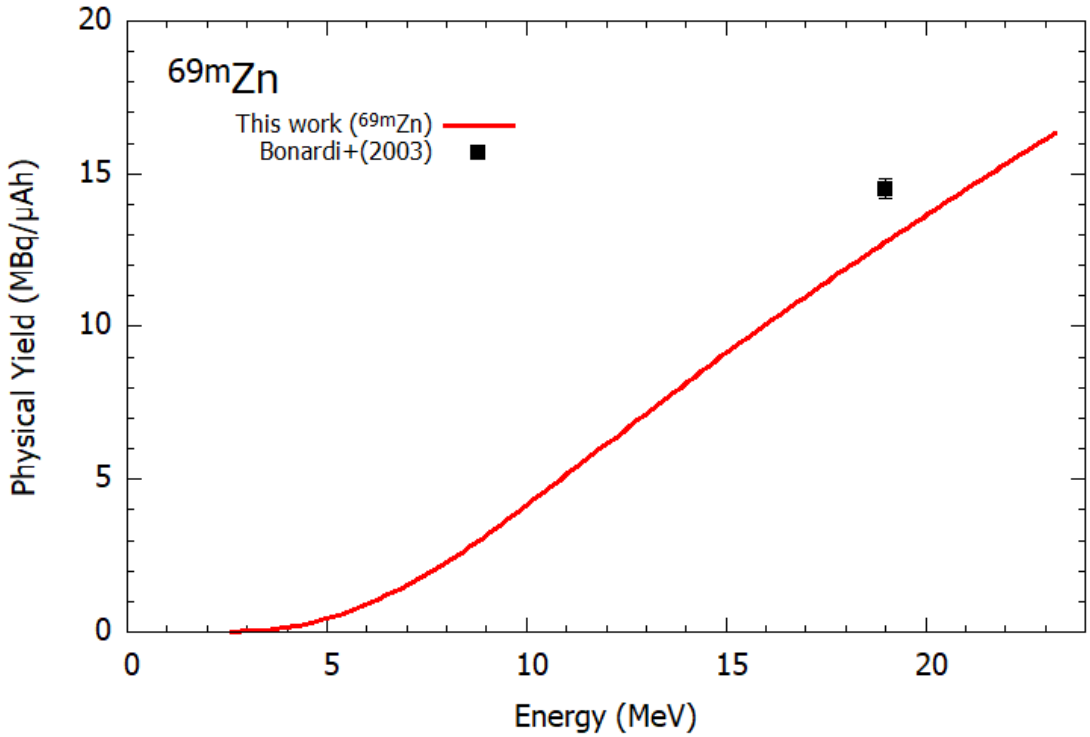

Fig. 4.15. The physical yield of ^{69m}Zn via the deuteron-induced reactions on ^{nat}Zn

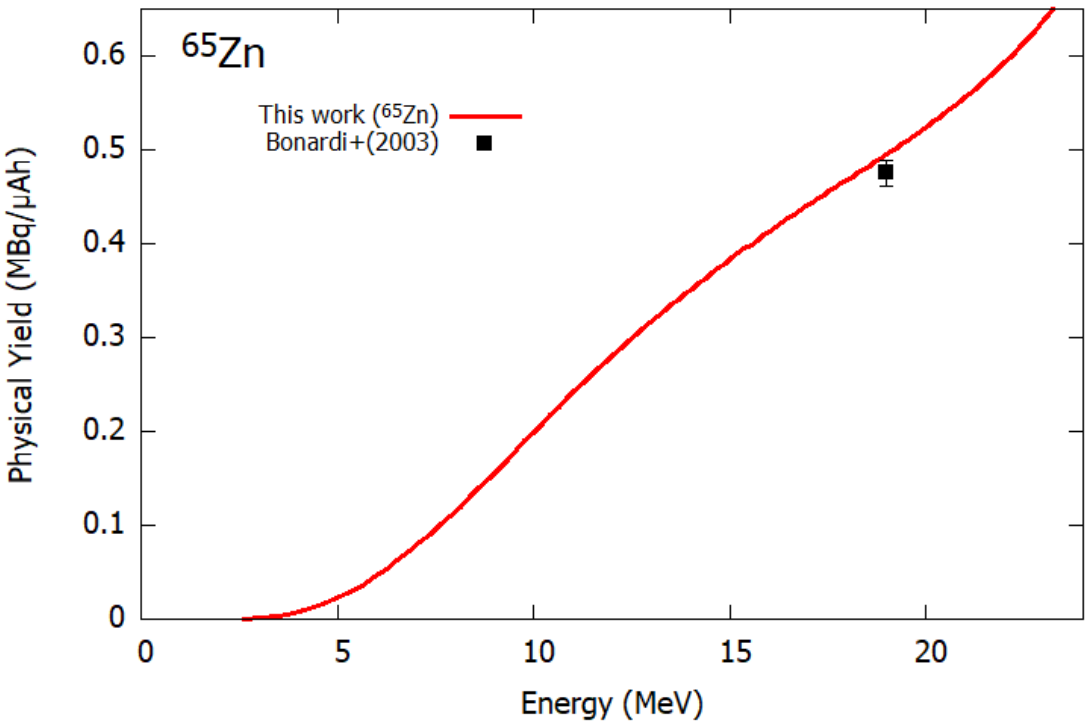

Fig. 4.16. The physical yield of ^{65}Zn via the deuteron-induced reactions on ^{nat}Zn.

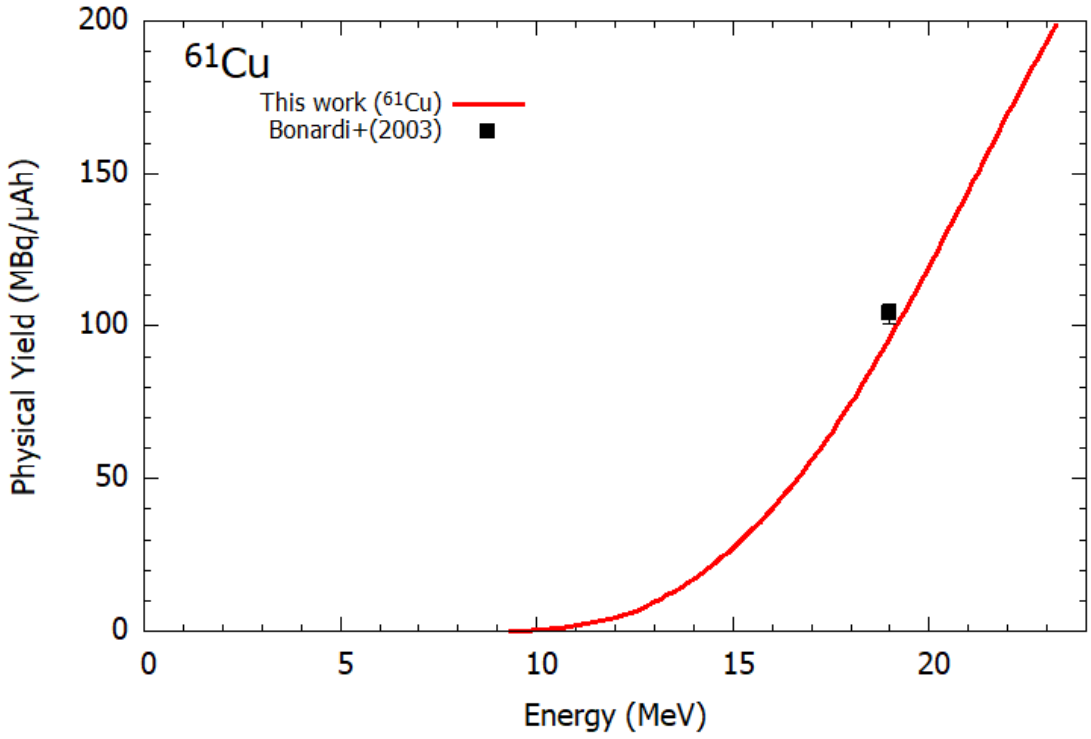

Fig. 4.17. The physical yield of ^{61}Cu via the deuteron-induced reactions on ^{nat}Zn

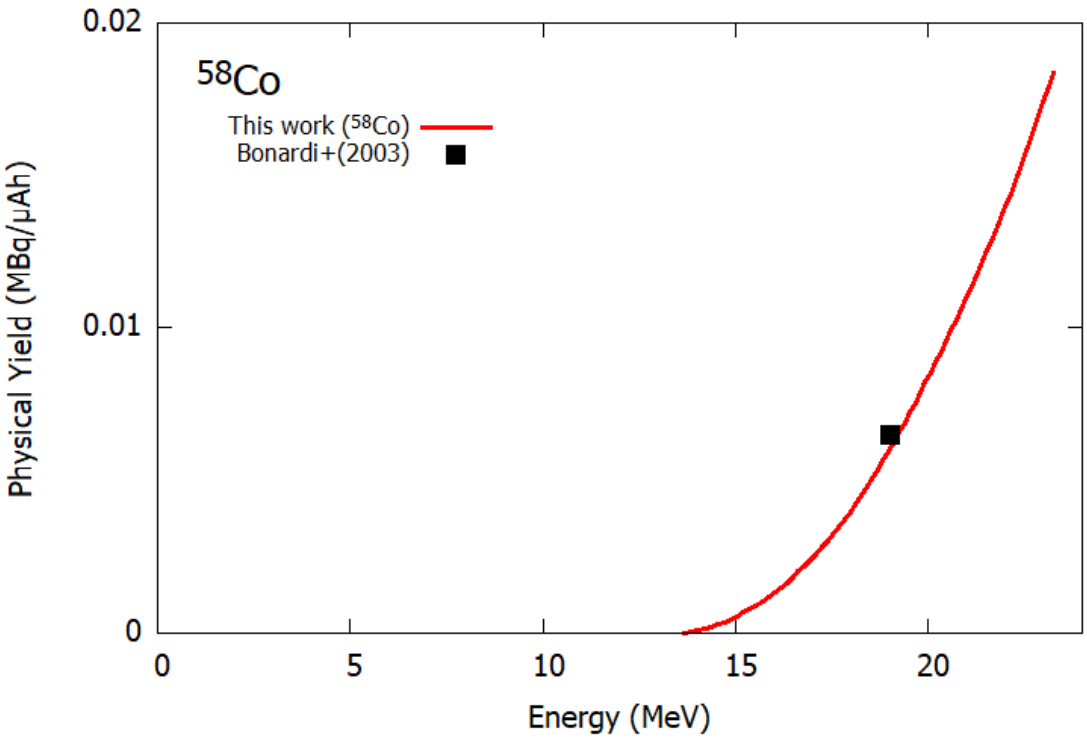

Fig. 4.18. The physical yield of ^{58}Co via the deuteron-induced reactions on ^{nat}Zn.

The physical yields of ^{69m}Zn, ^{65}Zn, ^{61}Cu and ^{58}Co are shown in Figs. 4.15-4.18 with the previous data at 19 MeV (Bonardi et al., 2003). Our data agree with the previous data except for ^{69m}Zn. The previous data of ^{69m}Zn are higher than ours.

4.3.11 Comparison of proton- and deuteron-induced reactions

Based on the deduced physical yields, the best production reaction of ^{68}Ga for practical use can be discussed. The yields of ^{68}Ga using two reactions, proton- and deuteron-induced reactions on ^{68}Zn, are compared. The yield of the ^{68}Zn(d,2n)^{68}Ga reaction is deduced from that of the ^{nat}Zn(d,x) ^{68}Ga reaction obtained in section 4.3.1 and assumption of negligibly small contribution of the ^{67}Zn(d,n)^{68}Ga reaction. The yield of the ^{68}Zn(p,n)^{68}Ga reaction is obtained from the previous study (Szelecsényi *et al.*, 1998). The two yields at the threshold energies of the reactions to produce the radioactive impurity ^{67}Ga were 5.6 and 4.2 GBq/μAh for 12.2-MeV proton- and 14.6-MeV deuteron-induced reactions, respectively. Based on the comparison, the 12.2-MeV proton-induced reaction on enriched ^{68}Zn with chemical separation is probably better to produce ^{68}Ga without radioactive impurity. However, the conclusion can be changed if small amount of ^{67}Ga can be accepted.

4.4 Summary

The excitation functions for the production of ^{68}Ga and by-products such as ^{65,66,67}Ga, ^{63,65,69m}Zn, ^{61}Cu and ^{58}Co via the deuteron-induced reactions on natural zinc were measured up to 24 MeV. The stacked-foil activation technique and the high-resolution γ-ray spectrometry were used for the cross section measurements. The measured data were compared with previous experimental data and the TENDL-2017 data. The derived excitation function of the ^{nat}Zn(d,x)^{68}Ga reaction is consistent with the data of Šimečková et al. (2017). The measured cross sections of the other investigated radionuclides show also good agreements with the recently reported data. The physical yields deduced from measured cross sections partially agree with the previous data. The data obtained in this work are useful to consider the best reaction to produce ^{68}Ga for practical use.

CHAPTER 5: Production Cross Sections of ^{45}Ti in Deuteron-Induced Reaction on ^{45}Sc up to 24 MeV

5.1 Introduction

The radionuclide ^{45}Ti ($T_{1/2}$=3.08 h) is a positron emitter ($E_{\beta+}^{max}$ = 1040 keV, $E_{\beta+}^{ave}$ = 439 keV, $I_{\beta+} = 84.8\%$) (National Nuclear Data Center, 2019). The maximum and average energies of emitted positrons are comparable to those from ^{11}C and smaller than those of ^{15}O and appropriate for the small animal PET (Vavere, Laforest and Welch, 2005). This PET isotope can be used to investigate of titanium leaking of medical implants (Kim *et al.*, 2019) as well as for the study of the neurotoxicity of titanium dioxide nanoparticles (Song *et al.*, 2015) and in other applications. At low energy cyclotrons, the deuteron-induced reaction on a monoisotopic ^{45}Sc target is a possible route to produce this radionuclide. In our literature survey, however, only one experimental study (Hermanne *et al.*, 2012) on the cross sections of the ^{45}Sc(d,2n)^{45}Ti reaction was found and their experimental data are scattered. Thus, the present study aims to measure the cross sections of this reaction with higher confidence. We also measured the cross sections of radioactive by-products, ^{44}Ti and ^{44g,44m,46}Sc. The physical yields for the ^{45}Ti production were also deduced from the measured cross sections.

5.2 Materials and methods

The experiment was performed at the AVF cyclotron of RIKEN RI Beam Factory. Stacked-foil activation technique and γ-ray spectrometry were used to measure the cross sections.

The stacked target consisted of metallic foils of ^{45}Sc (25-μm thick, 99.0% purity, Nilaco Corp., Japan and 250-μm thick, 99.9% purity, Johnson Matthey Alfa Products company, USA), ^{27}Al (18-μm thick, 99.6% purity, Nilaco Corp., Japan) and ^{nat}Ti (20-μm thick, 99.6% purity, Nilaco Corp., Japan). The Ti foils are used for monitoring the beam parameters. The Al foils were placed between the Sc foils to sandwich them and to separate the recoiled reaction products from each of the Sc and Ti foils. According to the procedures defined in Section 3.1.1, the average thicknesses of the foils were derived.

The derived thicknesses were 25.8 and 250 μm for ^{45}Sc, 18.5 μm and 20.2 μm for ^{27}Al and ^{nat}Ti, respectively. The foils were cut into the size of 8×8 mm to fit into the target holder, which served as a Faraday cup. The two thicker Sc foils were placed at the top of the stack for cross section measurements of the long-lived ^{44}Ti ($T_{1/2}$ = 59.1 y). The configuration of the stacked foils is shown Fig. 5.1.

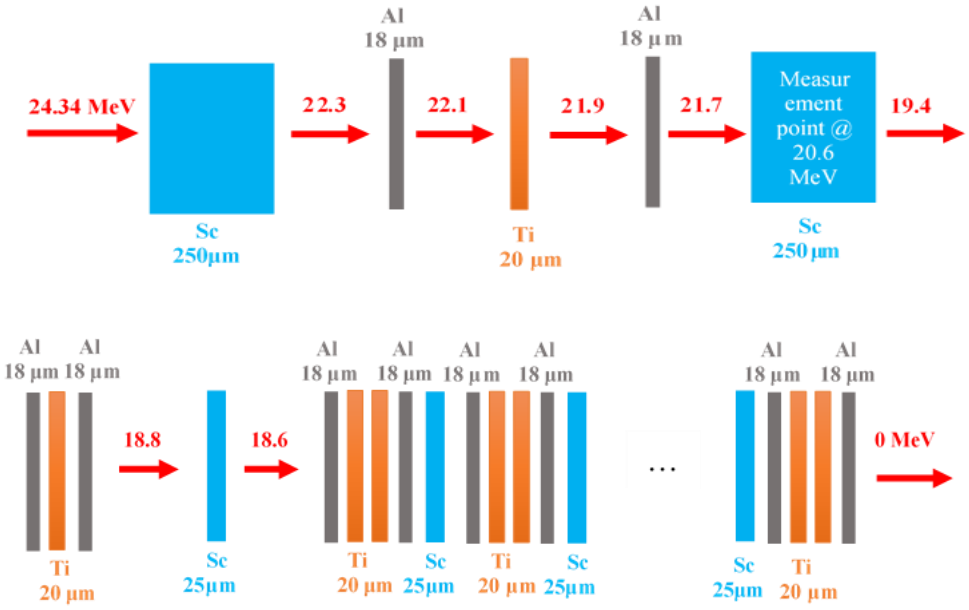

Fig. 5.1. Scheme of the stacked foils. Al foils are used as the catcher and Ti foils are worked as the monitor. Two thicker foils are designated for ^{44}Ti measurement

The stacked target was irradiated for 30 min with a deuteron beam of 24.3 ± 0.1 MeV energy, determined by the time-of-flight method (Watanabe et al., 2014). The average intensity of 180 nA was determined by the collected charge measurement with the Faraday cup-like target holder. The energy degradation in the stacked target was calculated using the SRIM code (Ziegler, Ziegler and Biersack, 2010) and Equation 3.7.

The γ-ray spectra of each irradiated foil were measured by a high-resolution HPGe detector without chemical separation. The detector was calibrated by a mixed γ-ray point source containing ^{57,60}Co, ^{88}Y, ^{109}Cd, ^{113}Sn, ^{137}Cs, ^{139}Ce, and ^{241}Am. Several series of γ-ray measurements were performed to follow the decay of the produced isotopes. The first series of the measurements for short-lived isotopes started after a cooling time of about 1 hour. Each foil was measured more than three times in 5 months. The distance between the detector and the foils was arranged to keep the dead time less than 7%, but each series was always measured with the same detector-sample distance.

The measured γ-ray spectra were analyzed by the Gamma Studio software (SEIKO EG&G). The nuclear reaction and decay data for the γ-ray spectrometry are listed in Table 5.1.

Table 5.1: Reactions and decay data for the investigated reaction products (Pritychenko and Sonzongni, 2003; International Atomic Energy Agency, 2009; National Nuclear Data Center, 2019). γ-lines in bold were used in our data evaluation.

Nuclide	$T_{1/2}$	Decay mode [%]	E_γ [keV]	I_γ [%]	Contributing reaction	Q-value [MeV]	Reference
^{45}Ti	3.08 h	ε+β$^+$ (100)	719.6	0.154(12)	^{45}Sc(d,2n)	-5.07	Burrows, 2008
^{44}Ti	59.1 y	ε (100)	67.8679 78.3234	93.0(2) 96.4(17)	^{45}Sc(d,3n)	-14.6	Chen et al., 2011
^{46}Sc	83.79 d	β$^-$ (100)	889.277 1120.545	99.984(1) 99.987(1)	^{45}Sc(d,p)	6.5	Wu, 2000
^{44m}Sc	58.61 h	ε (1.2) IT (98.8)	271.241 1157.002	86.7(3) 1.20(7)	^{45}Sc(d,t) ^{45}Sc(d,dn) ^{45}Sc(d,p2n) ^{44}Ti decay	-5.07 -11.38 -13.55	Chen et al., 2011
^{44g}Sc	3.97 h	ε+β$^+$ (100)	1157.02	99.9(4)	^{45}Sc(d,t) ^{45}Sc(d,dn) ^{45}Sc(d,p2n) ^{44m}Sc decay	-5.07 -11.38 -13.55	Chen et al., 2011
Monitor reaction							
^{48}V	15.97 d	ε+β$^+$ (100)	944.13 983.52 1312.11	7.870(7) 99.98(4) 98.20(3)	^{46}Ti(d,γ) ^{47}Ti(d,n) ^{48}Ti(d,2n) ^{49}Ti(d,3n)	13.5 4.6 -7.0 -15.2	Burrows, 2006

The cross sections of the ^{nat}Ti(d,x)^{48}V monitor reaction were used to check the primary beam parameters and target thicknesses. The measurements of the 1312.11-keV γ-rays (I_γ = 98.20%) emitted with the decay of ^{48}V ($T_{1/2}$ = 15.97 d) were performed after a cooling time of 1 month in order to avoid the possible interference from decay of ^{48}Sc ($T_{1/2}$ = 43.67 h). The cross sections derived from the measurements for the ^{nat}Ti(d,x)^{48}V reaction were compared with the IAEA recommended values (Takács *et al.*, 2007; Hermanne *et al.*, 2018) in Fig. 5.2. Among the two sets of the recommended values, that in 2007 was used since its shape is consistent with the measured one. The beam intensity determined by the Faraday cup was decreased by 2.0% to have the best agreement. The corrected beam intensity (177 nA) was adopted in the data assessment for the cross sections. The measured thicknesses and incident beam energy were used without any correction.

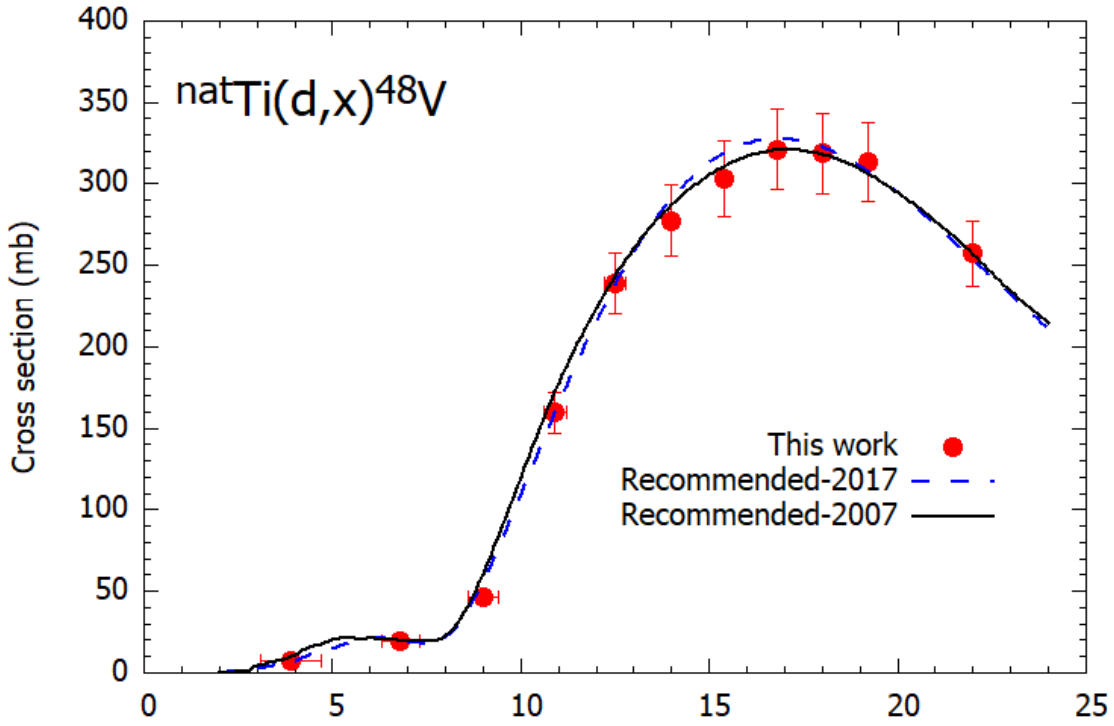

Fig. 5.2. The excitation function of the ^{nat}Ti(d,x)^{48}V monitor reaction compared with the recommended values (Takács *et al.*, 2007; Hermanne *et al.*, 2018).

The uncertainties of the cross sections and the beam intensity were estimated using Equations 3.22 and 3.23. The projectile energy uncertainty of ± 0.1 MeV is propagated to ± 0.6 MeV in the last foil of the stack, which was estimated from uncertainties of the incident energy and target thicknesses (<2%). The energy degradation of 2.0-2.2 and 0.2-0.6 MeV in thick and thin foils were obtained using the SRIM code. The midpoint projectile energy, energy thickness of each foil and the uncertainties were listed in Table 5.2. The total uncertainty of the cross sections was 8.1-28.7%. It was estimated using the following components: beam intensity (5%), target thickness, target purity (1%), detector efficiency (6%), γ-intensity (<8%), and γ-ray counting (0.4-26.4%). The statistical uncertainty for ^{45}Ti was high due to the small peak for the very low-intensity γ-line (719.6 keV, 0.154%).

5.3 Results and Discussions

The activation cross sections of ^{44,45}Ti and ^{44g,44m,46}Sc were determined for the deuteron-induced reactions on ^{45}Sc. The results are given in Table 5.2 and graphically shown in Figs. 5.3-5.7, in comparison with the previous experimental data (Skobelev *et al.*, 2011; Hermanne *et al.*, 2012) and the theoretical estimation of TENDL-2019 (Koning *et al.*, 2019). Our results in the figures show the cross sections in terms of the projectile energy with its total uncertainty but without the energy thickness. Physical yield for the radionuclide ^{45}Ti was derived from the measured cross sections and is shown in Fig. 5.8.

Table 5.2: Measured cross sections of ^{44,45}Ti and ^{44m,44g,46}Sc in the deuteron-induced reactions on ^{45}Sc. The midpoint projectile energy, energy thickness of each foil and the uncertainties propagated from those of the incident energy and target thicknesses are shown in the first column.

Energy (MeV)	Cross sections (mb)				
	^{45}Sc(d,2n)^{45}Ti	^{45}Sc(d,3n)^{44}Ti	^{45}Sc(d,p)^{46}Sc	^{45}Sc(d,x)^{44m}Sc	^{45}Sc(d,x)^{44g}Sc
23.3 ±1.0 ± 0.1	237 ± 64	7.44 ±0.71	81.6 ± 6.9	107 ± 9	113 ± 13
20.6 ±1.1 ± 0.1	251 ± 46	3.36 ±0.35	104 ± 9	40.7 ± 3.3	49.7 ± 5.7
18.7 ±0.1 ± 0.2	272 ± 40		102 ± 8	12.3 ± 0.9	17.6 ± 2.1
17.5 ±0.1 ± 0.2	279 ± 43		109 ± 9	5.55 ± 0.46	9.74 ± 1.2
16.3 ±0.1 ± 0.2	297 ± 41		127 ± 10	3.16 ± 0.26	6.57 ± 1.03
14.9 ±0.1 ± 0.2	296 ± 38		143 ± 12	2.11 ± 0.17	4.44 ± 0.85
13.5 ±0.2 ± 0.3	291 ± 36		163 ± 13	1.68 ± 0.14	3.14 ± 0.66
11.9 ±0.2 ± 0.3	261 ± 32		199 ± 16	1.20 ± 0.10	1.96 ± 0.16
10.2 ±0.2 ± 0.3	201 ± 24		253 ± 21	0.539 ± 0.045	0.892 ± 0.075
8.2 ±0.2 ± 0.4	96.5 ± 12.1		316 ± 26	0.104 ± 0.012	0.194 ± 0.018
5.8 ±0.3 ± 0.6	3.14 ± 0.54		311 ± 25	0.074 ± 0.009	0.130 ± 0.011

5.3.1 The ^{45}Sc(d,2n)^{45}Ti reaction

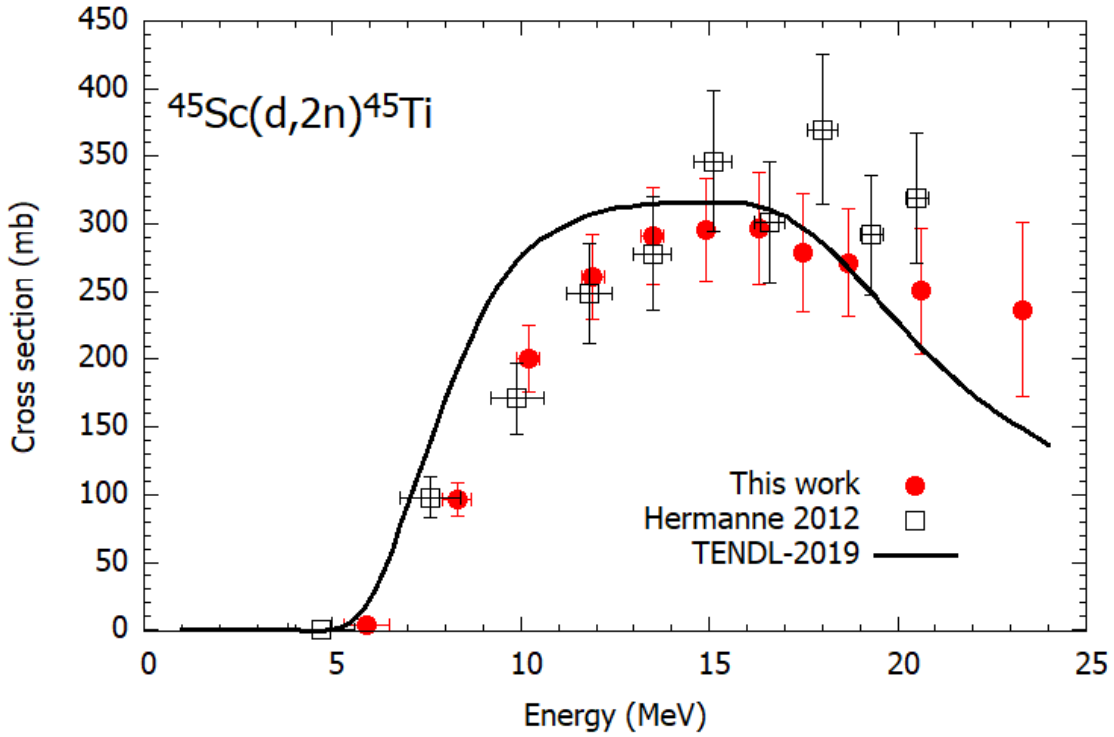

Fig. 5.3. The excitation function of the ^{45}Sc(d,2n)^{45}Ti reaction.

^{45}Ti ($T_{1/2}$ = 3.08 h) can be produced in the (d,2n) reaction on ^{45}Sc. After a cooling time of about 1 hour, the cross sections of the reaction were derived from the measurements of the low intensity 719.6-keV γ-rays (I_γ = 0.154%) emitted in the decay of ^{45}Ti. The excitation function is shown in Fig. 5.3 in comparison with the previous data (Hermanne *et al.*, 2012) and the theoretical estimation of TENDL-2019 (Koning *et al.*, 2019). The present data are consistent with the data reported by Hermanne et al. (2012) and are less scattered. The TENDL-2019 data, however, show the peak position slightly shifted to the lower energy.

5.3.2 The ^{45}Sc(d,3n)^{44}Ti reaction

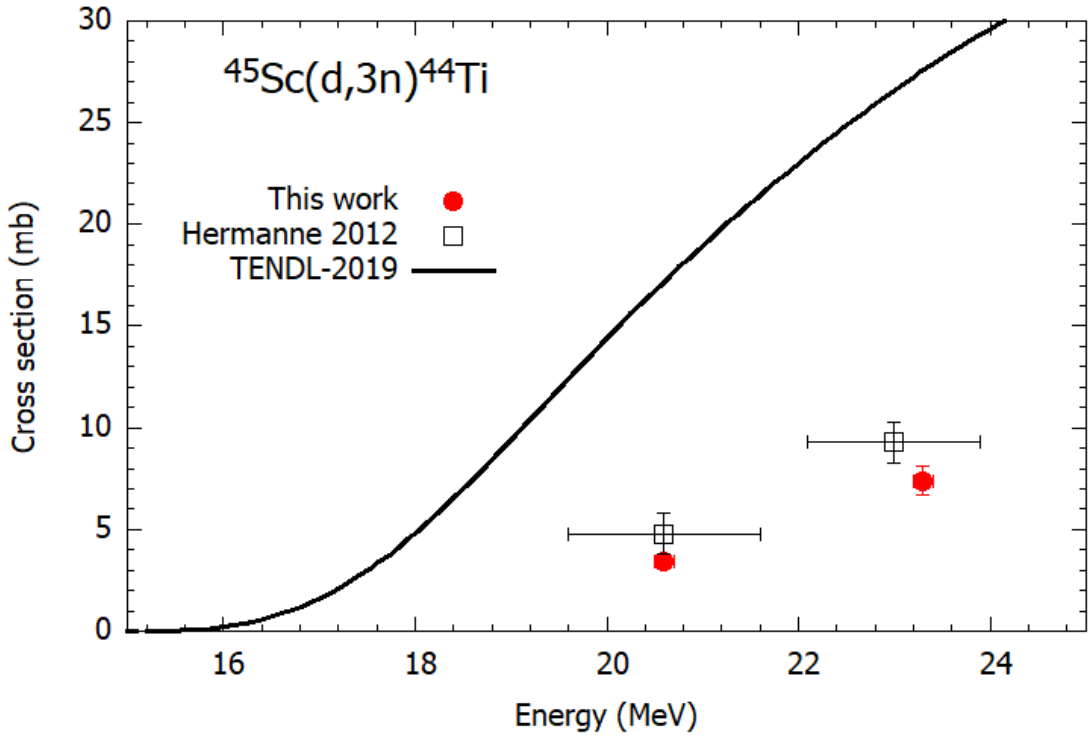

Fig. 5.4. The excitation function of the ^{45}Sc(d,3n)^{44}Ti reaction.

Only the (d,3n) reaction on ^{45}Sc produces the long-lived radioisotope ^{44}Ti ($T_{1/2}$ = 59.1 y). ^{44}Ti decays by EC process (100%) into ^{44g}Sc. The γ-ray measurements were performed for more than 6 hours for the first two thicker Sc foils (250 μm thickness) after a long cooling time of about 5 months. The cross sections of the ^{45}Sc(d,3n)^{44}Ti reaction were derived using the measurements of the 78.32-keV γ-rays (I_γ = 96.4%) emitted in the decay of ^{44}Ti. For this low energy γ-rays, the self-absorption correction (discussed in Section 3.3.1) was considered using the mass attenuation coefficient of 0.40 cm^2/g for the γ-line at 78.32 keV. The self-absorption was estimated to be 1.5%. The internal consistency was checked using the measurements of the 67.87 keV γ-line (I_γ = 93%). The derived cross sections are compared with the previous experimental data (Hermanne *et al.*, 2012) and the theoretical estimation of TENDL-2019 (Koning *et al.*, 2019) in Fig. 5.4. The energy uncertainty of the two data points of Hermanne et al. 2012 is large because these two points correspond to the last two foils of a long stack irradiated with a 50 MeV deuteron beam. Our data agree with the data reported by Hermanne et al. (2012) within the uncertainty. The TENDL-2019 data overestimate two experimental datasets.

5.3.3 The ^{45}Sc(d,p)^{46}Sc reaction

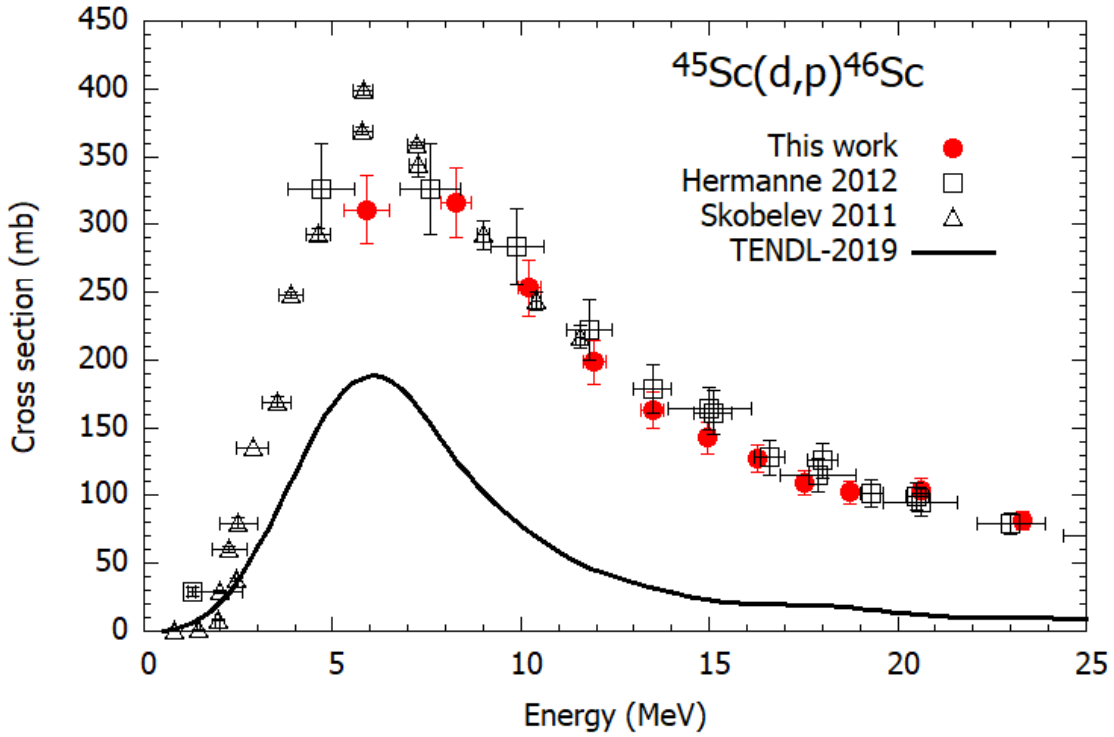

Fig. 5.5. The excitation function of the ^{45}Sc(d,p)^{46}Sc reaction.

The (d,p) reaction on ^{45}Sc can produce both the short-lived meta-stable state ($T_{1/2}$ = 18.75 s) and the long-lived ground state ($T_{1/2}$ = 83.79 d) of ^{46}Sc. During the beam time and cooling period, the meta-stable state decayed by the internal transition (IT) (100 %) into the ground state. The cumulative cross sections of the ^{45}Sc(d,p)^{46}Sc reaction were derived from the measurement of the 1120.545-keV γ-line (I_γ = 99.987%) from the decay of the ground state. The excitation function for the ^{46}Sc production is shown in Fig. 5.5 in comparison with the previous experimental data (Skobelev *et al.*, 2011; Hermanne *et al.*, 2012) and the TENDL-2019 data (Koning *et al.*, 2019). Both experimental data sets are in agreement with the present data. The TENDL-2019 predictions are lower than the experimental data.

5.3.4 The ^{45}Sc(d,x)^{44m}Sc reaction

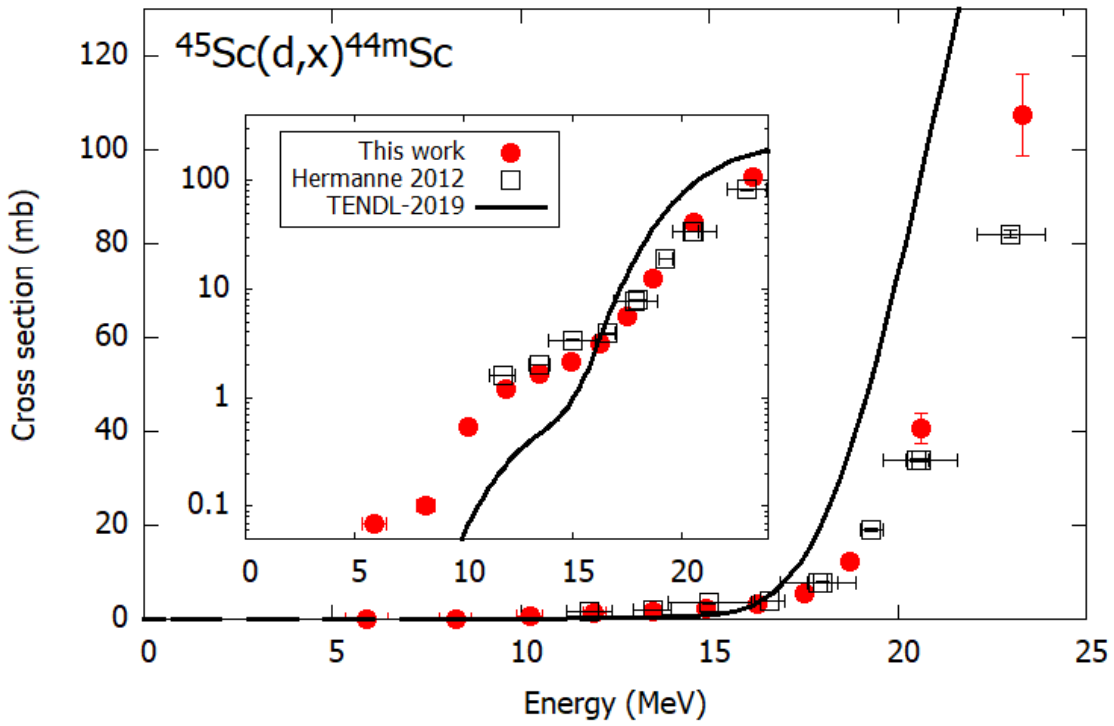

Fig. 5.6. The excitation function of the ^{45}Sc(d,x)^{44m}Sc reaction.

The long-lived meta-stable state of ^{44}Sc ($T_{1/2}$ = 58.61 h) is formed by the (d,t), (d,dn) and (d,p2n) reactions on ^{45}Sc. The meta-stable state ^{44m}Sc decays by the IT process (98.8%) into the ground state ^{44g}Sc and by the EC process (1.2%) into ^{44}Ca. The intense γ-rays at 271.24 keV (I_γ = 86.7%) emitted from the decay of ^{44m}Sc are used to derive the cross sections of the ^{45}Sc(d,x)^{44m}Sc reaction. After an average cooling time of about 28 hours, the γ-ray spectrometry was carried out. The excitation function for the ^{45}Sc(d,x)^{44m}Sc reaction is shown in Fig. 5.6 in comparison with the previous experimental data (Hermanne et al., 2012) and the TENDL-2019 data (Koning *et al.*, 2019). The present dataset is consistent with the data reported by Hermanne et al. (2012). The TENDL-2019 data overestimate the experimental cross sections above 15 MeV.

5.3.5 The ^{45}Sc(d,x)^{44g}Sc reaction

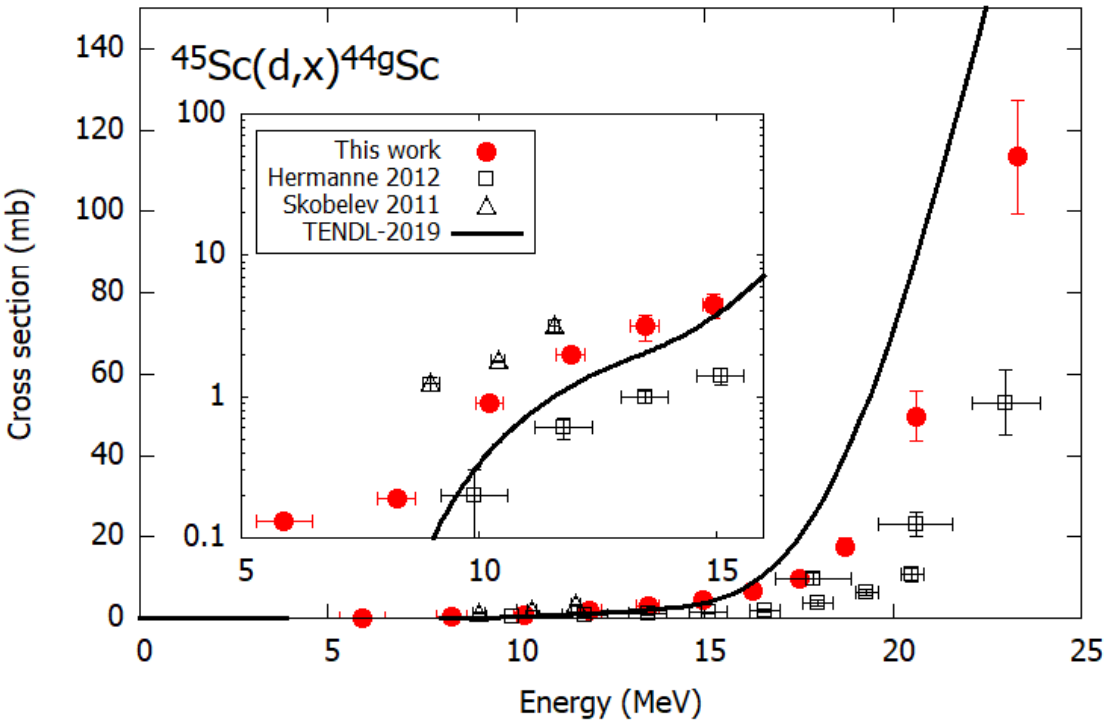

Fig. 5.7. The excitation function of the ^{45}Sc(d,x)^{44g}Sc reaction.

The ground state of ^{44}Sc ($T_{1/2}$ = 3.97 h) can be formed directly in the ^{45}Sc(d,x)^{44g}Sc reactions and indirectly by decay of its co-produced meta-stable state ^{44m}Sc. The contribution of the parent nucleus ^{44}Ti is very small and neglected due to its long half-life. The ground state decays by β^+ and EC processes into ^{44}Ca. In the data assessment, the intense γ-rays at 1157.02 keV (I_γ = 99.9%) were used. The contributions to the collected counts from both decay processes of ^{44m}Sc to ^{44g}Sc (IT: 98.8%) and ^{44}Ca (EC: 1.2%) were subtracted using the cross sections presented in section 5.3.4. The estimated contributions of the IT and EC processes of ^{44m}Sc were less than 35% and 0.5%, respectively. Both contributions were subtracted from the measured counts of the 1157.02-keV photo-peak. The independent cross sections for the ^{45}Sc(d,x)^{44g}Sc reaction were derived using the corrected counts. The derived excitation function is shown in Fig. 5.7 in comparison with the previous experimental data (Hermanne et al., 2012; Skobelev et al., 2011) and the TENDL-2019 prediction (Koning *et al.*, 2019). Our data are between the experimental data reported by Hermanne et al. (2012) and Skobelev et al. (2011). The TENDL-2019 data are in a partial agreement with our data.

5.3.6 Physical Yield

The physical yield (discussed in Section 2.2.3) of ^{45}Ti was deduced from the spline fitted curve of the measured excitation function presented in section 5.3.1. The result is shown in Fig. 5.7 with the one previous experimental data point at 22 MeV (Dmitriev, Krasnov and Molin, 1983). Our deduced physical yield is slightly larger than the experimental data.

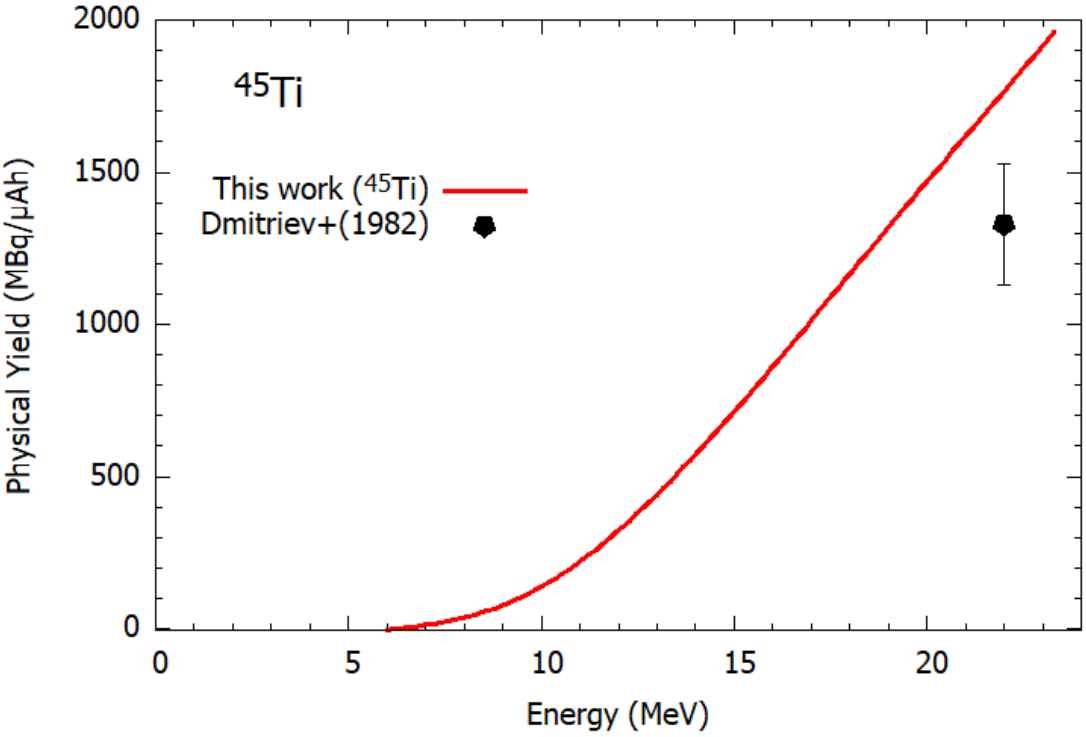

Fig. 5.8. The physical yield of ^{45}Ti via the deuteron-induced reaction on ^{45}Sc.

No other radioactive impurities of Ti are produced below the threshold energy of the ^{45}Sc(d,3n)^{44}Ti reaction. Therefore, production of ^{45}Ti without radio-contamination is possible in the ^{45}Sc(d,2n)^{45}Ti reaction in the deuteron energy range up to 15 MeV.

The stable isotope ^{46}Ti can also be formed directly and indirectly through the decay of co-produced ^{46}Sc and affect the specific activity of ^{45}Ti. The ratio of produced numbers of ^{45}Ti to all considered titanium (^{45}Ti+^{46}Ti+^{47}Ti) was estimated using our cross section data for ^{45}Ti and ^{46}Sc and the TENDL-2019 data for ^{46}Ti and ^{47}Ti. This ratio has a maximum in the energy region from 15 to 8 MeV and is about 0.74 at the end-of-bombardment (EOB) for a 1 h irradiation. The EOB activity reaches 680 MBq for 1h and

1μA irradiation. The applied energy window can be optimized for the higher ratio or activity.

5.4 Summary

The production cross sections of the ^{45}Sc(d,2n)^{45}Ti reaction was measured up to 24 MeV. The stacked-foil activation technique and the high-resolution γ-ray spectrometry were used for the cross section measurements. The obtained data were compared with the previous experimental data and the TENDL-2019 prediction. The derived excitation function of the ^{45}Sc(d,2n)^{45}Ti reaction is consistent with the earlier published data of Hermanne et al. (2012). The deduced physical yield is slightly larger than the experimental data of Dmitriev et al. (1983). The radioactive-contamination-free ^{45}Ti can be obtained via the ^{45}Sc(d,2n)^{45}Ti reaction in the energy region of 15 - 8 MeV applying chemical separation.

CHAPTER 6: Conclusion

We investigated deuteron-induced reactions on natural zinc and scandium to produce medical isotopes ^{68}Ga and ^{45}Ti using cyclotrons. In two experiments, the production cross sections of ^{68}Ga and ^{45}Ti were measured up to 24 MeV using the stacked-foil activation technique and the high-resolution γ-ray spectrometry. The measured excitation functions were compared with previous experimental data. The physical yields for the medical isotopes were deduced from measured cross sections and compared with previous experimental data.

The measured excitation functions are consistent with recent experimental data. Possible radioactive impurities for the production routes were estimated. The suitable projectile energy regions were determined for optimizing the production routes. The deduced yields indicate to reach a sufficient dose for PET scans. The yield from the ^{68}Zn(d,2n)^{68}Ga reaction is comparable with that from the ^{68}Zn(p,n)^{68}Ga reaction. The radioactive-contamination-free ^{45}Ti can be obtained via the ^{45}Sc(d,2n)^{45}Ti reaction in the energy region of 15 - 8 MeV applying chemical separation.

In conclusion, the deuteron-induced reactions on natural zinc and natural scandium can be considered as alternative routes for cyclotron production of medical isotopes ^{68}Ga and ^{45}Ti. The data measured in these experiments can extend the nuclear reaction database for optimizing production routes of medical isotopes.

In the future, production cross sections of new medicinal isotopes in cyclotrons and their route optimization will be studied continuously. Furthermore, we will focus on the development of radioactive nanoparticles as a contrast agent in multimodal imaging techniques such as PET/MRI and SPECT/MRI. We will consider a feasibility of applications in vitro and in vivo of the created radioactive nanoparticles.

Appendix A

The detailed information of an HPGe detector and a multiple γ-ray point source that used in our experiments are given as follows:

Detectors:

An HPGe detector (ORTEC GMX30P4-70) with the relative efficiency of 30% to a (3x3) NaI detector, and the energy resolution of 1.9 keV for the 1.332 MeV γ-line of the ^{60}Co standard source, a peak to Compton ratio of 52:l, the peak shape, FWTM/FWHM of 1.9 and with Be window of 0.51 thickness. γ-ray spectrometer and HPGe detector employed in these experiments are shown in Fig. A.1.

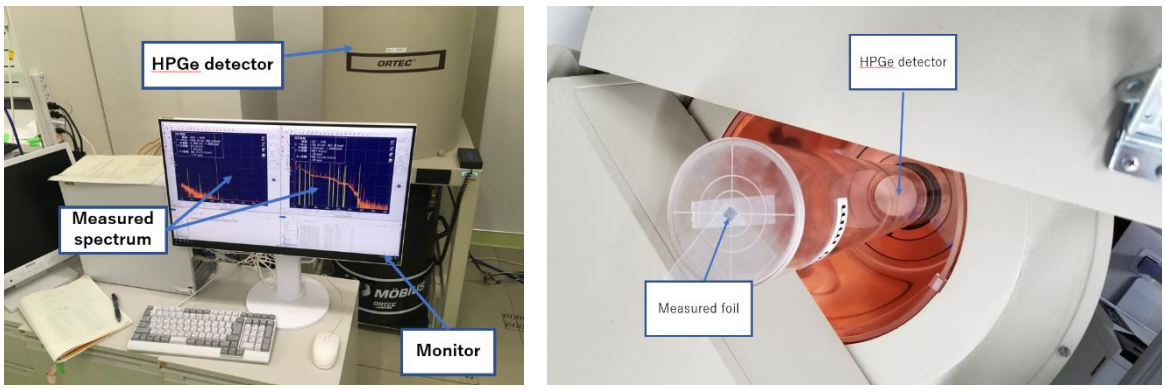

Fig. A.1. γ-ray spectrometer and ORTEC HPGe detector at RIKEN.

Dead time of detector

If two or more γ-rays emitted from the activated sample simultaneously enter into the detector crystal, the detector cannot process the signals. Then, the signal conversion process of the detection system waited for a certain time (up to microseconds). It is called the dead time and its correction can be estimated as:

$$\varepsilon_t = \frac{t_m - t_{\text{dead time}}}{t_m} = \frac{t_{\text{live time}}}{t_{\text{real time}}} \tag{A.1}$$

In our experiments, the dead time was kept below 10%.

Efficiency of detector

After irradiation, characteristic γ-rays emitted from activated foils are measured using a high purity Germanium (HPGe) detector. Each γ-ray of a certain energy E_γ emitted from the foils is detected with a certain probability due to attenuation, Compton scattering and etc. The probability is called the detector efficiency, ε_d. It can be determined from the measurement of a calibration source with known activity. In this work, a multiple γ-ray point source containing ^{57,60}Co, ^{88}Y, ^{109}Cd, ^{113}Sn ^{137}Cs, ^{139}Ce, and ^{241}Am is used to determine the detector efficiency.

The calibration source emits several γ-rays and forms photo peaks in the spectrum obtained at a fixed geometry (a distance between detector and source). As a result, the efficiency curve (as a function of γ-ray energy) is obtained from the measurement and shown in Fig. A.2.

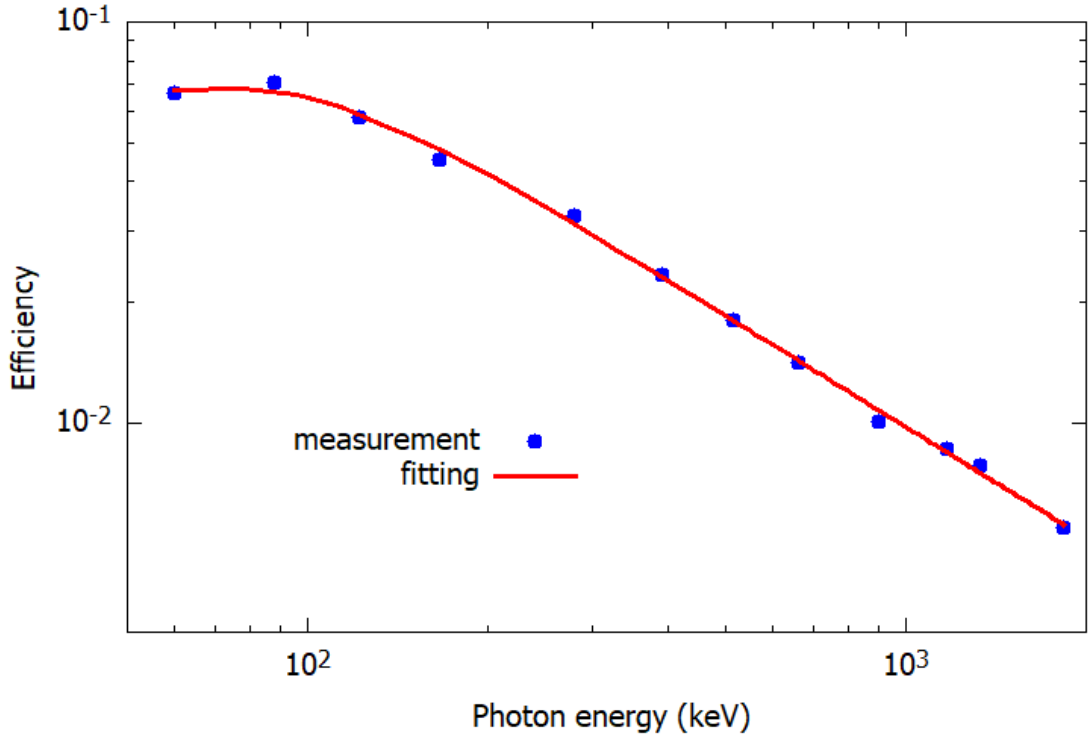

Fig. A.2.An example of efficiency calibration for an HPGe detector at 3 cm using a multiple γ-ray point source containing ^{57,60}Co, ^{88}Y, ^{109}Cd, ^{113}Sn ^{137}Cs, ^{139}Ce, and ^{241}Am.

The detection efficiency is fitted using a polynomial function as

$$\ln \varepsilon_d = \sum_{i=0}^{5} a_i \ln E_i \qquad \text{(A.2)}$$

where a_i is the fitting parameters and E_i is the energy of the photo peak.

The gamma-ray intensity

The gamma-ray intensity is a fraction of a specific γ-ray intensity in a decay:

$$\varepsilon_{\gamma_1} = \frac{I_{\gamma_1}}{\sum_i I_{\gamma_i}} \qquad \text{(A.3)}$$

The data of the γ-ray intensity were taken from NuDat 2.7 (National Nuclear Data Center, 2017), LiveChart (International Atomic Energy Agency, 2009).

Calibration Source

The detector was calibrated by a multiple γ-ray point source containing the radioisotopes listed in Table A.1. The calibration source was bought from Eckert & Ziegler and certified with an uncertainty of 2.3-3.2%.

Table A.1: Characteristics of the calibration point source.

Gamma-Ray Energy (keV)	Nuclide	Half-life	Branching Ratio (%)
60	Am-241	(432.17±0.66) years	36.0
88	Cd-109	(462.6±0.7) days	3.63
122	Co-57	(271.79±0.09) days	85.6
166	Ce-139	(137.640±0.023) days	79.9
279	Hg-203	(46.595±0.013) days	81.5
392	Sn-113	(115.09±0.04) days	64.9
514	Sr-85	(64.849±0.004) days	98.4
662	Cs-137	(30.17±0.16) years	85.1
898	Y-88	(106.630±0.025) days	94.0
1173	Co-60	(5.272±0.001) years	99.86
1333	Co-60	(5.272±0.001) years	99.98
1836	Y-88	(106.630±0.025) days	99.4

Acknowledgement

I would like to express my highest gratitude for the M-JEED scholarship (Mongolian-Japan Engineering Education Development Program, J11B16). Thanks to the scholarship, I could have an educational and research opportunity in the doctoral course in the Graduate School of Biomedical Science and Engineering, Hokkaido University.

My research has been conducted under supervision and assistance of many people. I sincerely appreciate everything they have given to me:

My heartfelt thanks and greatest pleasures are given to my supervisor, Prof. Masayuki Aikawa, for his support on my research. Also, I would like to thank my colleagues in the laboratory of Medical Applied Basic Physics, Graduate School of Biomedical Science and Engineering Group, Hokkaido University for their wonderful collaboration.

I deeply appreciate help and collaboration of Dr. Ichinkhorloo Davgadorj. Her assistance in resolving a variety of problems, her patience and friendly guidance over many years, and great respect for her family are particularly appreciated.

I would like to express my sincere gratitude to Prof. Javkhlantugs Namsrai, Prof. Erdene Norov and Prof. Tegshjargal Khishigjargal at National University of Mongolia. Their leadership, broad perspective, faith and positive thinking always supports me amid scientific difficulties.

The members in RI Application Research Group, RIKEN Nishina Center for Accelerator Based Science, collaboratively carried out experiments. I want to express my gratitude to the leader of the group, Dr. Hiromitsu Haba, for his kind support, encouragement, and providing excellent experimental conditions. In addition, the other members of the group, particularly Dr. Yukiko Komori, are appreciated for their support in preparing samples, irradiations for all the experiments in this thesis.

I would like to thank Sándor Takács, Ferenc Ditrói, and Zoltán Szűcs, Institute for Nuclear Research (ATOMKI), Debrecen, Hungary. Their outstanding teamwork, open-minded discussions, finding better solutions, and generous support are deeply appreciated.

I would want to express my gratitute to Prof. Chuukhenkhuu Gonchigdorj, my former supervisor, for his guidance and long-term support, as well as colleagues at Nuclear Research Center, National University of Mongolian.

My parents-in-law Tsoodol Buya and Dulamjav Zagdaa, owes me the greatest debt for her unwavering love and support throughout my life. I would also like to express my gratitude to my family, especially my lovely daughter Tegshzaya Zolbadral for always putting a smile on my face and bringing joy to my heart. In addition, I thank all of my brothers and sisters, and their families for their unwavering support and inspiration.

I would like to thank the people to give me the research opportunities. All experiments were carried out at RI Beam Factory operated by RIKEN Nishina Center and CNS, University of Tokyo, Japan. These works were supported by “Optimization of accelerator production routes of the new theranostic radioisotopes Sc-47 and Cu-67” under the Japan - Hungary Research Cooperative Program between JSPS and HAS and also supported by JSPS KAKENHI Grant Number 17K07004.

Finally, I thank Dr. Skobelev for his kind response to the inquiry on his study considered in our second experiment.

Cited References:

Alharbi, A. A. *et al.* (2011) 'Medical Radioisotopes Production: A Comprehensive Cross-Section Study for the Production of Mo and Tc Radioisotopes Via Proton Induced Nuclear Reactions on natMo', *Radioisotopes - Applications in Bio-Medical Science*, pp. 3–27. doi: 10.5772/20598.

Banerjee, S. R. and Pomper, M. G. (2013) 'Clinical applications of Gallium-68', *Applied Radiation and Isotopes*. Elsevier, 76, pp. 2–13. doi: 10.1016/j.apradiso.2013.01.039.

Baron, N. and Cohen, B. L. (1963) 'Activation Cross-Section Survey of Deuteron-Induced Reactions*', 1721(September 1954), pp. 2636–2642.

Basdevant, J. L., Rich, J. and Spiro, M. (2005) *Fundamentals in nuclear physics: From nuclear structure to cosmology*, *Fundamentals In Nuclear Physics: From Nuclear Structure to Cosmology*. Springer New York. doi: 10.1007/b106774.

Bissem, H. H. *et al.* (1980) 'Entrance and exit channel phenomena in d- and He3-induced preequilibrium decay', *Physical Review C*, 22(4), pp. 1468–1484. doi: 10.1103/PhysRevC.22.1468.

Bonardi, M. L. *et al.* (2003) 'Thin-target excitation functions and optimization of simultaneous production of NCA copper-64 and gallium-66,67 by deuteron induced nuclear reactions on a natural zinc target', *Journal of Radioanalytical and Nuclear Chemistry*, 257(1), pp. 229–241. doi: 10.1023/A:1024703022762.

Boros, E. and Packard, A. B. (2019) 'Radioactive Transition Metals for Imaging and Therapy', *Chemical Reviews*, 119(2), pp. 870–901. doi: 10.1021/acs.chemrev.8b00281.

Carlson, S. (1995) 'A glance at the history of nuclear medicine', *Acta Oncologica*, 34(8), pp. 1095–1102. doi: 10.3109/02841869509127236.

Carver, J. H. and Jones, G. A. (1959) 'Radiative deuteron capture $Zn^{64}(d,\gamma)Ga^{66}$', *Nuclear Physics*, 11, pp. 400–410. doi: 10.1016/0029-5582(59)90278-0.

Coetzee, P. P. and Peisach, M. (1972) 'Activation Cross Sections for Deuteron-Induced Reactions on some Elements of the First Transition Series, up to 5.5 MeV', *Radiochimica*

Acta, 17(1), pp. 1–6. doi: 10.1524/ract.1972.17.1.1.

Daraban, L. *et al.* (2008) 'Experimental study of excitation functions for the deuteron induced reactions 64Zn(d,2p)64Cu and 64Zn(d,αn)61Cu using the stacked-foil technique', *Applied Radiation and Isotopes*, 66(2), pp. 261–264. doi: 10.1016/j.apradiso.2007.09.006.

Dmitriev, P. P. *et al.* (1991) '^{66,67}Ga yields in the reactions $^{66\text{-}68}$Zn(d,xn).', *Sov. Atom. Energy 71*, 776–777((translated from Atomnaya Energiya 71 (1991) 261)).

Dmitriev, P. P., Krasnov, N. N. and Molin, G. A. (1983) *Yields of radioactive nuclides formed by bombardment of a thick target with 22-MeV deuterons*. International Atomic Energy Agency (IAEA): (INDC(CCP)--210/L). Available at: http://inis.iaea.org/search/search.aspx?orig_q=RN:15043227.

Fateh, B., H. Afarideh and Haji-Saeid, S. M. (1996) 'Proceedings of the 14th International Conference "Cyclotrons and Their Applications", 8–13 October 1995, Cape Town, South Africa, Word Scientific, Singapore', in, p. 553.

Gill, M., Livens, F. and Peakman, A. (2014) 'Chapter 9 - Nuclear Fission', in Letcher, T. M. B. T.-F. E. (Second E. (ed.). Boston: Elsevier, pp. 181–198. doi: https://doi.org/10.1016/B978-0-08-099424-6.00009-0.

Gilly, L. J. *et al.* (1963) 'Absolute cross sections and excitation functions for (d,p) and (d,2n) reactions on Mn^{55}, Cu^{63}, Cu^{65}, Zn^{66}, and Zn^{68} between 3 and 11.6 MeV', *Physical Review*, 131(4), pp. 1727–1731. doi: 10.1103/PhysRev.131.1727.

Hermanne, A. *et al.* (2012) 'Cross sections of deuteron induced reactions on ^{45}Sc up to 50 MeV: Experiments and comparison with theoretical codes', *Nuclear Instruments and Methods in Physics Research, Section B: Beam Interactions with Materials and Atoms*. Elsevier B.V., 270(1), pp. 106–115. doi: 10.1016/j.nimb.2011.09.002.

Hermanne, A. *et al.* (2018) 'Reference Cross Sections for Charged-particle Monitor Reactions', *Nuclear Data Sheets*, 148, pp. 338–382. doi: 10.1016/j.nds.2018.02.009.

Hevesy, G. de (1943) *The Nobel Prize in Chemistry 1943, NobelPrize.org 2020., Nobel Media AB 2020. Sun. 25 Oct.* Available at:

https://www.nobelprize.org/prizes/chemistry/1943/summary/.

Hubbel, J. H. and Seltzer, S. M. (2004) *X-Ray Mass Attenuation Coefficients: NIST Standard Reference Database 126*. doi: 10.18434/T4D01F.

International Atomic Energy Agency (2009) *LiveChart of Nuclides.* Available at: https://www-nds.iaea.org/livechart/.

International Atomic Energy Agency (2019) 'Gallium-68 Cyclotron Production', *IAEA-TECDOC-1863, IAEA, Vienna*.

Jaszczak, R. J. (2006) 'The early years of single photon emission computed tomography (SPECT): an anthology of selected reminiscences', *Physics in Medicine and Biology*, 51(13), pp. R99–R115. doi: 10.1088/0031-9155/51/13/R07.

Khandaker, M. U. *et al.* (2015) 'Production cross-sections of long-lived radionuclides in deuteron-induced reactions on natural zinc up to 23 MeV', *Nuclear Inst. and Methods in Physics Research, B*. Elsevier B.V., 346, pp. 8–16. doi: 10.1016/j.nimb.2015.01.011.

Kim, K. T. *et al.* (2019) 'General review of titanium toxicity', *International Journal of Implant Dentistry*. Springer Science and Business Media LLC, 5(1), p. 10. doi: 10.1186/s40729-019-0162-x.

Koning, A. J. *et al.* (2019) 'TENDL: Complete Nuclear Data Library for Innovative Nuclear Science and Technology', *Nuclear Data Sheets*. Elsevier Inc., 155, pp. 1–55. doi: 10.1016/j.nds.2019.01.002.

Koning, A. J. and Rochman, D. (2012) 'Modern Nuclear Data Evaluation with the TALYS Code System', *Nuclear Data Sheets*, 113(12), pp. 2841–2934. doi: 10.1016/j.nds.2012.11.002.

Konstantinov, I. O. (1997) 'The thin layer activation method and its applications in industry', *IAEA-TECDOC-924, IAEA*, p. 43.

Krasnov, N. N. *et al.* (1972) 'Yield of Ga-67 produced by a cyclotron.', *Izotopy v SSSR*, 11.

Lin, M., Waligorski, G. J. and Lepera, C. G. (2018) 'Production of curie quantities of

^{68}Ga with a medical cyclotron via the ^{68}Zn(p,n)^{68}Ga reaction', *Applied Radiation and Isotopes*. Elsevier Ltd, 133(December 2017), pp. 1–3. doi: 10.1016/j.apradiso.2017.12.010.

Ma, L. *et al.* (2007) 'Energy loss and straggling of MeV ions through biological samples', *Journal of Applied Physics*, 102(8), pp. 1–6. doi: 10.1063/1.2800996.

Morrison, D. L. and Porile, N. T. (1959) 'Absence of Isomerism in Gallium-65', *Physical Review*, 113(1), pp. 289–290. doi: 10.1103/PhysRev.113.289.

Nassiff, S. J. and Münzel, H. (1972) 'Excitation functions for deuteron induced reactions on zinc', *Radiochemical and radioanalytical letters*, 12, pp. 353–361.

Nassiff, S. J. and Münzel, H. (1973) 'Cross sections for the reactions ^{66}Zn(d,n)^{67}Ga, ^{52}Cr(d,2n)^{52g}Mn and ^{186}W(d,2n)^{186}Re.', *Radiochim. Acta*, 19, pp. 97–99.

National Nuclear Data Center (2017) *Nuclear structure and decay data on-line library, Nudat 2.7*. Available at: http://www.nndc.bnl.gov/nudat2/.

National Nuclear Data Center (2019) *Nuclear structure and decay data on-line library, Nudat 2.8*. Available at: http://www.nndc.bnl.gov/nudat2/.

Omami, G., Tamimi, D. and Branstetter, B. F. (2014) 'Basic principles and applications of 18F-FDG-PET/CT in oral and maxillofacial imaging: A pictorial essay', *Imaging Sci Dent*. Korean Academy of Oral and Maxillofacial Radiology, 44(4), pp. 325–332. Available at: https://doi.org/10.5624/isd.2014.44.4.325.

Otuka, N. *et al.* (2014) 'Towards a More complete and accurate experimental nuclear reaction data library (EXFOR): International collaboration between nuclear reaction data centres (NRDC)', *Nuclear Data Sheets*. Academic Press Inc., 120, pp. 272–276. doi: 10.1016/j.nds.2014.07.065.

Otuka, N. and Takács, S. (2015) 'Definitions of radioisotope thick target yields', *Radiochimica Acta*, 103(1), pp. 1–6. doi: 10.1515/ract-2013-2234.

Portnow, L. H., Vaillancourt, D. E. and Okun, M. S. (2013) 'The history of cerebral PET scanning: from physiology to cutting-edge technology', *Neurology*. Lippincott Williams

& Wilkins, 80(10), pp. 952–956. doi: 10.1212/WNL.0b013e318285c135.

Pritychenko, B. and Sonzongni, A. (2003) *Q-value Calculator (QCalc).* Available at: https://www.nndc.bnl.gov/qcalc/.

Qaim, S. M. *et al.* (2001) *IAEA-TECDOC-1211, Beam monitor reactions, Charged Particle Cross-Section Database for Medical Radioisotope Production: Diagnostic Radioisotopes and Monitor Reactions, Co-ordinated Research Project (1995–1999).* Vienna: IAEA.

Qaim, S. M. *et al.* (2016) 'Uses of alpha particles, especially in nuclear reaction studies and medical radionuclide production', *Radiochimica Acta*, 104(9), pp. 601–624. doi: 10.1515/ract-2015-2566.

Qaim, S. M. (2017) 'Nuclear data for production and medical application of radionuclides: Present status and future needs', *Nuclear Medicine and Biology*. Elsevier Inc., 44, pp. 31–49. doi: 10.1016/j.nucmedbio.2016.08.016.

Ramirez, J. J. *et al.* (1969) 'Energy straggling of alpha particles through gases', *Physical Review*, 179(2), pp. 310–314. doi: 10.1103/PhysRev.179.310.

Riga, S. *et al.* (2018) 'Production of Ga-68 with a General Electric PETtrace cyclotron by liquid target', *Physica Medica*. Elsevier, 55(July), pp. 116–126. doi: 10.1016/j.ejmp.2018.10.018.

Šimečková, E. *et al.* (2017) 'Proton and deuteron activation measurements at the NPI and future plans in SPIRAL2/NFS', *EPJ Web of Conferences*. EDP Sciences, 146, p. 11034. doi: 10.1051/epjconf/201714611034.

Skobelev, N. K. *et al.* (2011) 'Excitation functions for the radionuclide 46Sc produced in the irradiation of 45Sc with deuterons and 6He', *Journal of Physics G: Nuclear and Particle Physics*, 38(3), p. 35106. doi: 10.1088/0954-3899/38/3/035106.

Song, B. *et al.* (2015) 'A review on potential neurotoxicity of titanium dioxide nanoparticles', *Nanoscale Research Letters*. Nanoscale Research Letters, 10(1), p. 342. doi: 10.1186/s11671-015-1042-9.

Steyn, J. and Meyer, B. . (1973) ‘Production of ^{67}Ga by deuteron bombardment of natural zinc.’, *Int. J. Appl. Radiat. Isot.*, 24, pp. 369–372.

Stolarz, A. (2014) ‘Target preparation for research with charged projectiles’, *Journal of Radioanalytical and Nuclear Chemistry*, 299(2), pp. 913–931. doi: 10.1007/s10967-013-2652-2.

Szelecsényi, F. *et al.* (1998) ‘Evaluated cross section and thick target yield data bases of Zn + p processes for practical applications’, *Applied Radiation and Isotopes*. Elsevier Sci Ltd, 49(8), pp. 1005–1032. doi: 10.1016/S0969-8043(97)10103-8.

Szelecsényi, F. *et al.* (2012) ‘Investigation of direct production of ^{68}Ga with low energy multiparticle accelerator’, *Radiochimica Acta*, 100(1), pp. 5–11. doi: 10.1524/ract.2011.1896.

Takács, S. *et al.* (2007) ‘Evaluated activation cross sections of longer-lived radionuclides produced by deuteron induced reactions on natural titanium’, *Nuclear Instruments and Methods in Physics Research, Section B: Beam Interactions with Materials and Atoms*, 262(1), pp. 7–12. doi: 10.1016/j.nimb.2007.05.011.

Tárkányi, F. *et al.* (2004) ‘Excitation functions of deuteron induced nuclear reactions on natural zinc up to 50 MeV’, *Nuclear Instruments and Methods in Physics Research, Section B: Beam Interactions with Materials and Atoms*, 217(4), pp. 531–550. doi: 10.1016/j.nimb.2003.11.089.

The Editors of Encyclopedia Britannica (2018) ‘Nuclear medicine’, *Encyclopedia Britannica*. Available at: https://www.britannica.com/science/nuclear-medicine.

Vavere, A. L., Laforest, R. and Welch, M. J. (2005) ‘Production, processing and small animal PET imaging of titanium-45’, *Nuclear Medicine and Biology*, 32(2), pp. 117–122. doi: 10.1016/j.nucmedbio.2004.10.003.

Velikyan, I. (2018) ‘Prospective of 68 Ga Radionuclide Contribution to the Development of Imaging Agents for Infection and Inflammation’, *Contrast Media & Molecular Imaging*, 2018, pp. 1–24. doi: 10.1155/2018/9713691.

Vlasov, N. A. *et al.* (1957) ‘Excitation functions for the reactions Mg-24(d,a)Na-22, Fe-

54(d,a)Mn-52, Fe-54(d,n)Co-55, Zn-66(d,2n)Ga-66. At. Energ.2', *Journal of Soviet Atomic Energy*, 2, p. 189.

Watanabe, T. *et al.* (2014) 'Beam energy and longitudinal beam profile measurement system at the RIBF', in *Proceedings of the 5th International Particle Accelerator Conference (IPAC 2014)*, pp. 3566–3568.

Williams, D. C. and Irvine, J. W. J. (1963) 'Nuclear excitation functions and thick-target yields: Zn+d and Ar^{40}(d,a).', *Phys. Rev.*, 130, pp. 265–271.

Xiaowu, C. *et al.* (1966) 'Some measurements of deuteron induced excitation function at 13 MeV', *Acta Physica Sin.*, 22, pp. 250–252.

Yang, Q., O'Connor, D. J. and Wang, Z. (1991) 'Empirical formulae for energy loss straggling of ions in matter', *Nuclear Inst. and Methods in Physics Research, B*, 61(2), pp. 149–155. doi: 10.1016/0168-583X(91)95454-L.

Ziegler, J. F., Biersack, J. P. and Ziegler, M. D. (2008) 'SRIM: the Stopping and Range of Ions in Matter. [Online]. Available: http://www.srim.org'.

Ziegler, J. F., Ziegler, M. D. and Biersack, J. P. (2010) 'SRIM - The stopping and range of ions in matter (2010)', *Nuclear Instruments and Methods in Physics Research, Section B: Beam Interactions with Materials and Atoms*, 268(11–12), pp. 1818–1823. doi: 10.1016/j.nimb.2010.02.091.